Design, Integration, and Miniaturization of a Multichannel Ultra-Wideband Snow Radar Receiver and Passive Microwave Components

By

Jay William McDaniel

Submitted to the graduate degree program in Electrical Engineering & Computer Science and the Graduate Faculty of the University of Kansas School of Engineering in partial fulfillment of the requirements for the degree of Master of Science

_____

Chairperson: Dr. Carl Leuschen

_____

Co-Chair: Dr. Jie Bang (Stephen) Yan

_____

Dr. Sivaprasad Gogineni

Date Defended: April 28th, 2015

The Thesis Committee for Jay William McDaniel

certifies that this is the approved version of the following thesis:

Design, Integration, and Miniaturization of a Multichannel Ultra-Wideband Snow Radar Receiver and Passive Microwave Components

_____

Chairperson: Dr. Carl Leuschen

_____

Co-Chair: Dr. Jie Bang (Stephen) Yan

_____

Dr. Sivaprasad Gogineni

Date approved: May 1st, 2015

ABSTRACT

At the Center for Remote Sensing of Ice Sheets (CReSIS), two Ultra-Wideband (UWB) Frequency Modulated Continuous Wave (FMCW) radars are used for remote sensing of snow. The 12-18 GHz Ku-Band Radar altimeters provides high resolution surface elevation measurements, while the 2-8 GHz Snow Radar measures snow thickness over sea ice. In order for the Intergovernmental Panel on Climate Change (IPCC) to continuously develop more accurate models, additional snow characterization over sea ice is needed. Employing a constrained optimization approach, the snow water equivalent (SWE) can be estimated directly from the measured radar backscatter. Using the current Snow Radar depth measurement ability along with modified SWE approximation, remotely sensed snow density data can be gathered over large areas using airborne microwave sensors. These additional snow parameters will allow scientists to more accurately model a given area of snow and its effect on polar climate change. To meet this demand, a new "Airborne" Multi-Channel, Quad-Polarized 2-18GHz Snow Radar has been proposed. With tight size and weight constraints from the airborne platforms deploying with the Navy Research Laboratory (NRL), the need for integrated and miniaturized receivers for cost and size reduction is crucial for future deployments.

A set of heterodyne microwave receivers were developed as part of the new 2-18 GHz Snow radar to satisfy the March 2015 NRL deployment. The receivers were designed to enable snow thickness measurements from a survey altitude of 500 feet to 5000 feet while nadir looking, and estimation of SWE from polarimetric backscattered signals at low elevation 30 degree off nadir. The individual receiver has undergone a five times size reduction with respect to initial prototype design, while achieving a sensitivity of -125 dBm on average across the 2-18 GHz bandwidth, enabling measurements with a vertical range resolution of 1.64 cm in snow. The design

of a compact enclosure was defined to accommodate up to 18 individual receiver modules allowing for multi-channel quad-polarized measurements of snow backscatter over the entire 16 GHz bandwidth. With the new receiver and enclosure design, a one-fourth size reduction of the overall receiver chassis has been accomplished. The receiver bank was tested individually and with the entire system in a full multi-channel loop-back measurement, using a 2.95 μs optical delay line, resulting in a beat frequency of 200 MHz with 20dB range side lobes. Due to the multi-angle, multi-polarization, and multi-frequency content from the data, the number of free parameters in the SWE estimation can thus be significantly reduced resulting in more accurate estimation of SWE.

In addition to the receiver design, several UWB passive components were designed, fabricated, and tested for future implementation to reduce cost and allow for quick lead time due to in-house assembly. Design equations have been derived and a new method for modeling Suspended Substrate Stripline (SSS) filters in ADS for rapid-prototyping has been accomplished. Two SSS filters were designed which include an Optimized Chebyshev SSS Low Pass Filter (LPF) with an 18 GHz cutoff frequency and a Broadside Coupled SSS High Pass Filter (HPF) with a 2 GHz cutoff frequency. These filters were designed and modeled in house and sent out for professional fabrication. Mechanical design, fabrication, and assembly were all completed at CReSIS. Measurements were taken with a Vector Network Analyzer (VNA) and compared with HFSS simulations. Also, a 2-18 GHz three- port Transverse Electromagnetic (TEM) Mode Hybrid 8:1 power combiner was designed and modeled at CReSIS. This design will be integrated into the Vivaldi Dual Polarized antenna array with 8 active dual-polarized elements to implement a lightweight and compact array structure, eliminating cable and connector cost and losses.

ACKNOWLEDGEMENTS

The advice and support from my primary adviser Dr. Stephen Yan has been crucial to the success of my research. Dr. Yan's confidence in my capabilities throughout my research has pushed me far beyond what I thought I was capable of. The research opportunity through the Naval Research Laboratory (NRL) has not only enhanced my knowledge of theory but has also enriched my understanding of the process to take something from an idea to a final product.

I would also like to thank Dr. Sivaprasad Gogineni and the Center for Remote Sensing of Ice Sheets (CReSIS) for providing this incredible research opportunity. Dr. Gogineni offered superior insight and aid during specific research difficulties. He also provided the opportunity to attend events such as the National Science Foundation (NSF) D.C. site visit and Science and Technology Center (STC) directors meeting in Colorado.

There are several members of the CReSIS team which have been helpful during my research. Daniel Alvestegui has been a phenomenal source of information and help from day one at CReSIS. Dr. Carl Leuschen, Dr. John Paden, and Dr. Fernando Rodriguez were of impeccable aid in solving RF issues and providing assistance when needed. Aaron Paden solved several of my mechanical issues during integration and played a major role in the success of the receiver miniaturization. I would also like to thank Sean Holloway for helping with HFSS simulations and Justin Evers for assisting with antenna measurements, Visio rack layouts, and packing.

Finally, I would like to thank my fiancée Kathryn Zalenski for her never ending support and sacrifices made over the last couple of years. A special thank you goes to my father Gary McDaniel and grandmother Marjorie McDaniel, who have been there for me over the past six years of my collegiate career. Without them, none of this would have been possible.

TABLE OF CONTENTS

LIST OF FIGURES

1. INTRODUCTION

1.1 SCIENTIFIC BACKGROUND

In order to understand the global climate, determination of sea ice thickness is crucial. The heat exchange between the atmosphere and ocean is altered by the sea ice, specifically sea ice thickness, which separates them [12]. Under global warming conditions, the net energy absorbed by the ocean will increase, directly resulting in a reduction of the sea ice. The opposite is also true. Therefore, determination of the sea ice thickness can directly indicate global climate change. However, to accurately measure sea ice thickness, the overlaying snow must be fully characterized to compensate for the hydrostatic snow loading during the winter months [27]. If the snow density and thickness are known, sea ice thickness using freeboard ice measurements from airborne or satellite altimeters can be more accurately estimated [50].

At the Center for Remote Sensing of Ice Sheets (CReSIS), two Ultra Wideband (UWB) microwave radars have been developed and deployed to aid in the measurement of surface elevation and snow thickness over sea ice [2]. The 2-8 GHz Snow Radar is used for measuring snow over sea ice while the 12-18 GHz Ku Band Altimeter is used for high-precision surface elevation measurements [3]. The systems have been deployed several times over the last decade on NSF and NASA platforms in conjunction with Operation Ice Bridge (OIB). In section 1.3, a more detailed description of the two systems mentioned above will be given along with measured results.

To further update and more accurately predict sea ice thickness, information regarding snow properties like SWE or density will be needed in addition to snow thickness. Snow Water Equivalent (SWE) is the amount of water that would result from a given amount of snow melt [11]. Mathematically, this is equal to multiplying the snow depth by its' corresponding bulk snow

density [13]. Currently, SWE data is gathered from land based observation centers, which limits the area available for data gathering, or satellite-based which is weather limited and offers very low resolution. Also, the direct SWE measurement techniques currently employed are very time consuming. The constrained optimization approach allows SWE to be estimated directly from the measured backscatter. However, this approach has several free parameters. Fortunately, several of these free parameters can be filled by the radar system with multi-polarization, multi-frequency, and multi-look- angle capabilities.

Using the current Snow Radar depth measurement ability along with modified SWE approximation, remotely sensed snow density data can be gathered over large areas using airborne microwave sensors. In order to meet this demand, a new Multi-Channel, Quad-Polarized 2-18 GHz Snow Radar was developed. In section 1.4, this new system will be described in more detail. Before any further discussion on the systems designs, a brief overview on FMCW RADAR will be given.

1.2 FMCW RADAR OVERVIEW

Frequency Modulated Continuous Wave (FMCW) Radar is a special form of Continuous Wave (CW) Radar where the primary difference is the modulated waveform. In most cases, the waveform is linearly frequency modulated and thus given the acronym (LFMCW). This is commonly known as a chirp. CW Radars can only detect radial velocity using the Doppler Effect, while a FMCW Radar can measure both radial velocity and range to the target [1].

Figure 1-1 shows the block diagram of a typical FMCW Radar system. A waveform generator creates the frequency modulated waveform which then divides into two paths. Part of the signal, known as the reference signal, is coupled off into the Local Oscillator (LO) input of the mixer in the receiver chain. The other part of the signal is sent to the amplifier section of the transmitter. After the signal is amplified and filtered, it is transmitted into free space through a

transmit antenna continuously through a round trip travel to the target and reflected back, and then received by the receive antenna. The signal is filtered, amplified, and then down-converted in the mixer to create the beat frequency. Down-conversion is done by utilizing the ideal behavior of the mixer as a signal multiplier. The reference signal is multiplied by the received signal and then filtered to produce the Intermediate Frequency (IF) or beat frequency. This process is also known as stretch processing. Once the beat frequency is determined, information regarding the targets range and radial speed can be determined.

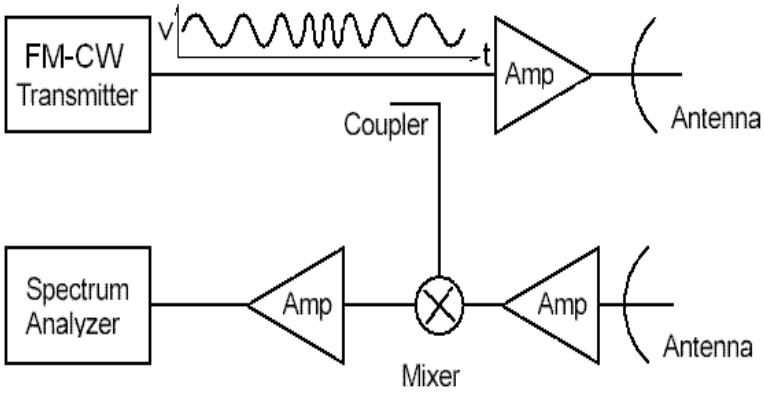

Figure 1-1: FMCW Block Diagram

As shown in figure 1-2 below, a frequency-time plot helps illustrate visually the beat frequency (f_b) which is shown as Δf. The beat frequency is the difference between the transmitted signal and the received signal [1]. As mentioned above, this is done in hardware through mixer multiplication, which creates a new signal with a frequency that is the sum of the reference and received signal, and another signal which has a frequency that is the difference between the reference and received signal. After low-pass filtering, only the difference or beat frequency signal is left to be further processed in the IF chain. In practice, the data product is the beat frequency which can then be converted into range as shown in equation 1.1

$$\Delta f = \frac{2 \cdot R \cdot k}{c} \tag{1.1}$$

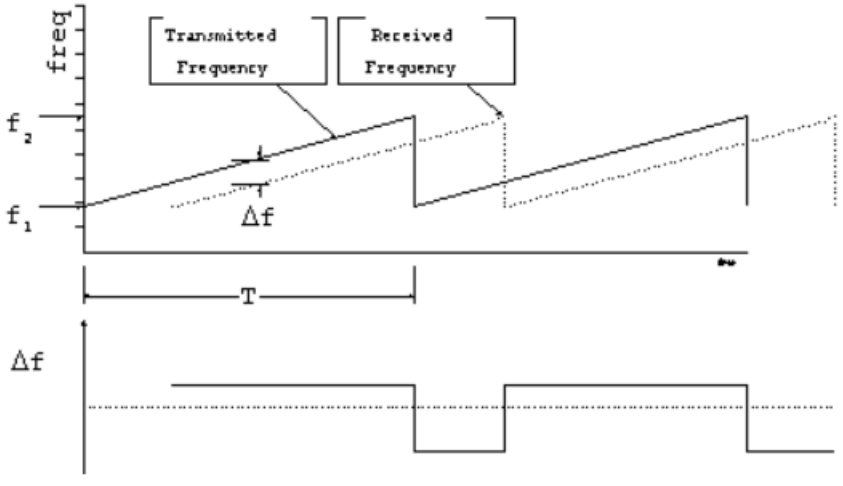

Figure 1-2: FMCW Radar Theory of Operation

In equation 1.1, range (R) is expressed in meters, chirp rate (k) is expressed in Hertz per second, and c is the velocity of propagation in free space. The chirp rate is the chirp bandwidth (B) divided by the pulse duration (Tpd) expressed in seconds. This is shown in equation 1.2.

$$k = \frac{B}{Tpd} = \frac{f_2 - f_1}{Tpd} \tag{1.2}$$

1.3 PREVIOUS SYSTEM DESIGN

Until March of 2015, the Snow Radar and Ku Band Altimeter were essentially two separate systems that shared a common chirp generator. This can be seen in figure 1-3. Inside the chirp generator, a 1.5-2.25 GHz baseband chirp was generated and then sent to a frequency multiplier unit with an effective frequency multiplication of eight. From there, the signal was split into two

separate chirps: a 12-18 GHz chirp and, after a -10 GHz frequency down conversion (FDC), a 2-8 GHz chirp. Following this step, the rest of the system was continuously broken up into two separate systems with each chirp having its own transmitter, receiver, and IF section. However, they did share an UWB horn transmit (Tx) and receiver (Rx) antenna for last season's NRL deployment. The rest of this section will contain brief explanations and block diagrams of the individual sections of the two systems.

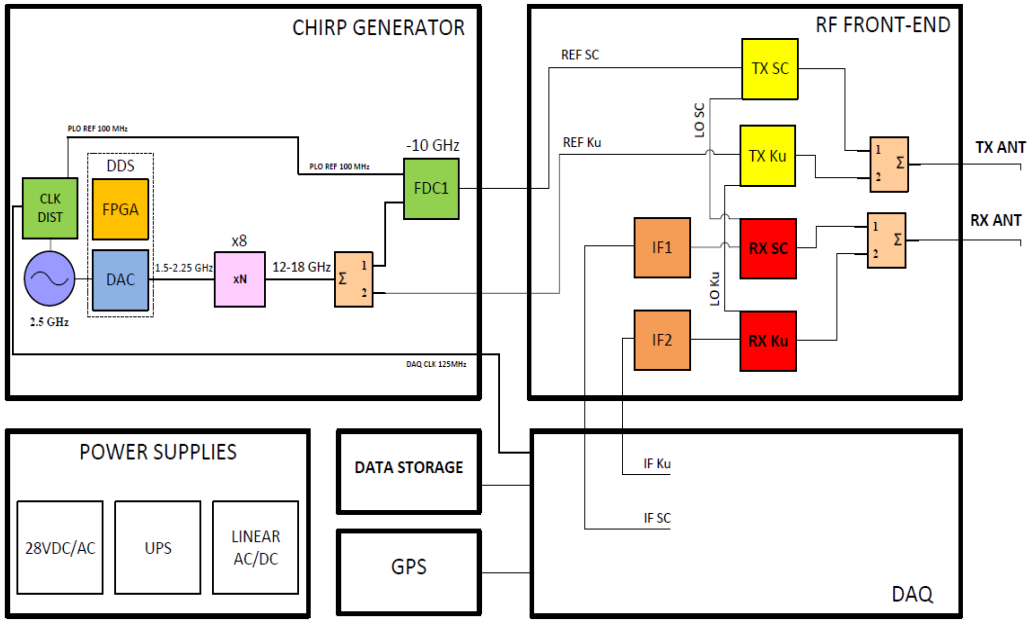

Figure 1-3: Snow Radar/Ku Band Altimeter System Block Diagram

The x8 frequency multiplier, located inside the chirp generator chassis, was designed to take the 1.5-2.25 GHz baseband chirp and up-convert it to a 12-18 GHz chirp. The process can be seen in figure 1-4. After the multiplier, the signal was sent through a 1:2 power divider where one of the chirps was sent to a -10 GHz FDC which can be seen in figure 1-5. The outputs of the chirp generator were a 2-8 GHz chirp and a 12-18 GHz chirp. These two signals were then fed into the radio frequency (RF) Front-End chassis.

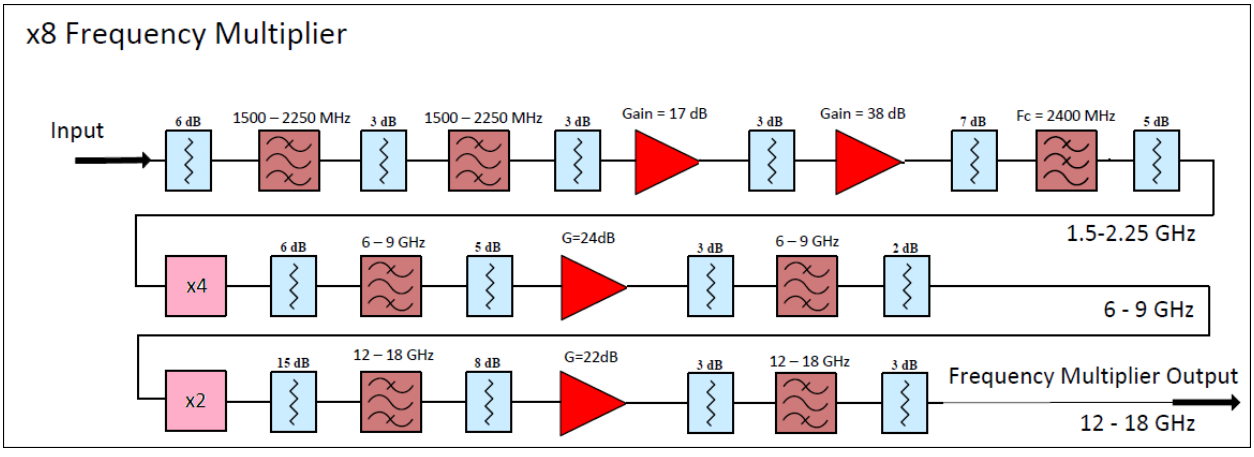

Figure 1-4: x8 Frequency Multiplier Block Diagram

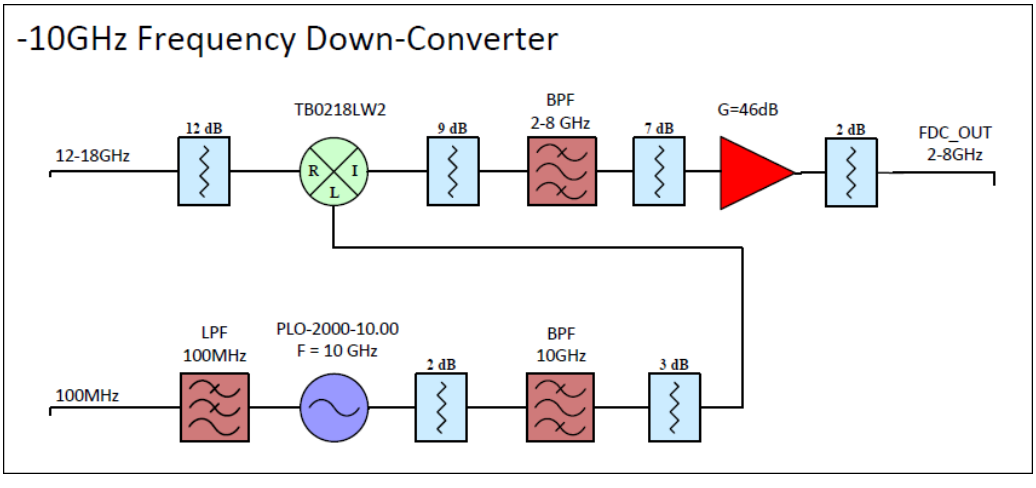

Figure 1-5: -10 GHz Frequency Down Conversion

After entering the RF Front-End chassis, the two chirps were amplified and filtered in their respective transmit chains, shown in figure 1-6. An isolator was used at the input and the output of the transmit chain in order to provide high isolation between the two chains. A 10 dB coupler was used to couple a portion of the transmit signal, which will act as the local oscillator (LO) signal for down-conversion in the receiver.

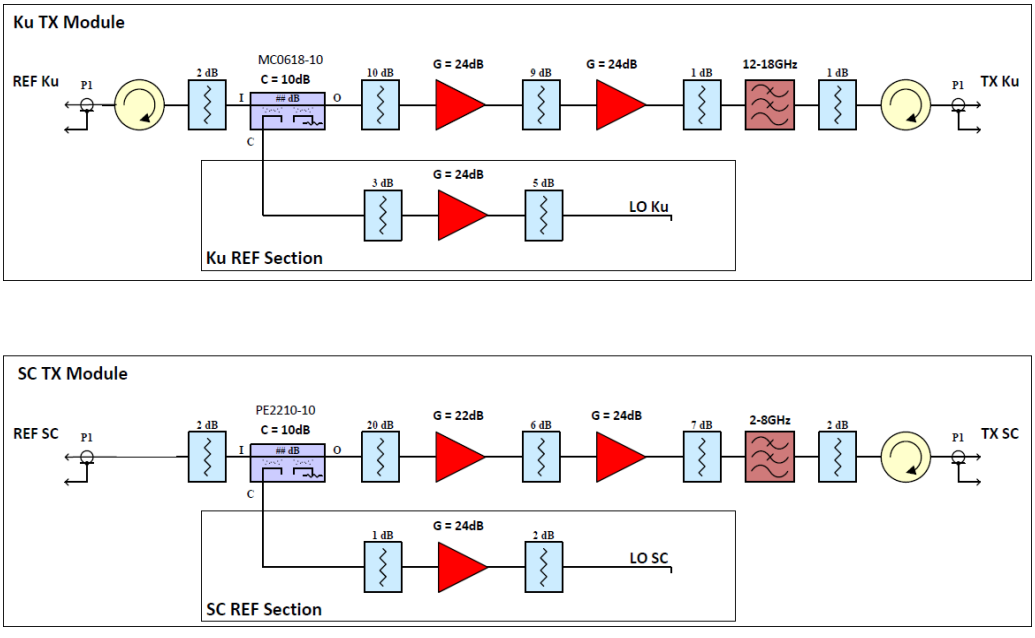

Figure 1-6: Snow Radar/Ku Band Altimeter Transmitter Block Diagram

Following the transmit chain, the signals were combined using a 2:1 power combiner and fed into a UWB Tx horn antenna. The Tx antenna chosen was an UWB 0.9-18 GHz Dual Polar Q-Par Horn antenna with radome [47]. The Rx antenna was chosen to be an UWB 2-18 GHz Dual Polar A-Info Horn antenna [48] inside a custom enclosure, which was designed and fabricated at CReSIS. The purpose of the custom enclosure is to minimize the mutual coupling between the Tx and Rx antennas, and this will be discussed in 2.2.3.

At the output of the receive antenna, the signal was split into two using a 1:2 power divider and sent to two different receivers, shown in figure 1-7. One receiver was designed for the 2-8 GHz received signal, while the other was designed for the 12-18 GHz signal. Each signal was filtered, amplified, and down-converted to the beat frequency before being sent to the IF module. An isolator was used at the input of each receiver to provide ample isolation between the two separate systems.

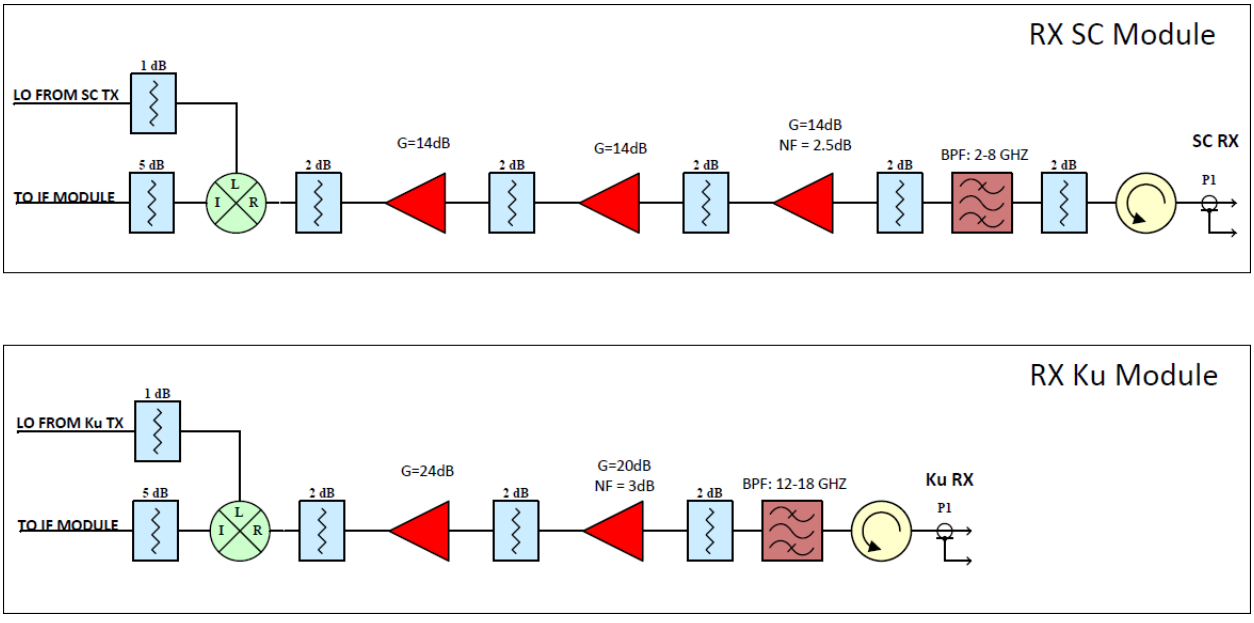

Figure 1-7: Snow Radar/Ku Band Altimeter Receiver Block Diagram

The purpose of the IF module is to further amplify the signal to make sure it fits within the dynamic range of the analog to digital converter (ADC) so it can be digitized for processing. The IF module is also designed to filter out any low frequency signals created due to directly coupled signals between the antennas and filter the beat frequency based on which Nyquist Zone we are operating in. The IF module block diagram is shown below in figure 1-8; the same IF module was used for both 2-8 GHz and 12-18 GHz signals. After the IF module, both signals are sent to the NI-DAQ digitizer.

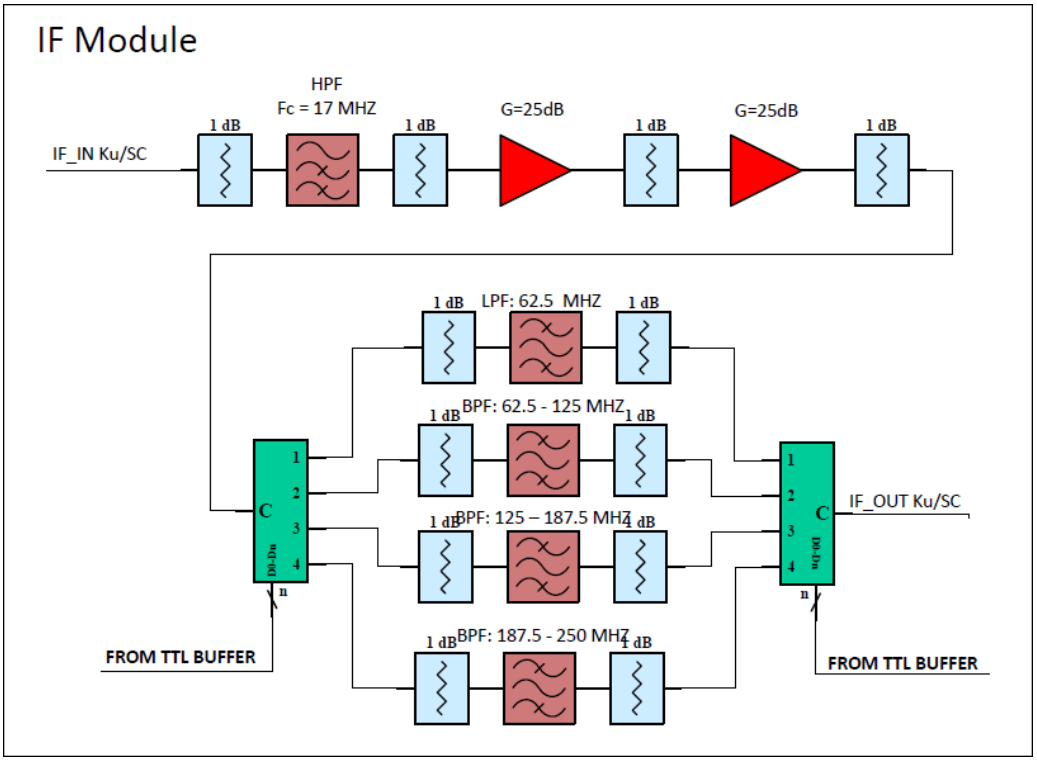

Figure 1-8: IF Module Block Diagram

Because of the need for new polarimetric and multi-angle measurements, a new multi-channel system would need to be designed. Using a similar design setup for the "new" snow radar by duplicating the receiver system over and over to meet the receiver number requirements, it was estimated 16U of rack space was needed for the Rx bank, LO distribution, and power supplies. The Twin Otter aircraft was not a feasible option because it only contained 20U of rack space for the entire system. Therefore, the design of miniaturized and integrated 2-18GHz radar receivers with a modular mechanical integration to reduce size and weight was a necessity for continued radar complexity to satisfy research demands.

1.4 CURRENT SYSTEM DESIGN

As mentioned above in section 1.1, the constrained optimization approach for determining SWE has three free parameters, corresponding to the radar system design: polarization, frequency,

and look-angle. The SWE can be most accurately predicted from the backscatter with more information about how each of these variables affects the SWE.A large bandwidth is important because the backscatter is a function of frequency. Therefore, the integration of the 2-8 and 12-18 GHz, with addition of the 8-12 GHz bandwidth, was chosen for a full 16 GHz. This also allows for a theoretical range resolution of 1 cm, with approximately 1.5 cm vertical range resolution after applying the Hanning window. The previous system has a 3.75 cm theoretical resolution after Hanning window degradation; thus, the new system has 75% better resolution. With the need for both vertical (V) and horizontal (H) polarizations, a minimum two-channel receiver chassis is needed. This will allow for quad-polarized measurements which are VV, HH, VH, and HV.

However, because SWE is also a function of angle, flexibility in changing the look-angle is needed. This can be done by physically moving the antenna to a different look-angle or designing a mounting structure that can adjust to different look angles. The drawback is that both of these approaches are mechanically limited, bulky, and time consuming. A third approach called electronic beam-steering can satisfy changing the look-angle without physically or mechanically moving the antenna structure. This is done on receive only and requires every antenna element to have a designated receiver in order to independently control the phase center of that element. Therefore, multiple receiver channels will need to be built to allow for electronic beam-steering. In figure 1-9, the system block diagram for the new Snow Radar is shown.

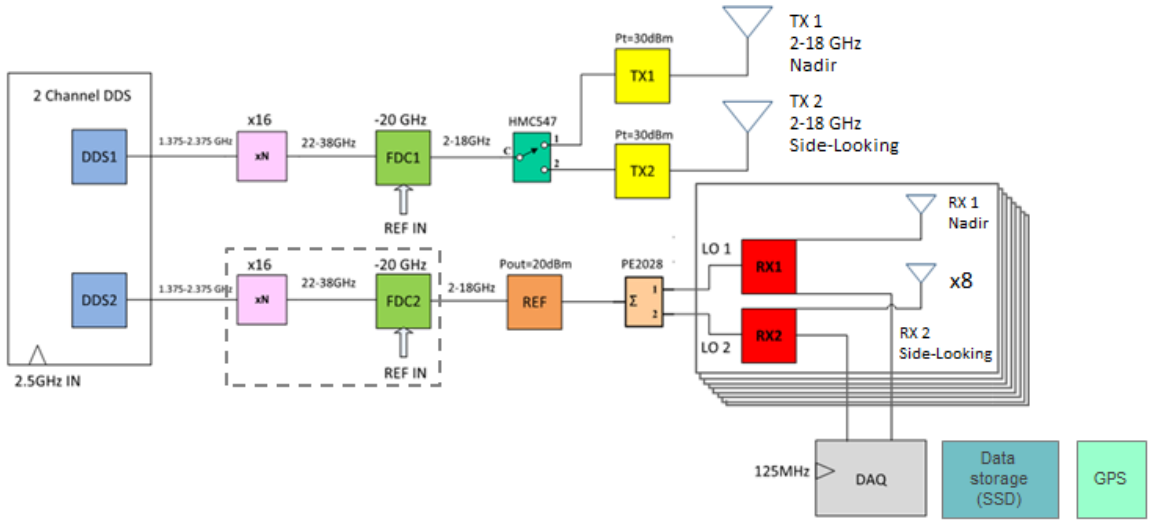

Figure 1-9: Snow Radar System Block Diagram

For the new Snow Radar system, the chirp generator chassis contains the hardware to generate two independent baseband chirps. The first chirp will be the signal chirp and the second chirp will be the reference chirp. This reference chirp can be generated independently and will be used as the LO signal for down-conversion in the receiver. Because the section of the signal chirp is no longer coupled to create the reference signal, the beat frequency is no longer range dependent, so high LO isolation can also be achieved. In equation 1.1, range can be replaced by $c \times \tau$ where c is the speed of light and tau is the time delay associated with the wave propagation. Therefore, as range increases, time of propagation and beat frequency increases. However, the reference chirp can be time delayed from the signal chirp to give any desired beat frequency. During flight, a tracker can be implemented to continuously update the time delay based on the flight altitude to produce a fixed frequency. The two main benefits to this design are; the signal can be time delayed appropriately to produce a low beat frequency to eliminate the need for high sampling rate digitizers; and there is no need for multiple Nyquist zones because the beat frequency is range independent. This greatly reduces the cost of the digital system and hardware complexity in receiver and data processing.

After the two chirps are generated, they are both fed into their own ×16 frequency multiplier. The ×16 frequency multiplier block diagram I shown in figure 1-10. The 1.375-2.375 GHz baseband chip is multiplied by 16 to obtain a 22-28 GHz chirp, which is frequency down converted in the frequency multiplier chassis. See figure 1-11.

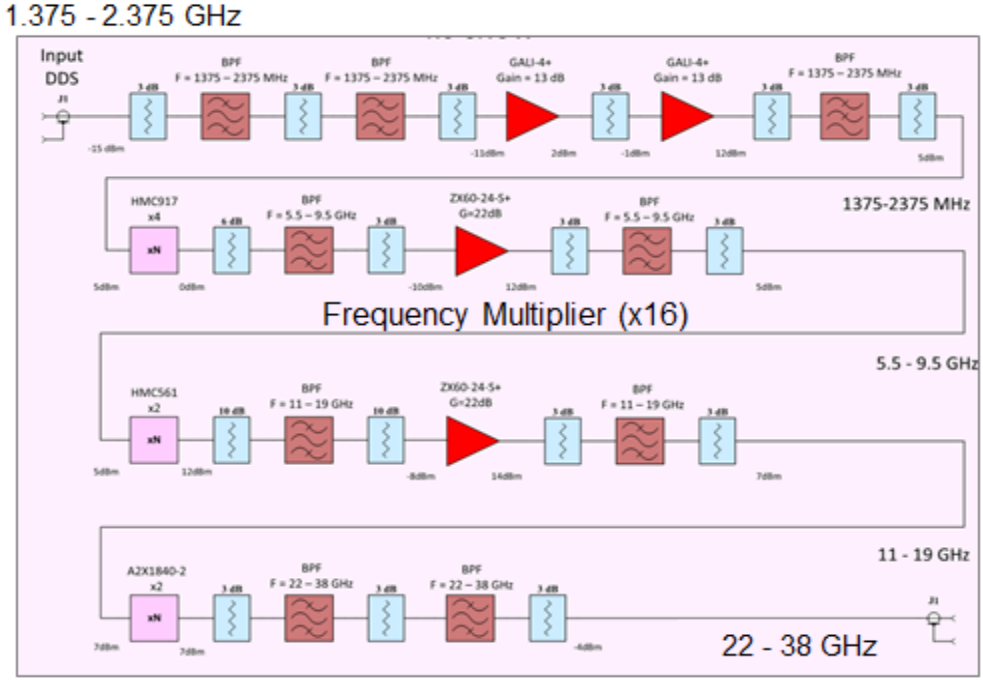

Figure 1-10: x16 Frequency Multiplier Block Diagram

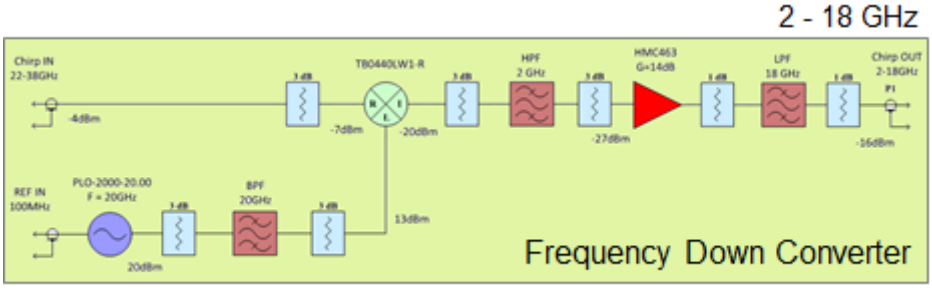

Figure 1-11: -20 GHz Frequency Down Conversion

The output of frequency multiplier 1 is fed into the transmitter chassis where it is gain compensated, filtered, amplified, and split into two signals. The signal is time multiplexed with a

switch between Nadir and side-looking antennas. This was done because of the need to designate one antenna to Nadir and one to side-looking. The transmitter block diagram is shown in figure 1-12.

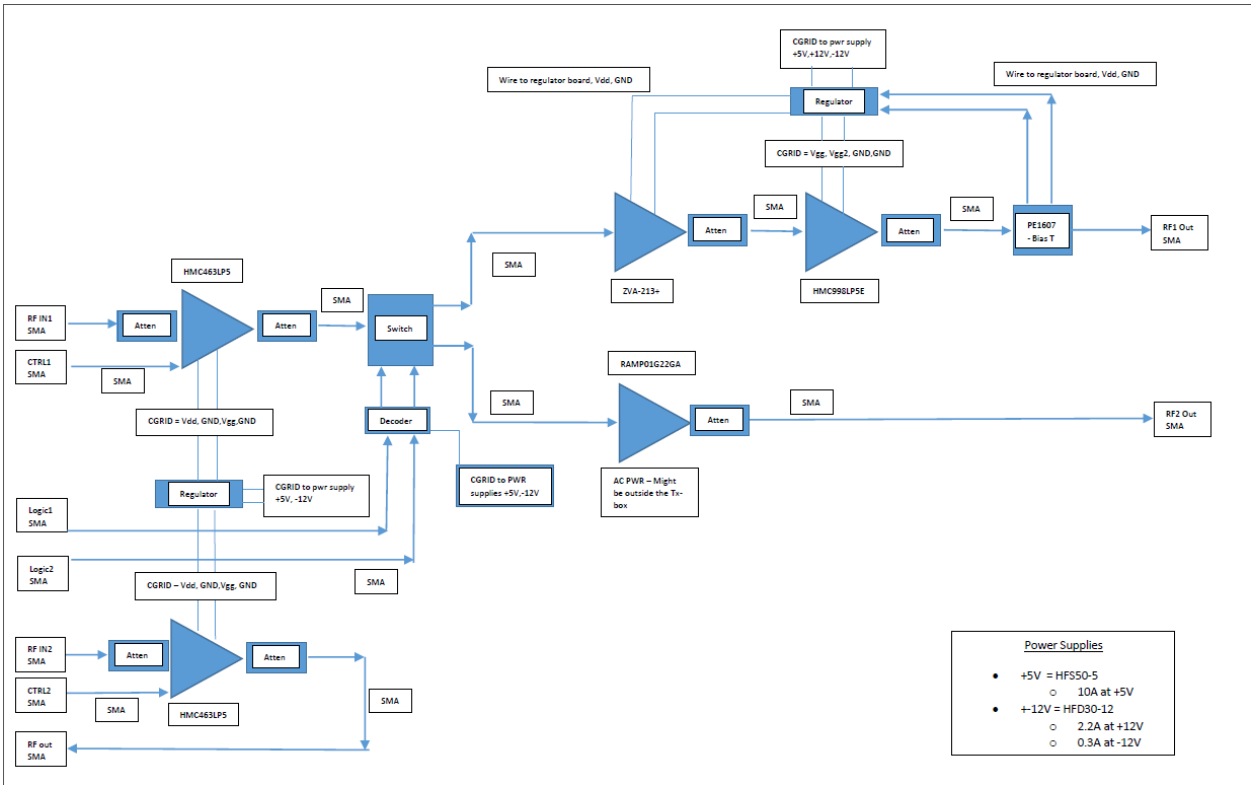

Figure 1-12: Transmitter Block Diagram

Due to the power level difference between the coherent specular Nadir returns and the non-coherent backscatter side-looking returns, the side-looking antennas required significantly higher gain than the Nadir antennas. The Nadir antennas used for the NRL mission were the same antennas used for the previous system. The additional side-looking Tx antenna used for the NRL mission was an UWB 2-18 GHz Satimo QR2000 Quad Ridge Horn antenna [49] and the Rx antenna was an UWB 2-18 GHz custom in-house designed Vivaldi Dual Polarized antenna array with 8 active dual-polarized elements.

The output of frequency multiplier 2 is fed into the LO distribution located in the receiver chassis where the signal is split using power dividers and amplified to the appropriate LO drive power into the mixer. The receiver chassis contains the individual receiver modules. There a receiver Nadir and 9 receiver for side-looking. The Nadir and side-looking differ slightly in attenuation values because of the expected return signal strengths. More attenuation was added in the Nadir channel to keep it from saturating when flying at low altitudes. A block diagram of an individual Nadir receiver is shown in figure 1-13; diagram of the side-looking channel is 1-14.

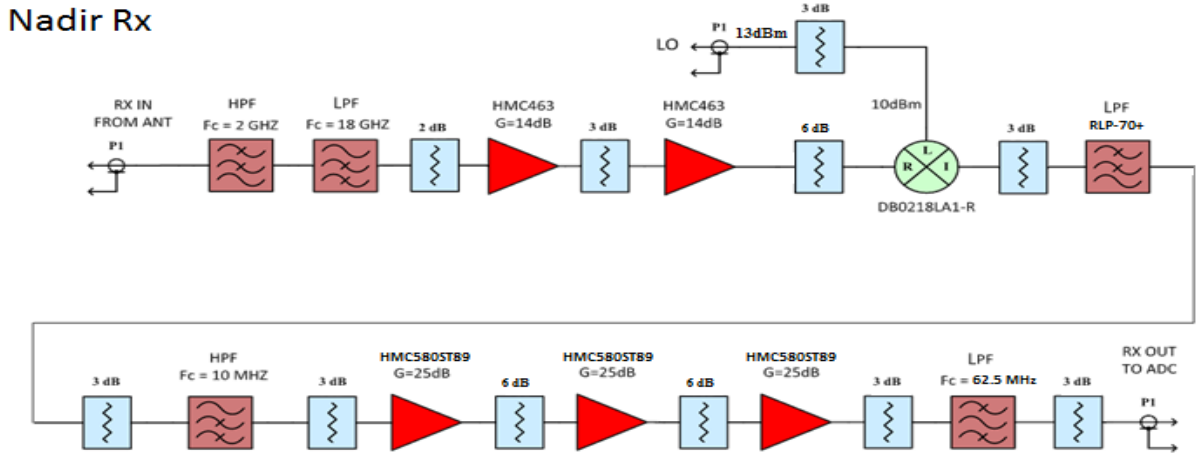

Figure 1-13: Nadir Receiver Block Diagram

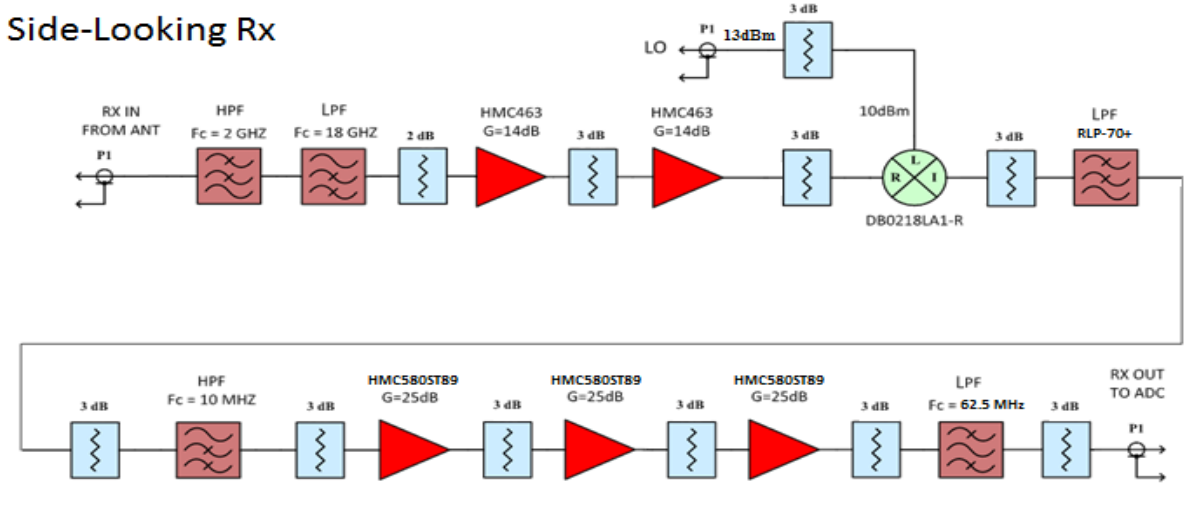

Figure 1-14: Side-Looking Receiver Block Diagram

As seen in the two figures above, there is no need for an anti-aliasing filter bank (Nyquist Zone filters) as before because a constant beat frequency can be achieved. It should be noted that the time delay of the second chirp should continuously be stored and saved that away it can be added during post-processing to extract the correct range to target.

A total system re-design was crucial to meet the scientific and engineering demands for the March 2015 NRL mission. The design of the direct digital synthesis (DDS) and FM were designed by Daniel Gomez-Alvestigui; CReSIS doctorate student on the NRL project. The main contributions of this these are as follows:

1. Design, integration, and miniaturization of a multichannel 2-18 GHz receiver using super-heterodyne receiver theory
2. Design and integration of a 2-18 GHz transmitter
3. Theory to measurement process of UWB SSS filters and theory to simulation process TEM-Mode Hybrid power divider

1.5 THESIS OUTLINE

Chapter 2: Receiver Design

This chapter discusses the system requirements and design of the 2-18 GHz integrated Snow Radar Receiver. A detailed link budget, which was pertinent to the receiver design, is discussed along with assumptions made. The LO distribution block diagram and performance measurements of individual sections of the receiver chain are presented. Finally, mechanical integration of the individual receivers into a 4U case receiver bank is shown as a finalized integrated product.

Chapter 3: Transmitter Design

This chapter discusses the system requirements and design of the 2-18 GHz integrated Snow Radar Transmitter. Performance measurements for both Nadir and Side-Looking channels are presented. A quick discussion on the automatic gain compensation (AGC) section, designed by Calen Carabajal, CReSIS masters student, will also be discussed. Finally, mechanical integration of the transmitter into a 2U case is shown as a finalized integrated product.

Chapter 4: Passive Component Design

Chapter 4 discusses the design of a DC-18 GHz Chebyshev Suspended Substrate Stripline (SSS) Low Pass Filter (LPF) and a 2-18 GHz Broadside Coupled SSS High Pass Filter (HPF). Theory and design guidelines for distributed filter design will be presented along with SSS filter theory and design considerations. The three-port TEM-Mode Hybrid Power Divider will also be presented in this chapter.

Chapter 5: Measurements and Results

This chapter shows measured results for the 2-18 GHz receiver when measured with a VNA in mixer mode. Measured results from the NRL deployment in Barrow Alaska are also provided in this section. Finally, an echogram is discussed which shows final data product results of interest to the scientific community.

Chapter 6: Conclusions and Future Work

Chapter 6 summarizes the results achieved for both the receiver and passive components described above. Also, a summary of future work for the receiver modules, filters, and power divider to further miniaturize and increase performance will be discussed.

2 RECEIVER DESIGN

2.1 SYSTEM REQUIREMENTS

For the NRL mission in March 2015, there was a set of system requirements for the new integrated Snow Radar receiver. The new receiver needed to be functional over the entire 2-18 GHz bandwidth. It was also requested for the receiver to detect Nadir return signals from 500 ft. to 5000 ft., although nominal flight altitude will be 1500 ft. The receiver was also designed to detect off-nadir return signals at 30 degrees from volumetric backscattering to determine SWE. The primary drive for an integrated and miniaturized receiver design was that the overall radar design had to meet aircraft requirements, especially in size and weight. Twelve receivers were built for the March 2015 NRL mission for the purpose of first time demonstration of the new radar: one receiver for Nadir, one receiver for side looking horizontal (H) polarization, eight receivers for side looking vertical (V) polarization, and two backup receivers.

2.2 LINK BUDGET

A receiver is the section of the Radar system which detects weak reflected or back-scattered signals, filters, amplifies, and works as a matched filter in order to maximize the signal to noise ratio (SNR) and eliminate any unwanted or coupled signals [1]. Before the receiver can be designed, a detailed link budget must be properly analyzed to determine the strength of signals expected at the input of the receiver. Once these signal powers are determined, a receiver design can begin, followed by an optimization of the design to meet all link requirements. The radar link budget can be estimated using the radar range equation which accounts for the transmitted power, free space path loss, and antenna gains in order to determine the power of the received signal at the input to the receiver [4]. Since it was intended to measure two different backscatters with the nadir and side-looking channels, the link budget analysis for the two cases are performed

separately. Also, the Nadir case was broken into two sections as well to look at the two extreme cases which will be discussed.

2.2.1 Nadir Link Budget

When the Snow Radar is operating in Nadir mode, there are two extreme cases that should be considered. The first case to consider involves flying at low altitude and expecting a large specular reflection from a lead. Leads are formed when the sea ice separates and drifts apart [5]. If the water, which has a high dielectric constant compared to that of air, fills the crack and becomes completely still, the surface will appear electrically smooth and a large specular reflection will occur [6]. The receiver should be designed not to saturate if this situation occurs because a lead is an excellent target for radar system calibration; therefore, a link budget analysis should be done for this given situation.

The specular radar range equation shown in equation 2.1 was used to determine the received power strength at the input of the receiver.

$$P_{Rx} = \frac{P_{Tx} \cdot G_{Tx} \cdot G_{Rx} \cdot \lambda^2 \cdot \Gamma^{sp}}{(4\pi)^2 \cdot (2R)^2 \cdot L} \tag{2.1}$$

The received power (P_{Rx}) is dependent on the transmitted power (P_{Tx}), the transmitter and receiver antenna gain (G_{Tx}) and (G_{Tx}) respectively, specular reflection coefficient (Γ^{sp}), range to the target (R), and the inherent losses in the system (i.e. cable loss, connectors, power divider, etc…). The expected return powers have been plotted below in figure 2-1. Notice that the link budget must be done versus frequency for UWB systems to incorporate component gain and loss variations across the entire pass band.

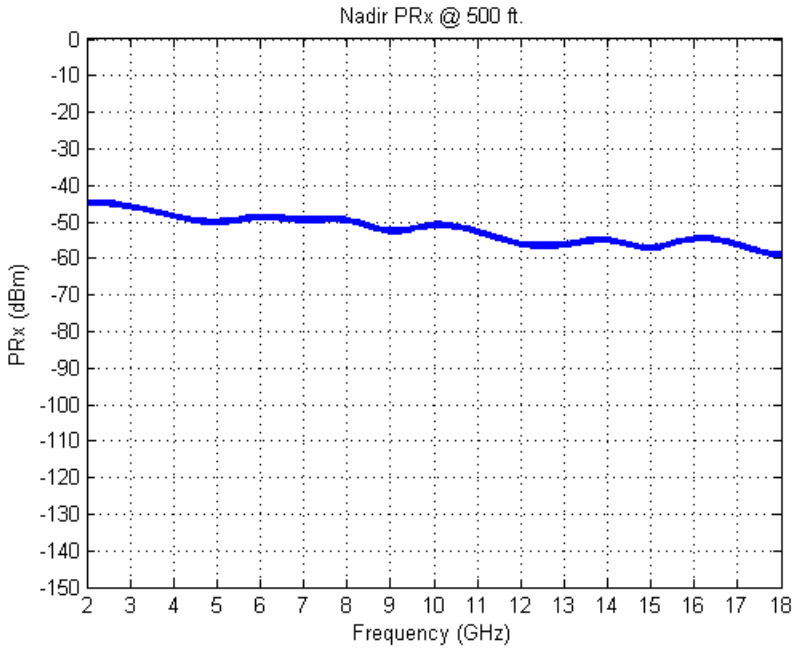

Figure 2-1: Nadir Return Power vs. Frequency at 500 ft. for NRL

The second extreme condition to be taken into consideration involves flying at high altitudes and expecting a small diffuse signal. Diffuse scattering occurs when the surface appears electrically rough and the incident signal is scattered in all directions [6]. Therefore, only a small amount of incident energy is directed back towards the receive antenna. The receiver should be designed to have a minimum detectable signal (MDS) capability low enough to detect the small diffuse return signals with ample SNR.

The radar range equation shown in equation 2.2 was used to determine the received power strength at the input of the receiver. This equation is slightly different from 2.1 because of the expected a scattered signal return rather than a specular reflection.

$$P_{Rx} = \frac{P_{Tx} \cdot G_{Tx} \cdot G_{Rx} \cdot \lambda^2 \cdot \sigma^o \cdot A}{(4\Pi)^3 \cdot (R)^4 \cdot L} \tag{2.2}$$

All the variables are the same as above except the backscattering coefficient (σ^o), and cross-sectional area (A). The nadir pulse limited area was calculated at 21.5 dB. The range was set to be 5000 ft. for the worst case scenario. Figure 2-2 shows the expected return signal power below.

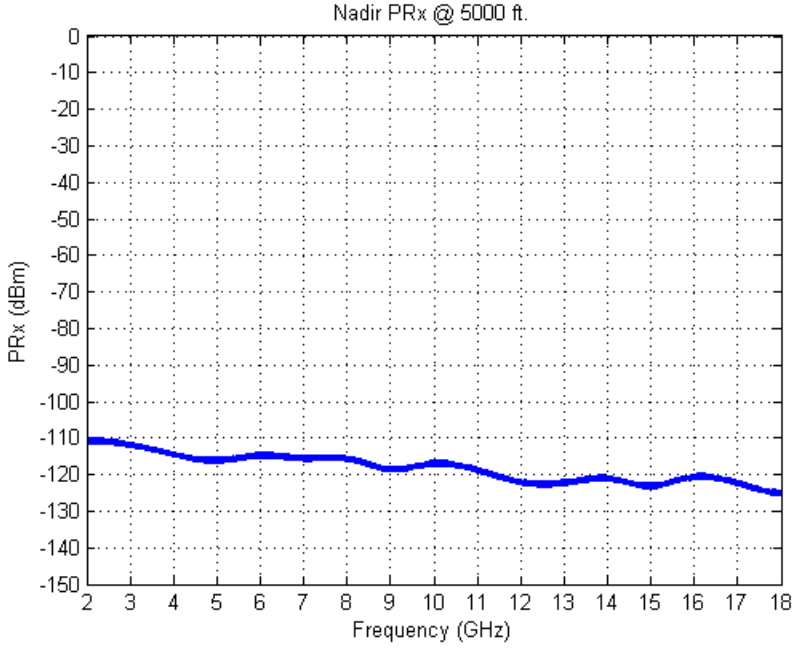

Figure 2-2: Nadir Return Power vs. Frequency at 5000 ft. for NRL

2.2.2 Side Looking Link Budget

When the Snow Radar is operating in the side looking mode, there are a few distinct differences between the system setup and calculations. First, due to the beamwidth limitations of the nadir Tx antenna and the incredibly small expected backscattered power, shown in figure 2-3, an additional transmit and receive antenna was designated to point at 30^o was decided. The variables used in the radar range equation are another major difference. Although it is the same as equation 2.2, the backscattering coefficient has been changed to the noise equivalent normalized backscatter which was set to -30 dBm [9] and [10]. Also, the area calculation is different because we are pulse limited in the cross-track and beam limited in the along-track while side-looking.

Taking these three major differences into consideration, figure 2-3 plots the expected return signals powers versus frequency.

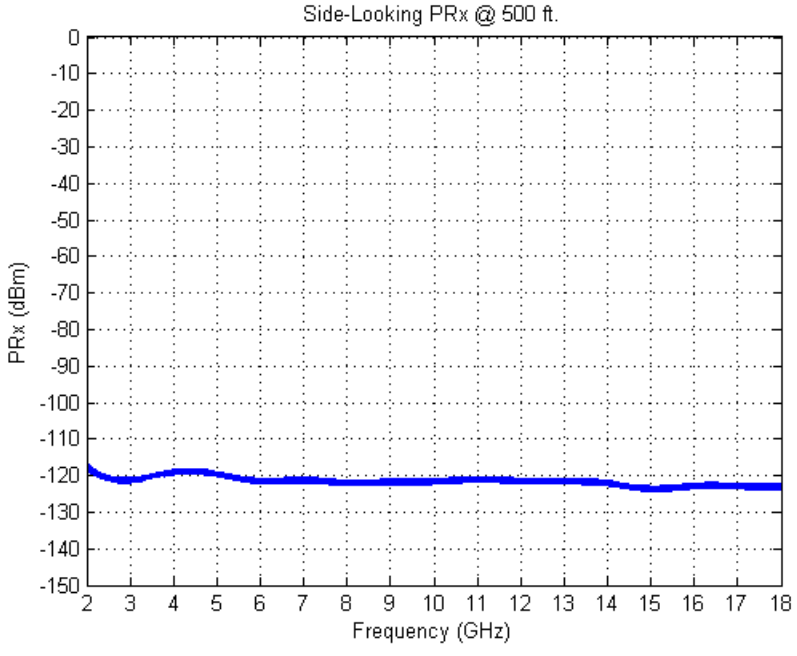

Figure 2-3: Side Looking Return Power vs. Frequency at 500 ft.

2.2.3 Coupled Signal Link Budget

Unlike pulsed radar, FMCW Radar simultaneously transmits and receives while the frequency varies as a function of time [1]. Because of this, a small portion of the transmitted signal will be directly coupled into the receive antenna. Due to little spreading loss over the short distance between the antennas, this coupled signal will appear large at the input of the receiver relative to the desired signal. From equation 1.1, this signal will typically be a very low beat frequency. In section 2.3 and 2.4, how this signal affects the RF section design and how it is filtered after down-conversion will be covered. For now, the highest priority is finding out how large this coupled signal will appear at the input to the receiver.

In order to determine the signal strength, the isolation was measured between the two Nadir looking antennas. For the NRL mission, the antennas will be mounted in antenna bays on the underbody of a DHC-6 Twin Otter aircraft. These bays are separated by approximately 20 feet; the isolation between antennas was measured in the anechoic chamber at the University of Kansas with 20 feet of separation. The antennas were pointed upwards because the distance between the antenna aperture and wall is greatest in this direction and reduces the effect of reflections from the wall. An HMC463LH250 Hittite low noise amplifier (LNA) was used to guarantee the received signal was above the noise floor and the data was averaged 150 times before being recorded. Reflections from the wall and walkway are typically very small, but the coupling measured is even smaller, which is why the signals were timed gated and recorded separately. Following the measurements, the amplifier gain was subtracted from the data to provide the actual isolation results. In figures 2-4 and 2-5, the isolation measurements setup and data results are provided.

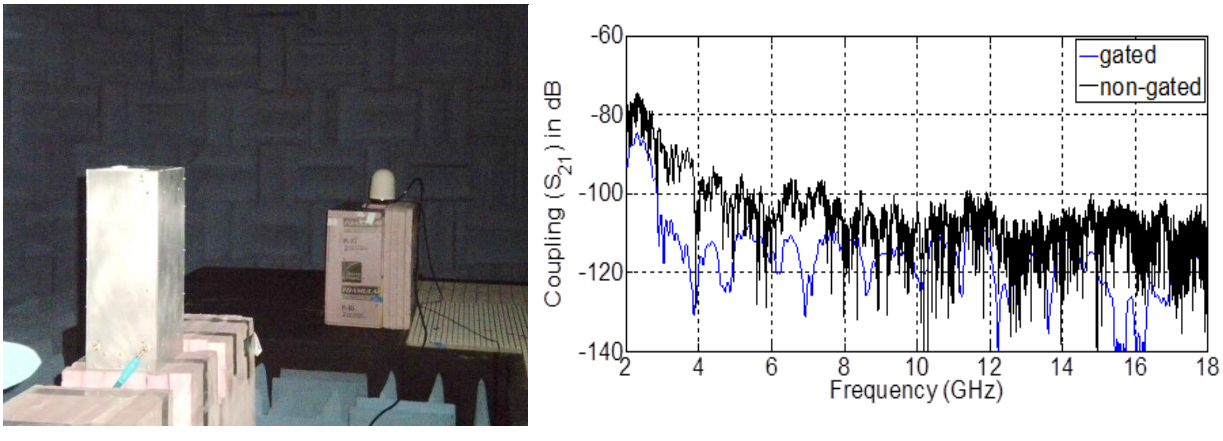

Figure 2-4: (Left)-Isolation Measurement Setup, (Right)-Isolation Data Results

From basic antenna theory, antenna gain and beam width are inversely proportional; the lower the gain, the wider the beam width [8]. Coupling is highest at 2 GHz because the electrical separation is shortest and the antenna beamwidth is widest at this frequency. Subtracting the worst

case scenario isolation of 80 dB from the 35 dBm transmit power, the worst case coupled signal will appear as a -45 dBm signal at the input of the receiver. This number will be important in section 2.3.4.

Because the side-looking antennas have higher gain than Nadir, the isolation will be greater than the Nadir scenario. Therefore, the worst case coupling is captured in the Nadir measurement above. If the Nadir receiver design (i.e. avoid saturation) can be satisfied with 80 dB isolation, then the required conditions for side-looking can be satisfied.

The rest of this chapter will be designated to the design of the receiver to detect the signals calculated and shown above. Section 2.3, 2.4, and 2.5 will be broken into a Nadir and side looking subset to differentiate the minor differences in the receiver design.

2.3 RF SECTION

The RF section of the FMCW receiver performs two very specific task: filtering unwanted signals and setting the sensitivity of the receiver [6]. A detailed description of the RF section will be described in 2.3.1 and 2.3.2 and the slight differences between them will be discussed. The upper chain in figure 1-13 and 1-14 should be used as reference for the following sections.

2.3.1 Nadir Receiver RF Design

The first components in the receiver chain is a high pass filter with a 2 GHz cutoff frequency followed by a lowpass filter with a cutoff frequency of 18 GHz. The filters were tested with a combination of pads between to try to improve matching. No benefit was achieved; therefore a pad was not used to reduce length and cost. However, a 2 dB was placed in between the filters and amplifier for matching. Following the filters are two low noise amplifiers (LNAs) which serve two important purposes. The amplifiers set the sensitivity of the receiver and provided high reverse isolation. Any reflected signals after the amplifiers are greatly attenuated before being re-

transmitted back out of the receive antenna. Finally a 3dB pad was inserted between the amplifiers for matching and a 6 dB pad was put between the second LNA and mixer. This was chosen because return signal powers for Nadir will be exceptionally larger than that expected for side-looking. A larger pad was inserted to keep the mixer from saturating because the RF input port of mixers are notoriously known for poor matching and the 6 dB pad greatly aids in the matching between the LNA output and mixer input. Finally, a 2-18 GHz mixer was used for down conversion to produce the beat frequency. The LO port of the mixer is fed from the LO distribution chain which will be discussed with further detail in section 2.6.

The noise figure of the receiver can be calculated using equation 2.3 [1]. Although the noise figure is determined by the entire receiver, the noise figure in the current design is set after the second LNA. Therefore, the noise figure and sensitivity can be calculated just from the RF section of the receiver, which will be analyzed in this section.

$$F_o = F_1 + \frac{F_2 - 1}{G_1} + \frac{F_3 - 1}{G_1 G_2} + \cdots + \frac{F_N - 1}{G_1 G_2 G_{N-1}} \tag{2.3}$$

Once the noise figure is known, the thermal noise sensitivity (MDS) of the receiver can be determined as:

$$MDS(dBm) = -174 + F_o + SNR + 10log_{10}(B_{IF}) \tag{2.4}$$

In the above equation, the desired SNR determined by the designer and B_{IF} is the IF noise bandwidth. The new Snow radar employs pulse compression by linearly chirping the transmitted signal. This allows for long chirp duration with a bandwidth corresponding to a short pulse [25]. Employing this technique the effective bandwidth becomes:

$$B_{IF} = \frac{1}{\tau} \tag{2.5}$$

Above, τ is the chirp duration. Incorporating equation 2.5 into 2.4, the pulse compression gain is added to the sensitivity calculation. As with the link budget in the plots above, the sensitivity must be calculated as a function of frequency due to gain and loss variations inherent in the components. Each component was characterized using a vector network analyzer (VNA) and the measured results were used to calculate the sensitivity. Calculated results are given in section 2.5.

Because the noise figure is set by the RF section alone, the correlation between receiver gain, system noise floor, and A/D noise level can be evaluated. Another way to achieve greater SNR is to do coherent averaging (coherent integration or pre-summing). From [25], coherent integration involves working with signals that have retained their magnitude and phase data and be combined from pulse to pulse to improve the overall SNR. However, two very important conditions must be met. The signals must remain coherent from pulse to pulse, and the noise must be uncorrelated from pulse to pulse. Thermal noise is constant on average across the frequency spectrum but will vary as a function of time [26]. This is also referred to as white noise. However, quantization noise, which is the noise floor set from the digitizer, is constant as a function of time. Therefore, if coherent integration is desired, the thermal noise floor needs to be greater than the quantization noise. This is done by increasing the receiver gain so that the thermal noise floor is above the quantization noise floor at the ADC.

The quantization SNR, given a 14 bit ADC with a max A/D level of 10 dBm ($2V_{pp}$ in a 50 Ω system), is calculated as follows [27]:

$$SNR = 1.76 + 20log_{10}(2^N) \tag{2.6}$$

N is the number of bits. For N=14, this is equal to 86.05 dB. Subtracting this from 10 dBm, the quantization noise floor is -76.05 dB. Next, the receiver noise floor can be solved for using

equation 2.4 by taking out the SNR variable. Given the A/D noise level and the receiver noise floor, receiver gain can be calculated as:

$$Required\ Rx\ Gain\ (dB) = -Rx\ Noise\ Floor(dBm) + AD\ Noise\ Level(dBm) \quad (2.7)$$

In figure 2-5, a plot showing the calculated values from 2.7 versus frequency is compared with the final measured receiver gain versus frequency. As seen from the plot, the actual measured gain is always 5 dB greater than the required receiver gain putting the thermal noise at a minimum of 5 dB above the quantization noise. Due to these results, the additional SNR can be achieved with coherent integration. By guaranteeing that the thermal noise floor is above the quantization noise floor, signal is guaranteed to be within the ADC's dynamic range as long as the measured signal sticks out of the thermal noise floor.

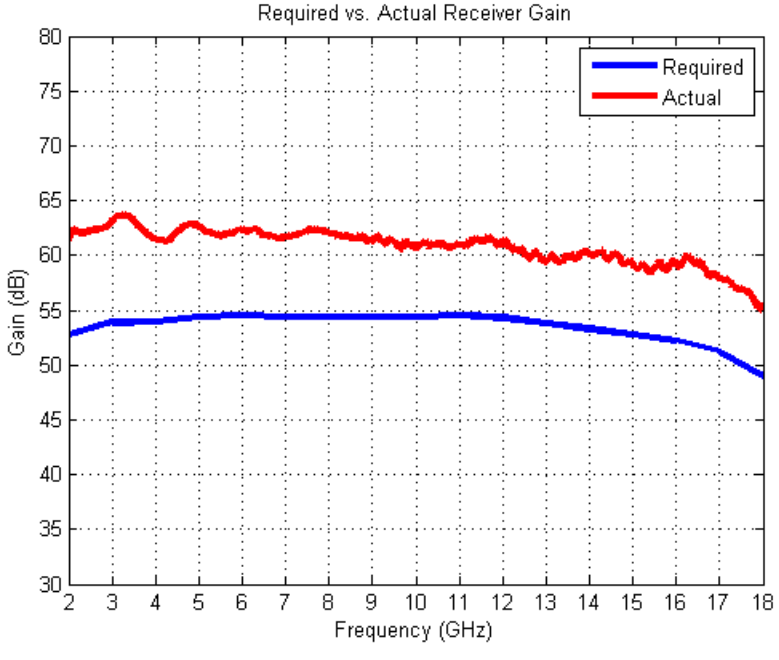

Figure 2-5: Receiver Gain Comparison for Coherent Integration

2.3.2 Side-Looking Receiver RF Design

The only major difference between the Nadir Rx RF section and the side-looking RF section is the pad between the second LNA and mixer. This pad has been reduced to a 3 dB pad. A smaller pad would have resulted in a slightly lower noise floor but the 3 dB pad was needed to minimize reflections due to the poor matching between the LNA output and mixer input. For side-looking, the input powers expected are lower than for Nadir and so saturation is not an issue with the reduced pad value.

Equation 2.3 and 2.4 are evaluated for the side-looking case, shown in section 2.5. It should also be apparent that since the noise figure for side-looking is equivalent to the Nadir noise figure and the gain of the RF section has increased by 3 dB, the actual gain of the receiver will be greater than the required receiver gain in 2.7. Thus, the side-looking receiver design will also allow for additional SNR from coherent integration.

2.3.3 RF Design Co-Simulation

To eliminate long lead times for amplifier evaluation boards, the amplifier chain used in the Rx RF front end was integrated, designed, fabricated, assembled, and tested in-house. All of the Rx components were provided with S2P files, run together in ADS to generate an ideal S_{21} plot. A full board design was done in HFSS and was used in conjunction with ADS and the characterized files to generate a Co-Simulated S_{21} plot. The Rx RF chain was built up using the connectorized eval boards and a S_{21} measurement was made in the lab. After fabrication and assembly of the in-house board, another Rx RF chain was built using this board and the S_{21} of the RF front end was measured in the lab. Figure 2-6 shows the HFSS board design to show the component integration.

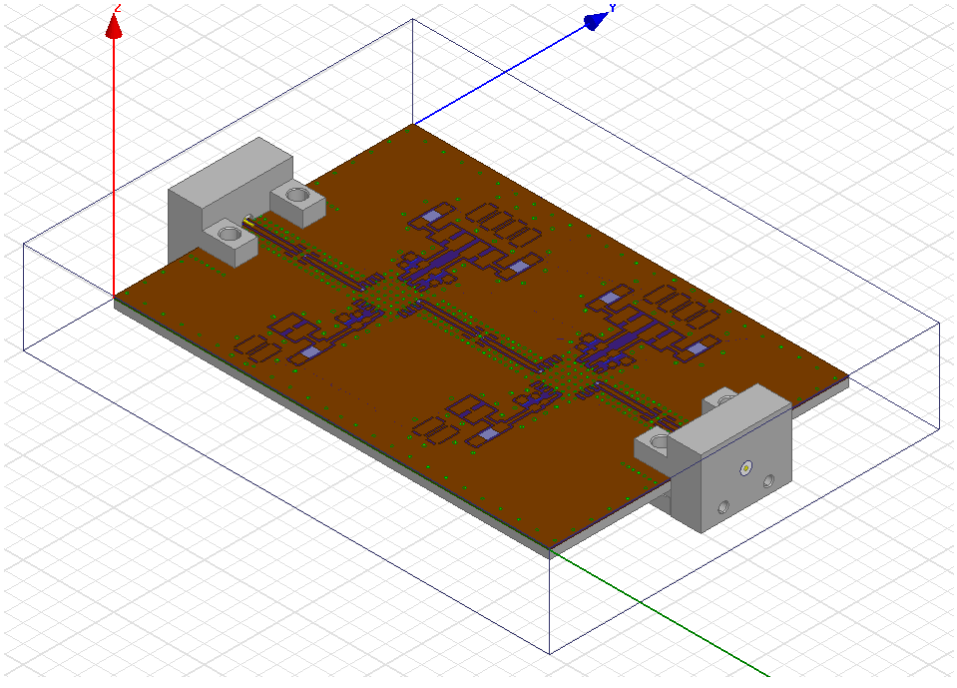

Figure 2-6: HFSS RF Board Design

Instead of designing the entire structure in HFSS, the copper layers and vias can be done in EAGLE and exported as Gerber files to ADS. Once board manipulations are done in ADS, files can be exported as a DXF/DWG design file and imported into HFSS. In HFSS, material characteristics and simulation ports can be added. After simulation is completed, the SXP file can be ported into ADS and all of the characterized component files can be used to implement a full Co-Simulation.

The board was designed on 10 mil thick Rogers 4350b material with 1oz. copper. The aluminum heatsink was designed and machined at CReSIS and serves two primary purposes. The heatsink provides mechanical support since the board material is so thin and it also allows for the board to be easily replaced inside the individual receiver cartridge. The Rogers material was attached to the heatsink using ECF 550 made by Henkel. This is an electrically conductive paste that is sold in sheets and can be custom fit. After the board is attached, the surface mount components can be put on using solder paste and put through a solder-reflow machine. Finally, the edge launch connectors can be attached and the board can be tested. Figure 2-7 is the final product

that was done in house. The LNAs are HMC464LH240 chips from Hittite and the bypass caps are UWB caps from Dielectric Labs. The connectors are Southwest Microwave Edge Launch connectors for coplanar waveguide (CPWG) layout and the DC power connectors are basic Molex connectors purchased from Digikey.

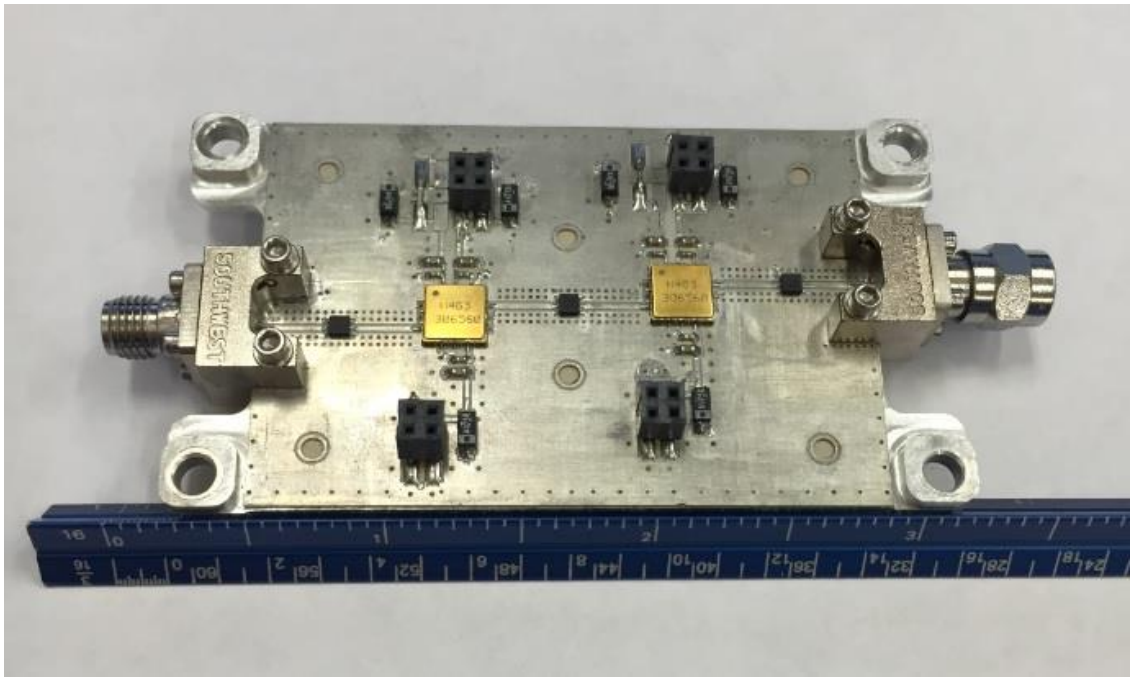

Figure 2-7: Integrated Receiver RF Amplifier Chain

Figure 2-8 is a plot comparing the RF chain response for all the different measurements and simulations mentioned above. In figure 2-8, the HFSS Co-simulation matches very closely to the ADS ideal simulation. Both of the lab measured boards also follow a general trend from 2-18 GHz. The difference between the two measured boards is due to the variation from chip to chip and can be seen from evaluation board to evaluation board. However, the RF amp chain board designed and developed at CReSIS gives very similar results to the purchased eval boards. For future expansion, this design can be used if eval boards are limited or unable to purchase.

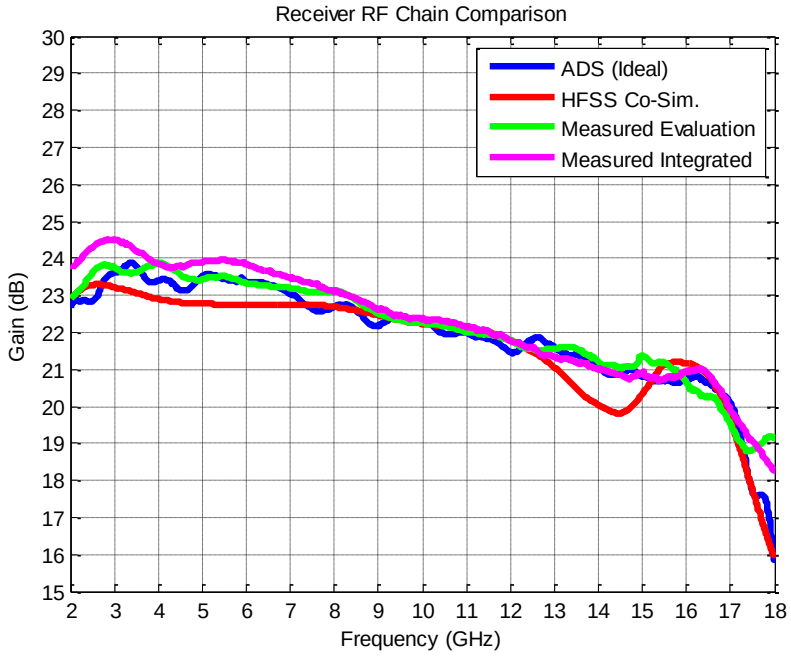

Figure 2-8: Receiver RF Chain Comparison

Figures 2-9 and 2-10 show the final measured results of the integrated RF chain as a function of frequency. The S_{11} is greater than 12.5 dB across the pass band, which is due to appropriately matching the system components and fine-tuning the integrated board layout. The S_{21} has a gain variation of 6 dB across the passband.

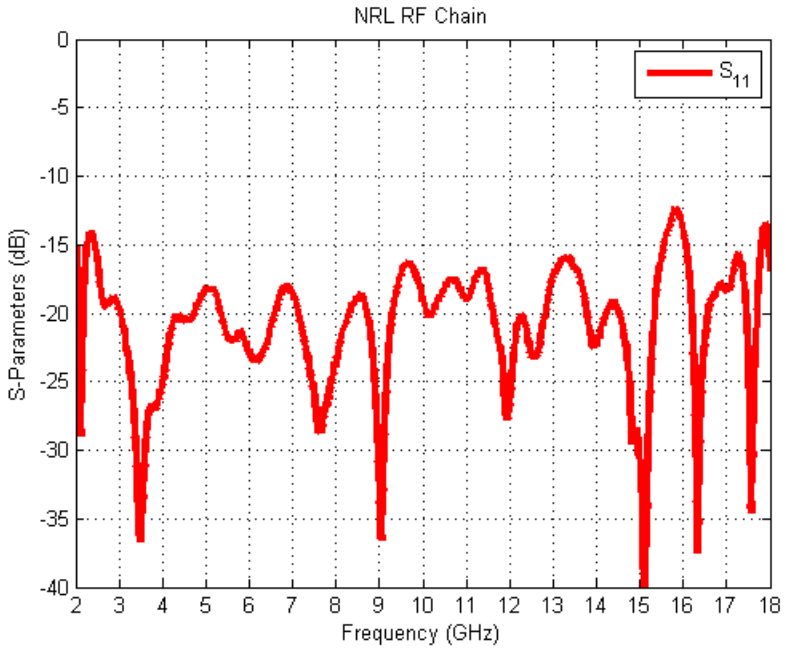

Figure 2-9: Integrated Rx RF Chain S_{11}

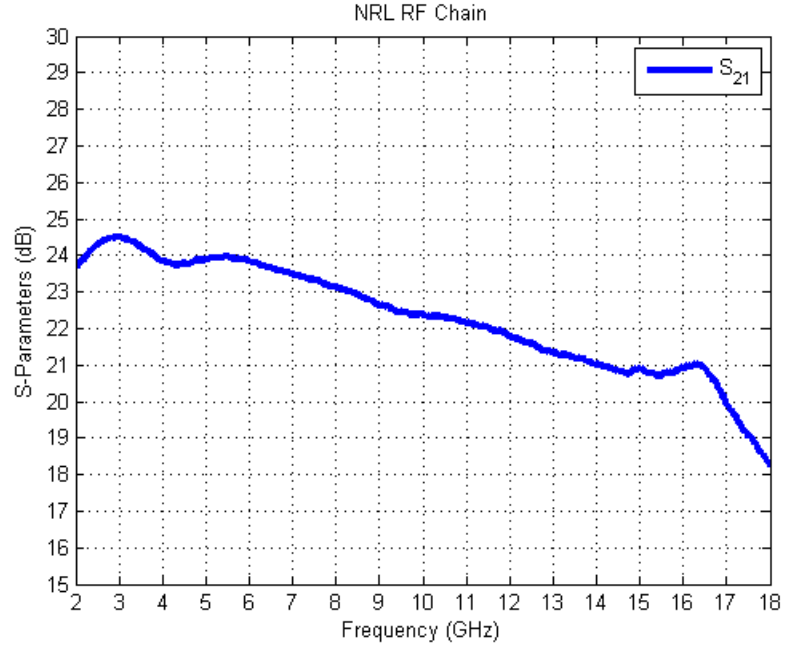

Figure 2-10: Integrated Rx RF Chain S_{21}

2.3.4 Mixer Saturation

The coupled signal discussed in 2.2.3 can be an issue in the RF section if it gets adequately amplified in the amplifier section causing the mixer to saturate. After the mixer, the signal will be down converted to either a low IF frequency (≈2.7 MHz) in single chirp mode or a high IF frequency (≈200 MHz) in dual chirp mode. Therefore, it is important for the coupled signal to make it to the IF section without saturating anything along the way. Techniques to get rid of this signal after the mixer will be discussed in 2.4.1.

As discussed above, a worst case coupling of 80 dB can be achieved at low frequency (≈ 2 GHz) with 20 feet of antenna isolation. This coupling was calculated given a 35 dBm transmit power that a -45 dBm signal will be present at the input of the receiver. Because the side-looking receiver has the highest gain, verification that the coupled signal is not saturating anything in the RF chain is required. If this is satisfied, than the nadir receiver design is satisfied as well. The P_{in}^{sat} was solved for the mixer and was found to be -15 dBm where the worst case coupled signal appears. This means that a signal would need to be -15 dBm or larger in order to saturate the mixer. Given a coupled signal of -45 dBm, 30 dB of head room from saturating the mixer is achieved. It should also be mentioned that the mixer is the first component in the RF section that will saturate given a large input signal. Therefore, since the mixer will not saturate due to the coupled signal, no other component in the RF chain will saturate either.

2.4 IF SECTION

The general purpose of the IF section is to filter out any unwanted signals other than the desired beat frequency and amplify it to fit within the ADC's dynamic range. In this section, the design of the IF section of the receiver is thoroughly discussed, and issues brought up in section

2.2.3 regarding coupled signals are addressed. The bottom chain in figure 1-13 and 1-14 should be used as reference in the following sections.

2.4.1 Receiver IF Design

Following down conversion in the mixer, the signal is sent through a Mini-Circuits RLP-70+ LPF which is used to filter out any high frequency leakage through the mixer. This particular LPF has a very slow roll-off but maintains at least 40 dB of attenuation all the way out to 4 GHz. This is important because the mixers are not perfect and have a finite isolation from LO to IF. The LO drive power for the Miteq DBO281LA1-R mixers is 10 dBm and only provides 20 dB of isolation from LO to IF. Therefore, it is crucial that these signals be filtered before entering the IF amplifier chain. The Hittite HMC580ST89 amplifiers still have some gain out to 4 GHz and if not properly attenuated could cause the IF section to saturate. Due to the isolation and attenuation through the LPF, the worst case leaked signals are approximately 40 dB from saturating the final IF amplifier. This filter serves another purpose when the Snow radar is operated in dual chirp mode. It can be proven that the coupled signal, after down-conversion, will appear around 200 MHz after down conversion. The RLP-70+ has an insertion loss of approx. 80 dB at 200 MHz and attenuates the coupled signal significantly.

The second filter in the IF chain is a custom designed HPF with a 10 MHz cutoff frequency. This filter serves two primary purposes. If the radar is operated in a single chirp mode, using equation 1.1 and setting R to be 6.096 m (20 feet antenna separation), the direct coupled signal between the antennas will show up as a beat frequency of approximately 2.7 MHz after down conversion. The IF HPF has approximately 80 dB of insertion loss (IL) at 2.7 MHz, which greatly attenuates the signal after down-conversion. A HPF with large attenuation at low frequencies also filters out high powered DC components which have leaked through the system.

After all unwanted signals have been filtered out, the desired beat frequency goes through an IF amplifier chain, which amplifies the signal into the dynamic range of the ADC. Some minor tuning to the IF amplifier bias line needed to be done in order to use Nyquist Zone 1 (10 MHz – 62.5 MHz) as the desired zone of operation. Using the radar in dual chirp operation, the reference chirp was time delayed to produce a beat frequency of 40 MHz, located in Nyquist Zone 1. Measurement of the populated eval board revealed that the bias line acted like a high pass filter with a cutoff frequency of 100 MHz. After three sections of filtering, the 40 MHz signal was only amplified by half of what it should have been. This design was built up in ADS and the RF choke inductor was tuned until it had a cutoff frequency of 10 MHz (821 nH). Although this reduced the attenuation at low frequencies, especially DC, this was not an issue due to the custom IF HPF used prior to the amplifier section.

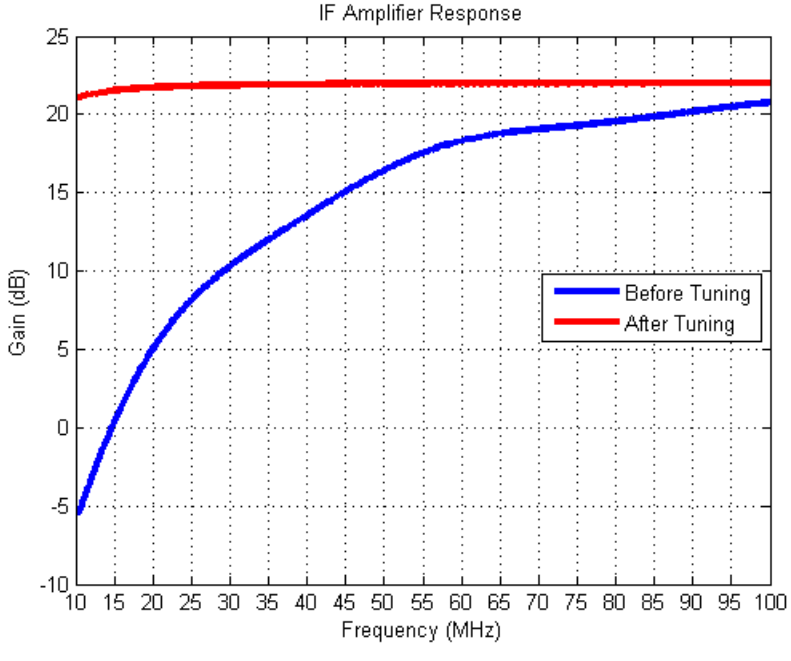

Figure 2-11: IF Tuning Comparison

The final stage of the IF board is a custom designed LPF with a cutoff frequency of 62.5 MHz. This filter is a seventh order elliptic filter designed to have a very sharp roll-off. The sole

purpose of this filter was to set the upper band of the first Nyquist zone. The digitizers used have a sampling frequency of 125 MHz. From the Shannon Nyquist theorem, this states that the first Nyquist zone will be DC-62.5 MHz which is what the filter was designed for.

After all the individual components were either designed or modified, a similar co-simulation was run for the IF section just as was done for the RF section. Figure 2-12 shows the HFSS board design to show the component integration. The board was designed on 62 mil thick Rogers 4350b material with 1oz. copper. Figure 2-13 is a plot comparing the simulated and measured IF chain. The simulated results vary slightly from the measured results due to non-ideal filter performance. The HFSS model used ideal lumped element components to implement the filter performance; whereas, the measured results take into consideration actual filter performance due to non-ideal component behavior.

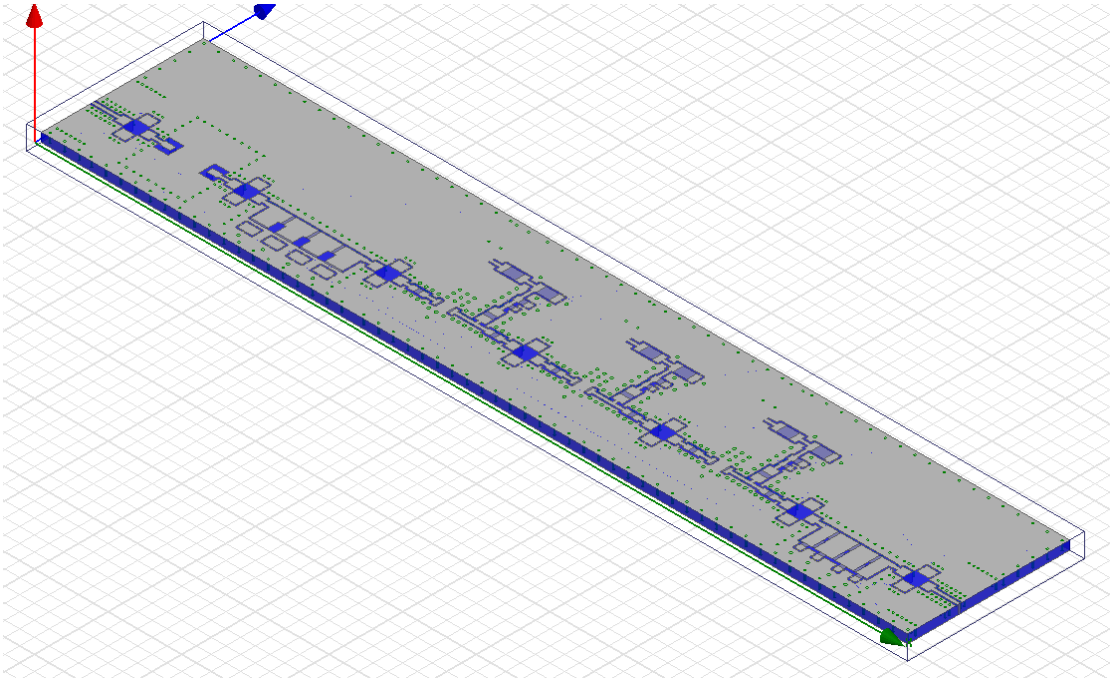

Figure 2-12: HFSS IF Board Design

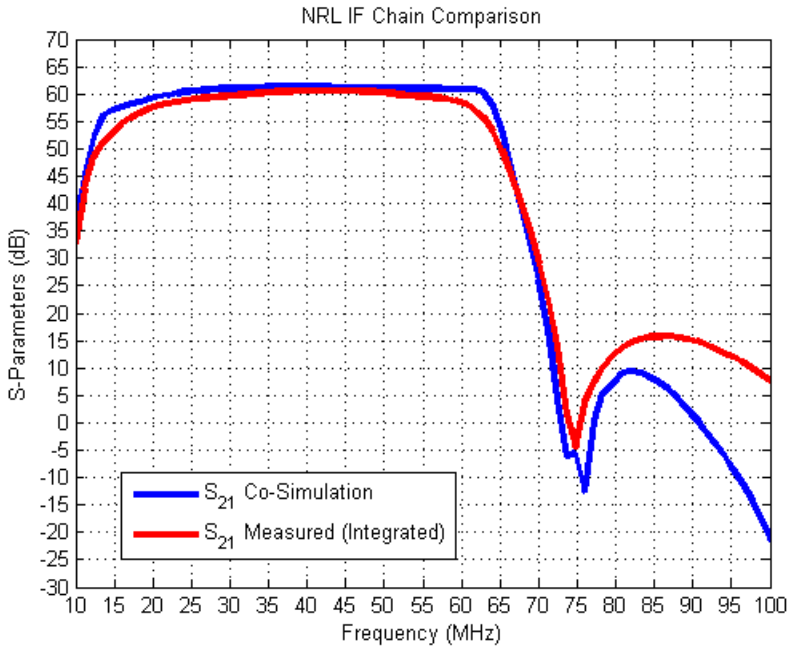

Figure 2-13: Receiver IF Chain Comparison

Figure 2-14 is a photo of the finished IF board which will be integrated into the individual receiver module. The layout was designed on 60 mil thick Rogers 4350b material with 1oz. copper. Because the board would get hot during operation due to all thee high gain IF amplifiers, several holes were milled into the board to mount the board to a heatsink.

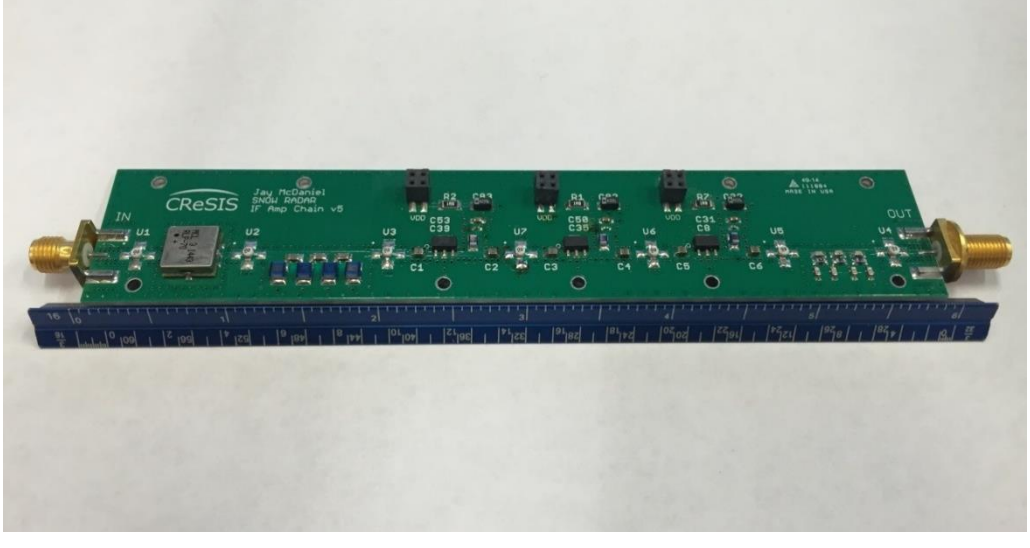

Figure 2-14: Finished and Populated Rx IF Board

A one-fifth size reduction, compared to past designs, was accomplished alone by integrating all of the IF components onto a single board. This also minimized the number of adapters used between the eval boards, greatly reducing the number of reflection with the IF chain. Because the IF filters were designed to meet the specific needs of the system, optimal performance could be achieved through the elimination of any unwanted signals limiting the noise bandwidth. This can be accomplished by setting the Nyquist zone with sharp filter roll-offs. Figures 2-15 and 2-16 show the final measured results of the integrated IF chain as a function of frequency. The S_{11} is greater than 20 dB across the pass band, which again is due to appropriately matching the system components and fine-tuning the integrated board layout. The Figure 2-16 is the measured response of the Nadir Rx IF section. The side-looking measured response is the same, but is 6 dB larger due to the slightly smaller pads between the IF amplifiers.

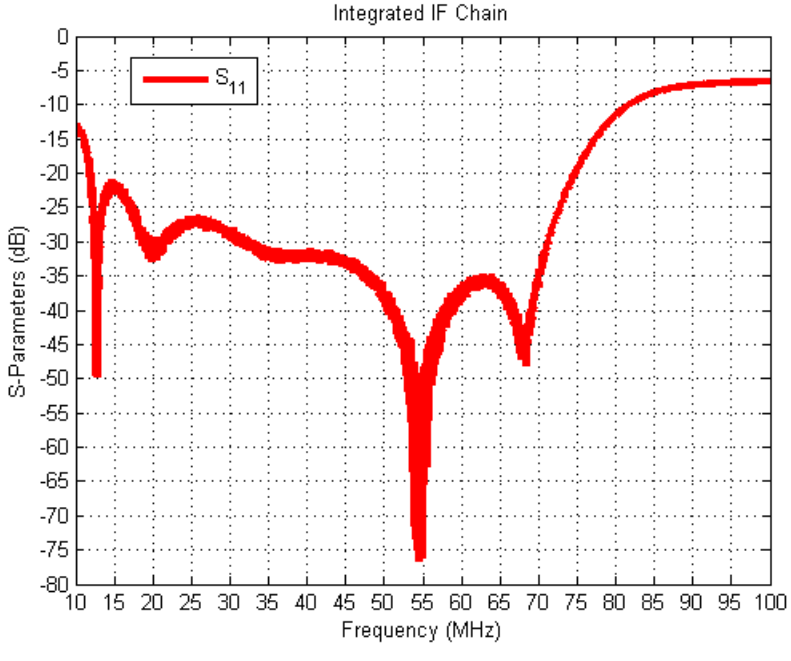

Figure 2-15: Integrated Rx IF Chain S_{11}

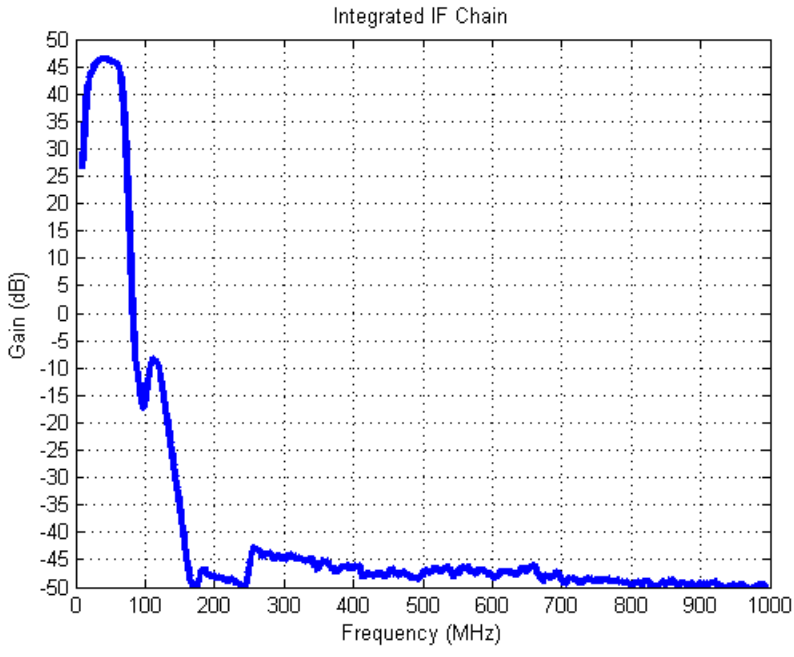

Figure 2-16: Integrated Rx IF Chain S_{21}

2.5 NOISE FIGURE, MDS, AND SATURATION POWER

In this section, several plots will be presented for results calculated using equations from 2.3.1. Because of the wide bandwidth of the system, all of these plots will be as a function of frequency to verify requirements are met for proper performance across the entire 2-18 GHz. The final plots in the section will combine all of these results to show where the expected return signals fall within the sensitivity (lower limit) and saturation power (upper limit).

2.5.1 Noise Figure Plots

In this section, calculated results from equation 2.3 will be plotted as a function of frequency for both Nadir and side-looking receivers. The noise figure is slightly better across the 2-18 GHz for the side-looking receiver because it has 3 dB more gain due to the padding difference between the output of the second LNA and the input of the mixer.

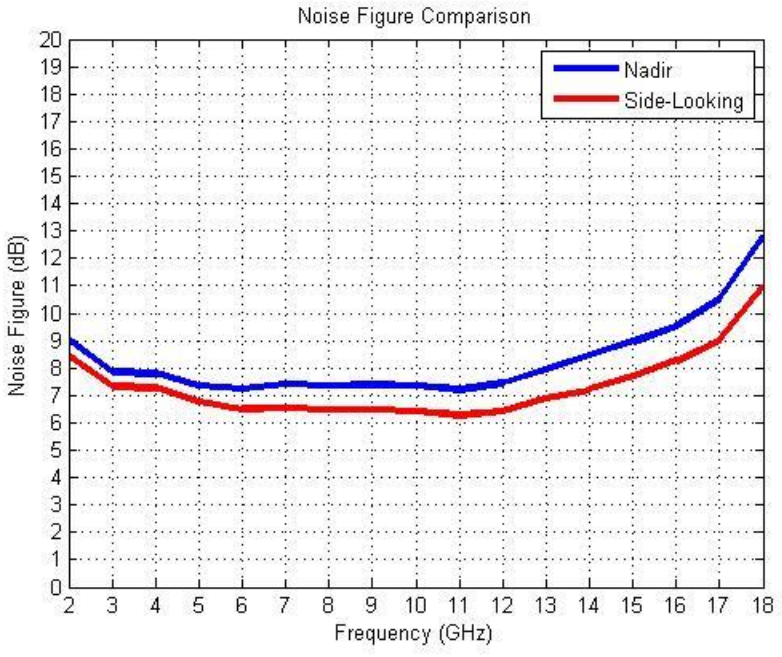

Figure 2-17: Noise Figure versus Frequency

2.5.2 Sensitivity (Minimum Detectable Signal) Plots

In this section, calculated results from equation 2.4 will be plotted as a function of frequency for both Nadir and side-looking receivers. Because the noise figure is slightly better across the 2-18 GHz for the side-looking receiver, the sensitivity will also be slightly better across the 2-18 GHz. However, there is very little difference between the designs.

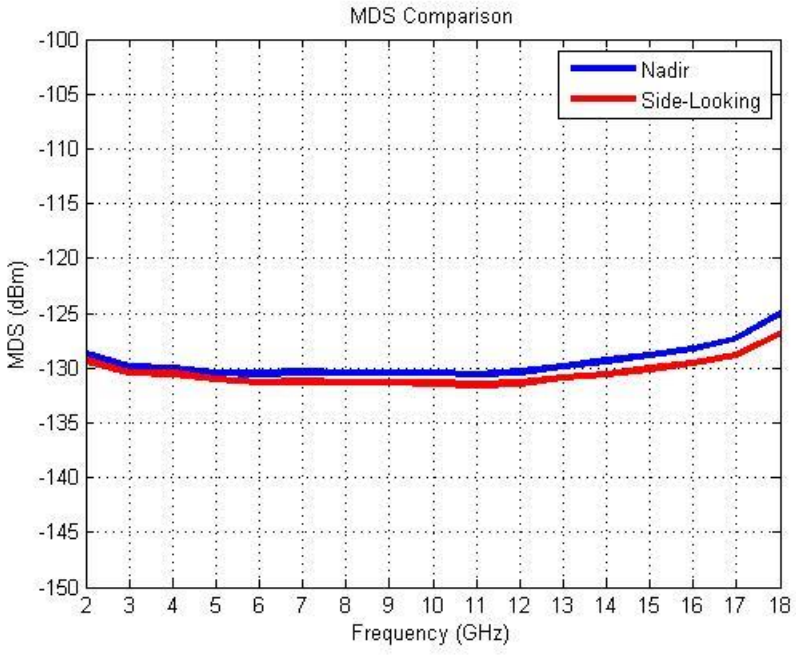

Figure 2-18: Sensitivity versus Frequency

2.5.3 Input Saturation Power Plots

In this section, calculated results for input saturation power will be plotted as a function of frequency for both Nadir and side-looking receivers. Because the gain is slightly higher across the 2-18 GHz for the side-looking receiver, the input saturation power will be slightly lower across the 2-18 GHz; thus, smaller input signal power will be able to saturate the receiver. The receiver was designed so that the first component in the receiver to saturate is the ADC. As long as the system is designed appropriately not to saturate, the signal is guaranteed to fall below the upper edge of the ADC's dynamic range. If the system is starting to saturate, the operator can quickly add a large attenuator at the output of the IF chain and the system performance will stay the same. If an internal or intermediate component starts to saturate first, there are two options. First, the pad can be changed to a larger value where the system is saturating. However, this may be difficult if the pad is integrated onto the board or unreachable. The second option is to put a pad at the input

of the RF chain. However, doing this will affect the noise figure and ultimately reducing the sensitivity. Figure 2-19 plots the input saturation powers versus frequency that will cause the ADC to start saturating.

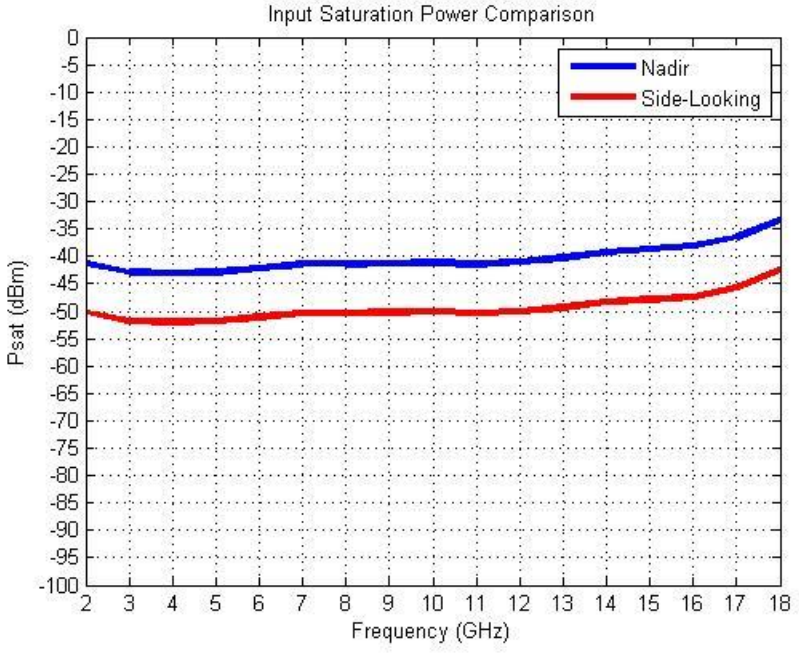

Figure 2-19: Nadir Input Saturation Power versus Frequency

2.5.4 Final Link Budget Results

In this section, the sensitivity, input saturation power, and the expected input signal powers calculated from the link budget equations in section 2.2.1 and 2.2.2 will be plotted on the same plot. This will verify that the system is designed correctly to detect the smallest signals expected while not saturating when measuring the largest signals expected is done. This process is absolutely necessary when designing a new system to make sure optimal performance is achieved while measuring any expected signal. Figure 2-20 shows the first case as discussed in 2.2.1 when flying at 500 ft. and expecting a large specular return from a lead. The return signal power is below the input saturation power. Through this method, large specular returns can be detected from leads and used for system calibration, effectively modeling the system response.

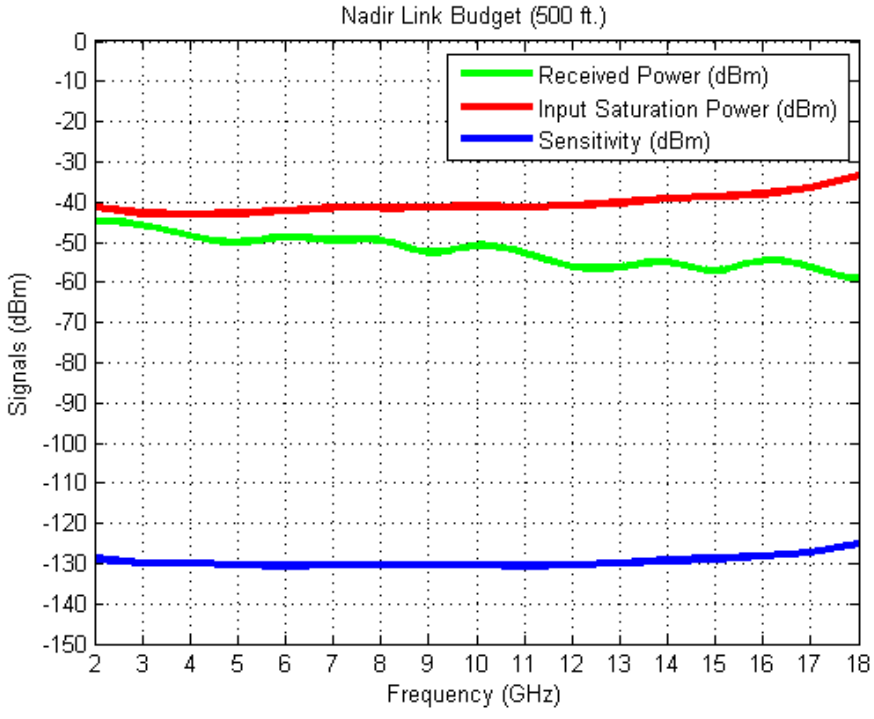

Figure 2-20: Nadir Specular Link Analysis versus Frequency

Figure 2-21 is the second scenario discussed in 2.2.1 when flying at 5000 ft. and expecting a diffuse signal return. This plot shows that the signal will be barely detectable at 5000 ft. However, the Twin Otter is typically flown at 1300-1500 ft. so detecting signals at this flight altitude will rarely be needed.

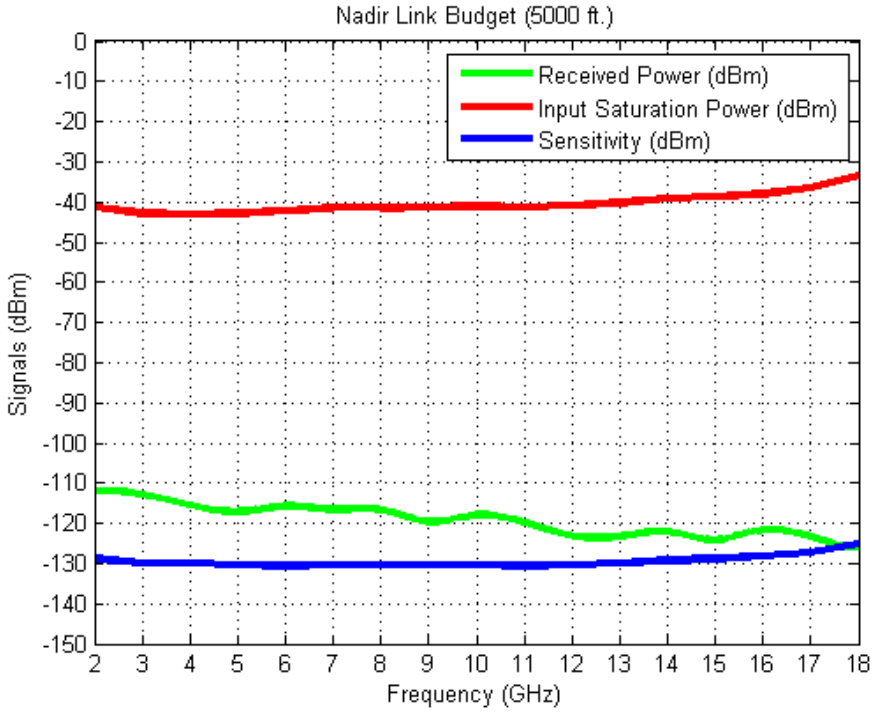

Figure 2-21: Nadir Diffuse Link Analysis versus Frequency

Finally, figure 2-22 is the last scenario discussed in 2.2.2, in which the transmitter is switched from nadir to side-looking. In this scenario, non-specular volumetric backscatter signal returns is expected from 30 degrees off nadir. IF the reflection coefficient is equal to the noise equivalent return of -30 dB, signals from side-looking can theoretically be detected, as long as the Twin Otter flies at 500 ft. If higher altitude is desired, the antenna gain or transmit power will need to be increased to achieve minimal SNR at higher altitudes.

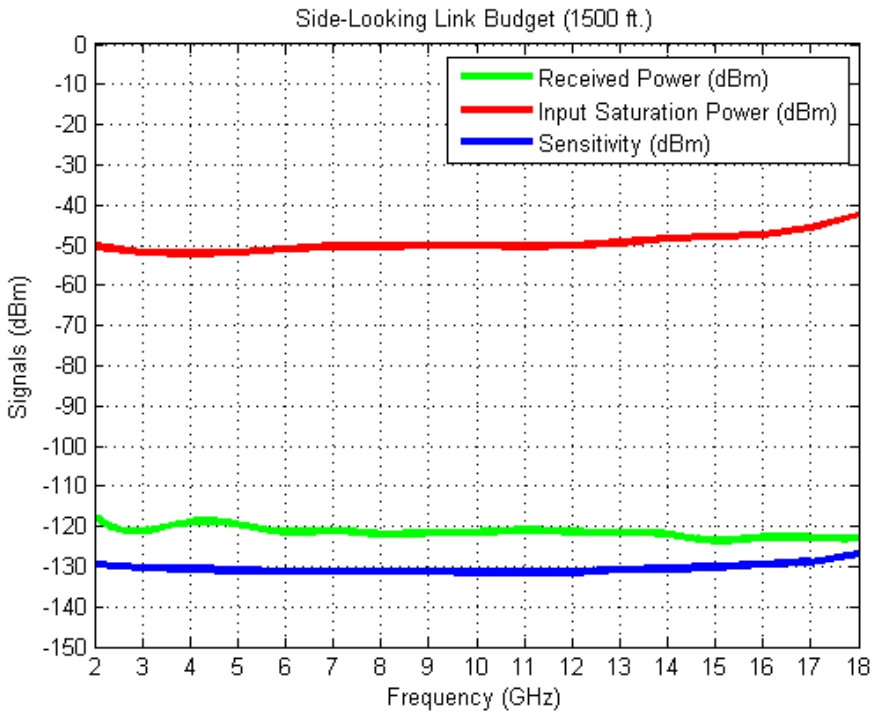

Figure 2-22: Side-Looking Link Analysis versus Frequency

2.6 LO DISTRIBTUION

The chirp from FM2 is fed into an AGC amplifier located inside the Tx chassis, which compensates for its respective gain variations. After compensation, this chirp is fed out of the transmitter chassis and into the LO distribution input of the Rx chassis, where the signal is amplified and divided to feed all the mixers. The block diagram of the LO distribution is shown in figure 2-23. The LO drive power for the mixer is 7 dBm to 13 dBm. It is important to meet this power requirement because for every 1 dB out of the LO drive power range, the LO Conversion Loss (CL) increases by 1 dB. This attenuates the signal and will raise the noise floor. Plot of signal amplitude versus frequency have been provided for the signal going directly into the mixer in figure 2-24. A Hewlett Packard 437B power meter was used to measure the average power for the signal mentioned above. The output of the LO distribution directly to mixer was measured and an average output power of 10dBm was accomplished.

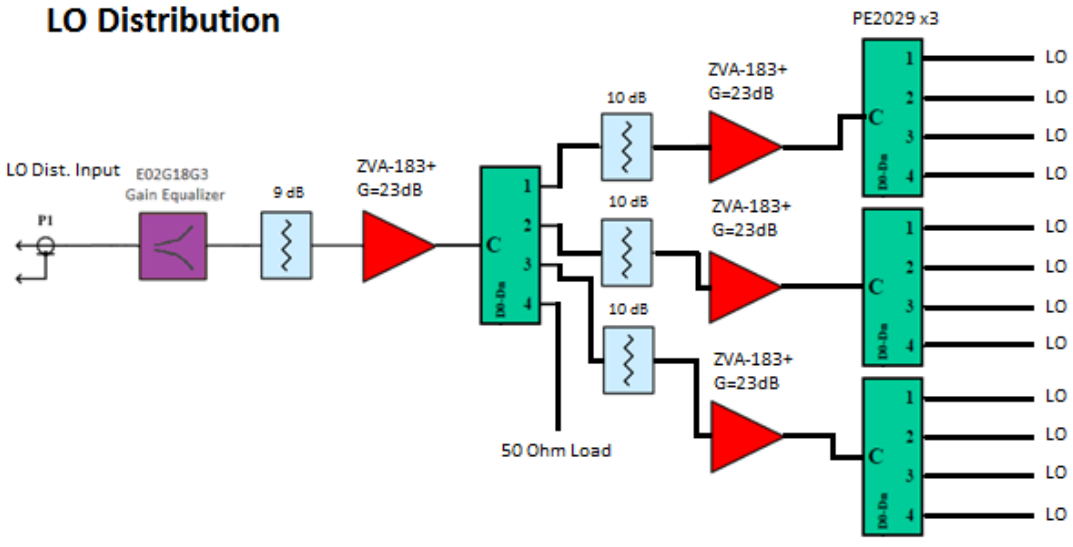

Figure 2-23: LO Distribution Block Diagram

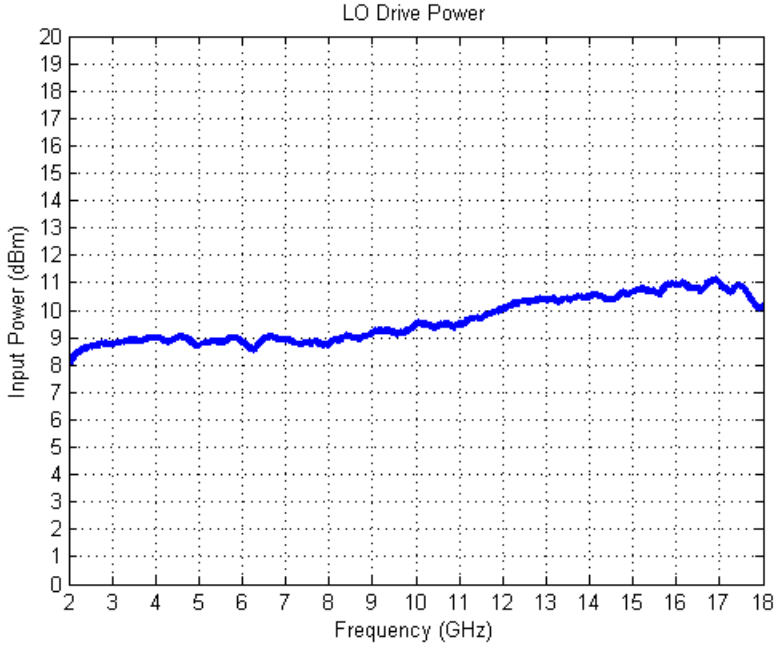

Figure 2-24: Mixer Input LO Power

2.7 MECHANICAL INTEGRATION

The final section of this chapter will briefly discuss the mechanical integration of the receiver chassis with photos of the final deliverable. Because several receivers would need to be integrated into a single chassis, the individual integrated and miniaturized receivers were designed to fit within a fully enclosed receiver case. Figure 2-25 shows the original prototype of the receiver and the final version of the integrated receiver. The point of doing this was to make the receivers modular so they could easily slide in and out of the chassis as needed. In figure 2-26, a front view shot of the receiver chassis is shown.

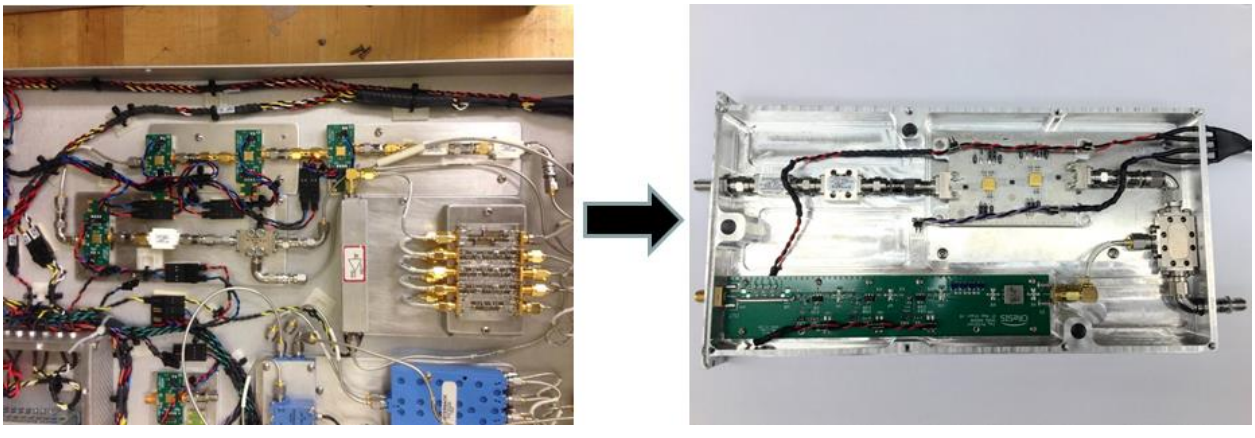

Figure 2-25: Original Rx Prototype and the Final Integrated Rx

Figure 2-26: Receiver Chassis Front View

The individual receiver modules can slide into individual compartments located on the front of the chassis. The 4U case shown can hold up to 18 individual receivers in total. Given this design, it is easy to add or subtract receivers according to the mission demands. On front panel, a switch was incorporated into the design with indicating LED when the chassis is turned on. When the switch is flipped to the ON position, all power supplies are turned on at the same time. No turn on procedure was necessary for the amplifiers chosen. Also, two additional SMA inputs are located at the top right of the chassis. The top SMA is the LO distribution input, and the bottom SMA is a spare in case modifications need to be made in the field.

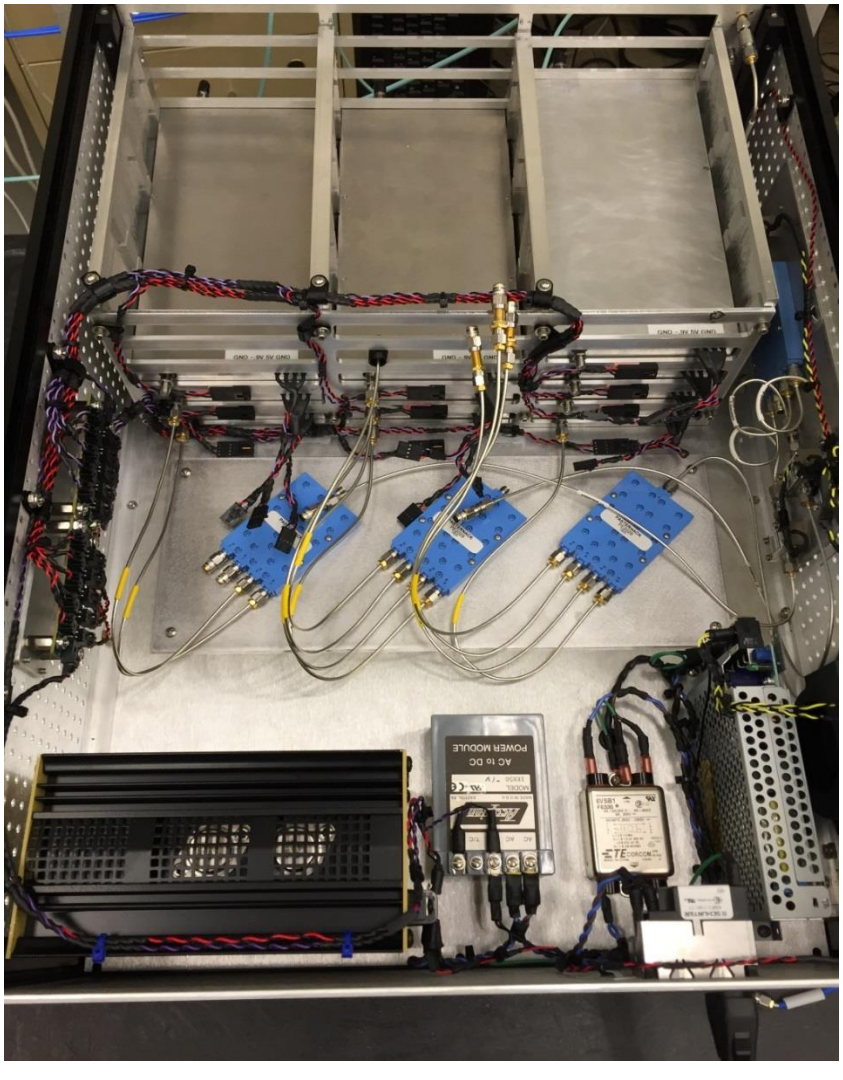

Figure 2-27: Receiver Chassis Top View from Back

Figure 2-27 above provides a detailed look at the inside of the Rx chassis. With the lid removed, the structure designed to hold the receivers can be seen. The four metal walls that create the housing structure for the receivers have grooves milled into them that the receivers slide into. The bottom of the receiver case has a fin that sticks out slightly to accomplish this task. On the back side of the chassis, three power supplies that were used. The far left supply is a 5 V (5A) linear supply from Acopian (model #: A5MT510). Next to it is a -1 V (50mA) mini-encapsulated linear power supply from Acopian as well (model #: I17345). The far right supply is a +12 V (2.5A) ultra-low noise switch power supply from Daitron (model #: HFS30-12). The incoming AC signal is fed through and AC filter and then into the AC-DC power supplies. After the power was converted to DC, the wires were carefully ran within the case as to not cross clean filtered DC across noisy unfiltered AC. Although all the cables used for LO distribution were shielded cables providing high isolation, separation of DC wires and coaxial cables was accomplished where possible.

On the far left wall, there are two boards that were designed for power distribution. The first board takes in a single 5 V DC supply and distributes it into 10 outputs. The second board does the same for the -1 V supply. This minimizes the need for splicing and allows for a clean look. It also reduces concerns of losing power due to a loose splice and the C-grid builds in polarity protection because they can only be plugged in one way. DC power is wired over to the back panel of the receiver housing where power could be connected to the back side of the receiver modules.

The LO distribution chain was screwed onto a metal plate which was then mounted onto the right wall of the chassis. Holes in the metal plate aligned with holes drilled into the case so now new modifications to the case needed to be done. The metal plate was cut from a thicker stock of aluminum to also act as a heatsink. A 12 V fan was mounted on the right side of the case to

blow hot air created by the amplifiers used in the LO distribution. It should also be noted that all of the LO distribution cables are the same model and length as well as all of the power dividers. The reason for this is so that all of the mixers see the same signal at the input to the mixer at the same time. Additionally, notice that a metal plate was used to mount the power dividers and then screwed into a false bottom allowing for future expansion if additional power splitters are needed. The idea of a single configurable case for future expansion was a key concept during the design. Figure 2-28 shows the inside of the Rx chassis from another view. This view shows more of the LO distribution and how it is mounted to the side wall.

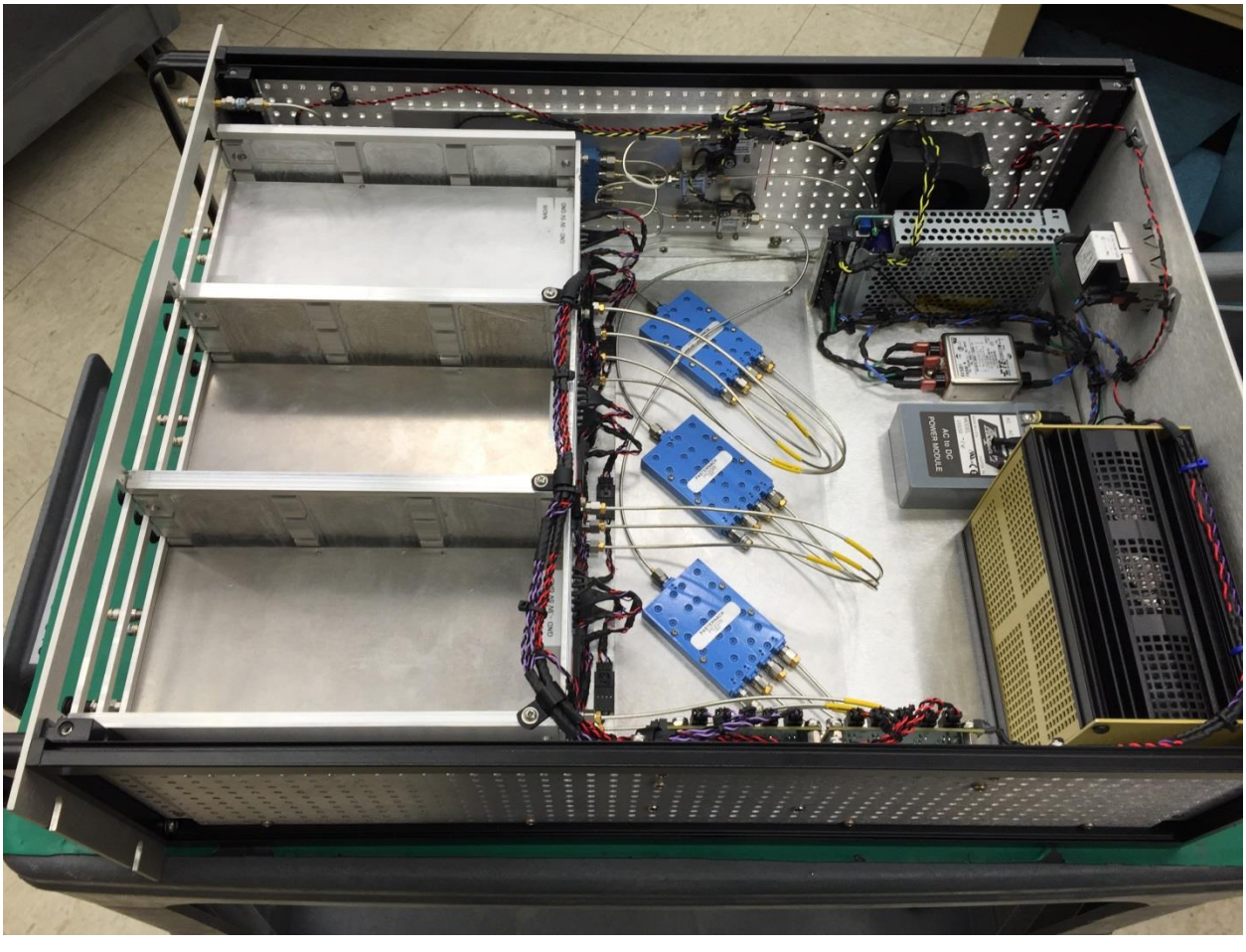

Figure 2-28: Receiver Chassis Top View from Side

TABLE 2-1
SNOW RADAR RECEIVER PARTS LIST

Quantity	Manufacturer	Model	Description	Data Sheet
4	Mini-Circuits	BW-SXW2+	DC-18 GHz Attenuators	[28]
2	Hittite	HMC463LH250	2-20 GHz AGC LNA	[29]
1	AMTI	H02G18GD	2-18 GHz HPF	[30]
1	AMTI	L18G20G2	DC-18 GHz LPF	[31]
1	Miteq	DB0218LA1-R	2-18 GHz Mixer	[32]
7	Mini-Circuits	PAT-X+	DC-7 GHz Attenuators	[33]
1	Mini-Circuits	RLP-70+	DC-70 MHz LPF	[34]
1	CReSIS	v1	15 MHz HPF	
3	Hittite	HMC580ST89	DC-1 GHz IF Amp	[35]
1	CReSIS		62.5 MHz LPF	
2	CReSIS		Power Distribution Board	
1	Acopian	A5MT510	5V (6A) Power Supply	[36]
1	Acopian	I17345	-0.9V (50mA) Supply	
1	Techmar	4U	Metal Chassis	

TABLE 2-2
LO DISTRIBUTION PARTS LIST

Quantity	Manufacturer	Model	Description	Data Sheet
5	Mini-Circuits	BW-SXW2+	DC-18 GHz Attenuators	[28]
4	Mini-Circuits	ZVA-183+	DC-18 GHz Amp	[37]
4	Pasternack	PE2029	4:1 Power Divider	[38]
1	Daitron	HFS30-12	12V (2.5A) Power Supply	[39]

3 TRANSMITTER DESIGN

3.1 SYSTEM REQUIREMENTS

For the NRL mission in March 2015, there was a set of system requirements for the new integrated Snow Radar transmitter. The new transmitter needed to transmit the entire 2-18 GHz bandwidth and meet the power requirements at the output which were determined above. The Nadir transmit power needed to transmit at 20dBm while the side-looking transmit power needed to be 34dBm. The entire transmitter also needed to be integrated into a single 2U chassis in order to meet the size requirements allotted. The rest of this chapter is designated to the design and integration of the transmit chain.

3.2 TRANSMITTER DESIGN

This section will heavily rely on figure 1-12 from chapter 1. The front panel of the transmitter chassis has 8 SMAs for input/output (I/O). Two RF input SMA terminals are for bringing in a signal from each of the frequency multipliers. The chirp from FM1 will be for the transmit chain and the chirp from FM2 will be for the LO distribution chain. There are also two input SMAs for the LO and TX compensation section for each corresponding chain. The final input SMA is for the Tx switch, which alters between Nadir and Side-Looking. Lastly, there are two output SMAs; one which connects to the Nadir Tx antenna and one which connects to the side-looking Tx antenna.

The chirp from FM1 is instantly fed into an amplifier with automatic gain control (AGC), which allows for gain compensation of the chirp. This is done by changing the control voltage, which alters the gain, in time with the chirp to compensate for variations in the generated chirp. Essentially, the chirp is flattened to the lowest value to get a constant amplitude versus frequency. After compensation, the signal is sent through a switch which alters between Nadir and side-

looking. A decoder board was designed and developed at CReSIS and attached to the switch. After the switch, the signal is filtered and amplified to produce the required output power. Figure 3-1 shows the signal amplitude versus frequency for both Nadir and side-looking.

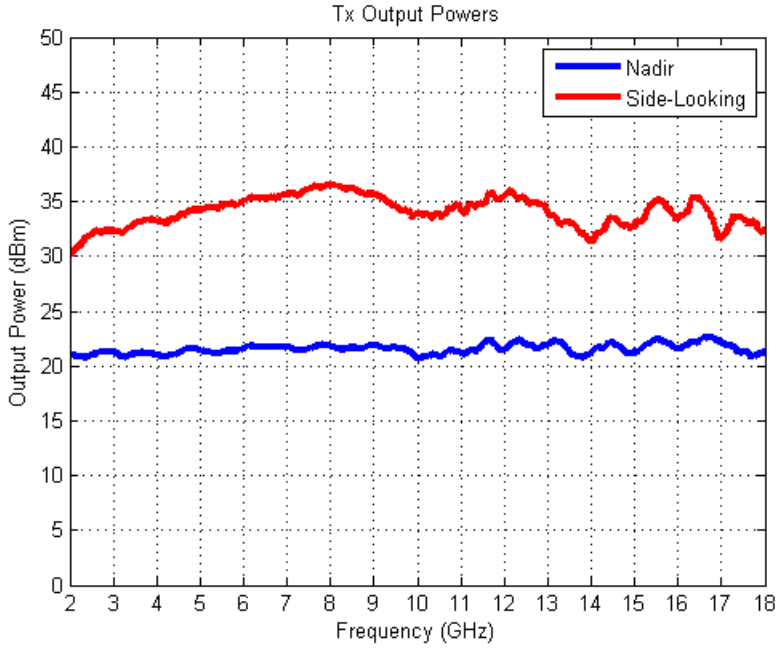

Figure 3-1: Transmitter Output Powers for Nadir and Side-Looking

A Hewlett Packard 437B power meter was used to measure the average power for each of the signals mentioned above. The output of the Nadir Tx chain had an average output power of 20 dBm and the output of the side-looking Tx chain had an average output power of 34 dBm. Both of these values matched what is noted in the link budget.

3.3 MECHANICAL INTEGRATION

In figure 1-12, several voltages were needed for all of the individual amplifiers. A voltage regulator board was designed and developed at CReSIS so only a single output +5V and dual output +/-12V Daitron ultra-low noise switching power supply was needed. All three of the supply

voltages were fed into the regulator and +5V, +7.5V, +12V, -.75V, -1V, and -12V were outputs of the board. This significantly reduced the weight and complexity of wiring inside the chassis.

Both transmit chains were attached to a common false bottom which served a multitude of purposes. First, it provided a common ground for all of the connectorized components. Second, it acted as a heatsink for some of the high power amplifiers which heated up quickly during testing without the plate. Finally, it kept the case from being destroyed allowing for it to be used in the future if design changes are made. The 8W power amplifier was also mounted off of the case floor to allow air to be pulled in by the fans located on the bottom of its case. Several fans were located on the back plate of the chassis to pull in air and keep components cool during operation. A switch was placed on the front plate to turn on/off the chassis along with an indicating LED. A photo of the finalized Tx chassis is shown in figure 3-3. Table 3-1 includes a parts list of all the components used in the transmitter chassis. There are no filters included in the transmitter chassis. Filtering is performed through the frequency multiplier and antennas.

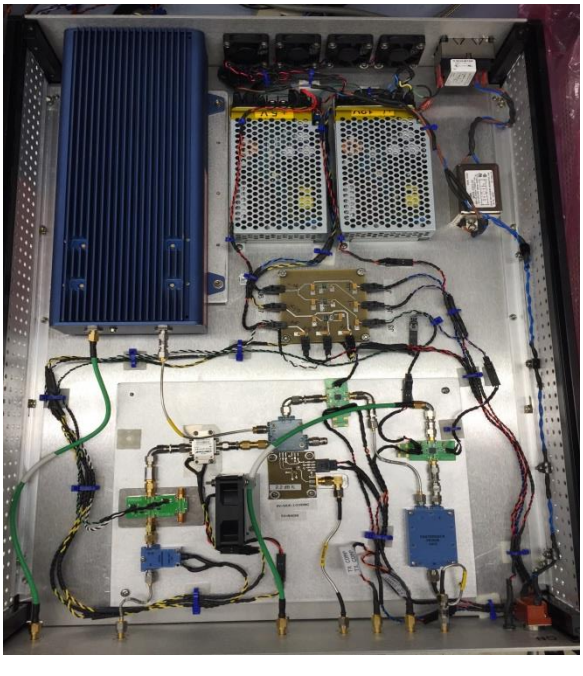

Figure 3-2: Snow Radar Transmitter Chassis

TABLE 3-1
SNOW RADAR TRANSMITTER PARTS LIST

Quantity	Manufacturer	Model	Description	Data Sheet
2	Hittite	HMC463LP5	2-20 GHz AGC LNA	[40]
1	Narda	SP133DHS	SP3T 2-18 GHz Switch	[41]
1	RF Lambda	RAMP01G22GA	1-22 GHz 8W (AC) Amp	[42]
1	Mini-Circuits	ZVA-213+	1-21 GHz High Gain Amp	[43]
1	Hittite	HMC998LP5E	.1-20 GHz 2W Amp	[44]
1	CReSIS	v1	Decoder Board	
1	CReSIS	v1	Regulator Board	
1	Daitron	HFS30-5	5V (6A) Power Supply	[45]
1	Dairton	HFD30-12	+12V (2.2A) -12V (.3A)	[46]
1	Techmar	2U	Metal Chassis	

4 PASSIVE COMPONENT DESIGN

4.1 SUSPENDED SUBSTRATE STRIPLINE FILTERS

Because of the rise for wider bandwidth radars for finer range resolution, there is increased demand for UWB passive component design, especially filters. A generalized Chebyshev lowpass filter prototype is used, due to its ability to have transmission zeroes at infinity along with remaining transmission zeroes at finite frequency points. This allows for superior selectivity. As noted in [18], filter realization on printed circuit boards while maintaining high selectivity is feasible, due to the typical impedance variation of 2:1 for the Chebyshev prototype being much less than the 10:1 variation experienced in elliptic prototypes. For this specific design, an equiripple passband response with “three” transmission zeroes at infinity and the rest at a finite frequency prototype is used. From this prototype, Richards Transformation is applied to transform

this lumped element prototype to a distributed lowpass filter with a cutoff frequency of 18 GHz and high pass filter prototype with a cutoff frequency of 2 GHz.

In this sub-chapter, the design of "Super" UWB Suspended Substrate Stripline filters will be discussed. There are several advantages to SSS including high performance, low cost, and low insertion loss [19]. Because most of the fields are captured in the air between the case and substrate, minimum dispersion is experienced across wide super bandwidths allowing for large passbands. Also, the use of thin RT/Duroid substrates allows for minimal board loss, temperature stability, and constant high frequency dielectric properties for wide bandwidth applications.

At the end of each section, measured results of the final product are compared against the simulated results as well as against purchased filters. Due to exceptionally long lead times and price demands for large bandwidth filters, these in house filters will be used in place of purchased filters in the future to reduce cost for future multi-channel expansion and eliminate lead time delays.

4.1.1 GENERALIZED CHEBYSHEV LOWPASS FILTER PROTOTYPE

The generalized Chebyshev lowpass filter prototype that will be repeatedly referenced to is given in figure 4-1. In [18], the alternating pole technique is used to solve for the element values along with Wo and W1. The N=11 (table IV) chart was used for RL ≥ 20 dB and I.L. ≥ 50dB. Table 4-1 provides the values mentioned above.

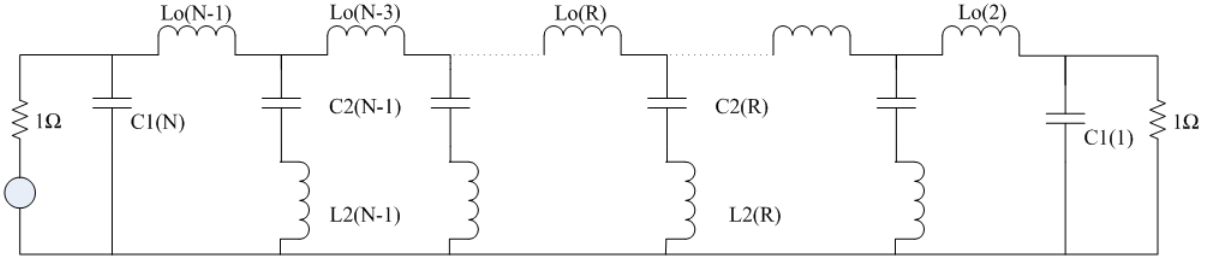

Figure 4-1: Generalized Chebyshev Low Pass Filter Prototype

TABLE 4-1
LOW PASS PROTOTYPE ELEMENT VALUES

R	Element	Value
11	$C_1(11)$	1.04297
	$L_0(10)$	.935065
10	$L_2(10)$	.984313
	$C_2(10)$	.787121
	$L_0(8)$	.786767
8	$L_2(8)$	.794605
	$C_2(8)$	.975041
	$L_0(6)$	.807267
6	$L_2(6)$	.794605
	$C_2(6)$	.975041
	$L_0(4)$	.786767
4	$L_2(4)$	.787121
	$C_2(4)$	.984313
2	$L_0(2)$	.935065
1	$C_1(1)$	1.04297
W_0		1.13609
W_1		1.06853

4.1.2 Low Pass Filter

In this section, the generalized Chebyshev lumped element lowpass prototype will be transformed into a distributed lowpass prototype using the Richard's Transformation [20]:

$$s = j\omega_o \tan(a\omega) \tag{4.1}$$

Above, where *s* is the complex frequency variable and *a* is a constant. Taking a single section of the generalized lowpass filter and solve for the admittance results in the following:

$$Y = \frac{sC}{1 + \frac{s^2}{\omega_o^2}} \tag{4.2}$$

W_o^2 is the resonance frequency of the given section. Apply the Richards Transformation to equation 4.2 results in:

$$Y = \frac{j\omega_0 C tan(2a\omega)}{2} \tag{4.3}$$

From [21], the input admittance for a shunt open circuit stub is:

$$Y_{in} = jY_o \tan(\beta l) \tag{4.4}$$

The above is identical to the admittance of the individual lowpass prototype section. This means that the lumped element capacitors can be realized as shunt open circuit stubs. In equating 4.3 and 4.4, it is apparent that

$$a = \frac{l}{2v} \tag{4.5}$$

given

$$\beta = \frac{\omega}{v} \tag{4.6}$$

Notice, it can also be stated that:

$$Z_o(R) = \frac{2}{\omega_o C(R)} \tag{4.7}$$

Rearranging equation 4.1, it is shown:

$$\Omega = \frac{\omega}{\omega_o} = \tan(a\omega) = \tan(2\pi f a) \tag{4.8}$$

If evaluated at the cutoff frequency becomes:

$$\Omega = 1 = \tan(2\pi f_c a) \tag{4.9}$$

Inserting equation 4.5 into 4.9 and solving for l results in:

$$l_1 = \frac{v}{\pi f_c} tan^{-1}\left(\frac{1}{\omega_o}\right) \tag{4.10}$$

where

$$v = \frac{c}{\sqrt{\varepsilon_e}} \tag{4.11}$$

and *c* is the velocity of propagation in free space.

In [22], closed form analysis equations are developed for SSS and Broadside coupled structures. The characteristic impedance Z_o is derived as

$$Z_o = \eta_o \left[V + R\left(\frac{W}{b} + 1.3930 + 0.6670 * ln\left(\frac{W}{b} + 1.444\right)\right)^{-1}\right] \tag{4.12}$$

where $\eta_o = 120\pi$ and

$$V = -0.6301 - 0.07082\frac{h}{b} + 0.2470\frac{a}{b} \tag{4.13}$$

$$R = 1.9492 + 0.1553\frac{h}{b} - 0.5123\frac{a}{b} \tag{4.14}$$

where *a* is the width of cavity, *b* is height of cavity, and *h* is the thickness of the substrate. Setting Z_o to be 50 Ω and solving for *w*, gives a 50 Ω transmission line. While using a 5 mil thick Rogers 6002 RT/Duroid substrate with a dielectric constant $\varepsilon_r = 2.94$ and a loss tangent$\delta = .0012$, and setting *a* = *b* = 70 mil, parameters, $w = 58.6\ mil$. Once the 50 Ω width is known, one can solve for the effective dielectric constant ε_e as:

$$\sqrt{\varepsilon_e} = \left(1 + \left(E - F * ln\frac{W}{b}\right) * ln\frac{1}{\sqrt{\varepsilon_r}}\right)^{-1} \tag{4.15}$$

where

$$E = 0.4640 + 0.9647\frac{h}{b} - 0.08364\frac{a}{b} \tag{4.16}$$

$$F = -0.1424 + 0.3017\frac{h}{b} - 0.02411\frac{a}{b} \tag{4.17}$$

Using the same parameters as above in addition to width, the effective dielectric constant can be solved for. Given $w = 58.6$ mil, the effective dielectric constant is $\varepsilon_e = 1.5242$. Plugging this value back into equation 4.11, it can be stated that $v = 2.43 * 10^8 \ \frac{m}{s}$. Now that v is known, the lengths of the inner shunt open circuit stubs can be solved. From [18], the lengths of the outer shunt open circuit stubs are $l_2 = \frac{l_1}{2}$. These distributed parameters have been solved and are shown in table 4-2

From [19], the TEM-Mode transmission line characteristic impedance is related to the static capacitance to ground as

$$\frac{Z_o}{\sqrt{\varepsilon_r}} = \frac{\eta_o}{(C/\varepsilon)} \tag{4.18}$$

where $\frac{C}{\varepsilon}$ is composed of the parallel plate capacitance $\frac{C_p}{\varepsilon}$ and fringing capacitance $\frac{C_F}{\varepsilon}$ as

$$\frac{C}{\varepsilon} = \frac{2C_p}{\varepsilon} + \frac{4C_F}{\varepsilon} \tag{4.19}$$

$\frac{C_F}{\varepsilon}$ can be found from figure 5 in [23] and

$$\frac{C_p}{\varepsilon} = 2 * \frac{W/b}{1 - t/b} \tag{4.20}$$

where W and t are the width and thickness of the strip conductor respectfully. For this configuration, $\frac{C_F}{\varepsilon}$ was found to be .54. Substituting equation 4.20 into 4.19 and then substituting that into 4.18 and solving for *W* obtains:

$$W = \frac{b-t}{4}\left(\frac{\eta_o}{Z_o(R)\sqrt{\varepsilon_r}} - 4\frac{C_F}{\varepsilon}\right) \tag{4.21}$$

By choosing a substrate with a dielectric constant close to one and making sure $b \gg t$, then $\sqrt{\varepsilon_r} \approx 1$. When equation 4.7 is substituted into 4.21 and scaled for 50 Ω terminations, equation 4.21 becomes:

$$W_1 = \frac{b-t}{4}\left(1.2\pi\omega_o C_2(R) - 4\frac{C_F}{\varepsilon}\right) \tag{4.22}$$

Using equation 4.22 and values from table 4-1, the width of the shunt open circuit stubs can be solved. These values have been calculated and are shown in table 4-2.

The lumped inductors become series short circuit stubs after the Richards transformation has been applied and is equivalent to a pi-network [20]. Series impedance of the pi-network is

$$Z = jZ_L \sin\left(\frac{\omega l_L}{v}\right) \approx \frac{2\pi f_c l_L}{v} \tag{4.23}$$

using the small angle approximation for sin(x). Equating 4.23 with the impedance for a series short circuit stub

$$Z = jL_o(R)\omega_o tan\left(\frac{2\pi f_c l}{v}\right) \tag{4.24}$$

the length of the inductive stub can be found as

$$l_L = \frac{L_o(R)\omega_o}{Z_L} * \frac{v}{2\pi f_c} * \tan\left(\frac{2\pi f_c l}{v}\right) \tag{4.25}$$

where l can be proven to be the same as equation 4.10. Rearranging equation 4.21 and solving for Z_o, along with making the substitution of $Z_o = 50 * Z_L$ and using results from equation 4.12 for width (w), Z_L can be solved.

$$Z_L = \frac{7.534}{\frac{4W}{b-t} + 4\frac{C_F}{\varepsilon}} \tag{4.26}$$

All of the series short circuit stubs will have the same width which is the width that yields a 50 Ω characteristic impedance transmission line. Once Z_L has been calculated, values from table 4-1 can be substituted into equation 4.25 and the series short circuit stub lengths can be calculated. The distributed parameters have been solved and are shown in table 4-2.

In table 4-2, notice the symmetry that occurs for the distributed lowpass filter prototype. This symmetry allows for easy tuning because the number of variables is cut in half. Because the series short circuit stubs were designed to have a width which equates to a 50 Ω transmission line, the filter can be tuned to any cutoff frequency by simply tuning the length of the short circuit stubs. However, the four inner stubs are the same length and the two outer stubs are the same length. Therefore, tuning this filter to any cutoff frequency relies on only tuning two lengths. The rest of this section shows the ADS schematic and results as well as the HFSS design and simulated results, first using strictly the theory values calculated, and then after slight tunings have been done to optimize performance.

TABLE 4-2
DISTRIBUTED PROTOTYPE PARAMETERS

R	Type	Length (mil)	Width (mil)
1	Shunt Open Circuit Stub	61.07	37.49
2	Series Short Circuit Stub	60.55	58.6
3	Shunt Open Circuit Stub	122.13	19.68
4	Series Short Circuit Stub	50.94	58.6
5	Shunt Open Circuit Stub	122.13	32.76
6	Series Short Circuit Stub	52.28	58.6
7	Shunt Open Circuit Stub	122.13	32.76
8	Series Short Circuit Stub	50.94	58.6
9	Shunt Open Circuit Stub	122.13	19.68
10	Series Short Circuit Stub	60.55	58.6
11	Shunt Open Circuit Stub	61.07	37.49

Figure 4-2 shows the ADS schematic for the distributed lowpass filter prototype. Because ADS has limited structures for SSS, the stripline model was used and the dielectric constant was set to the effective dielectric constant solved for in equation 4.15. Also, the substrate thickness was set to be the thickness of the cavity as specified earlier in this section. Figure 4-3 shows the simulated results from ADS. The calculated theoretical values result in a filter with very close desired performance. Only minor tuning will need to be done in order to achiever absolute desired performance.

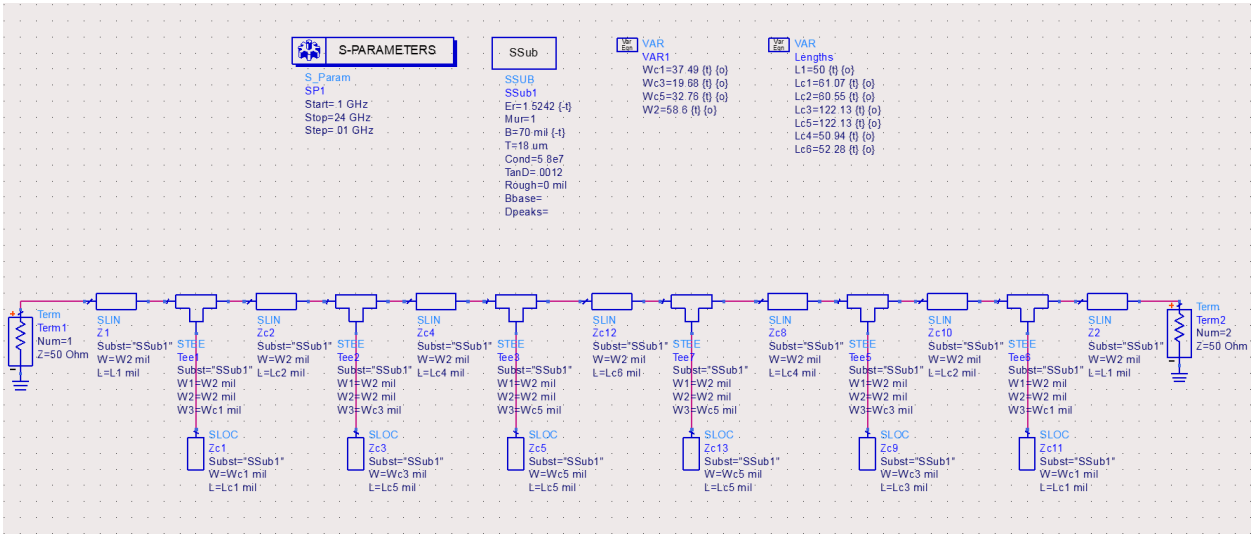

Figure 4-2: ADS Schematic with Calculated Theory Values

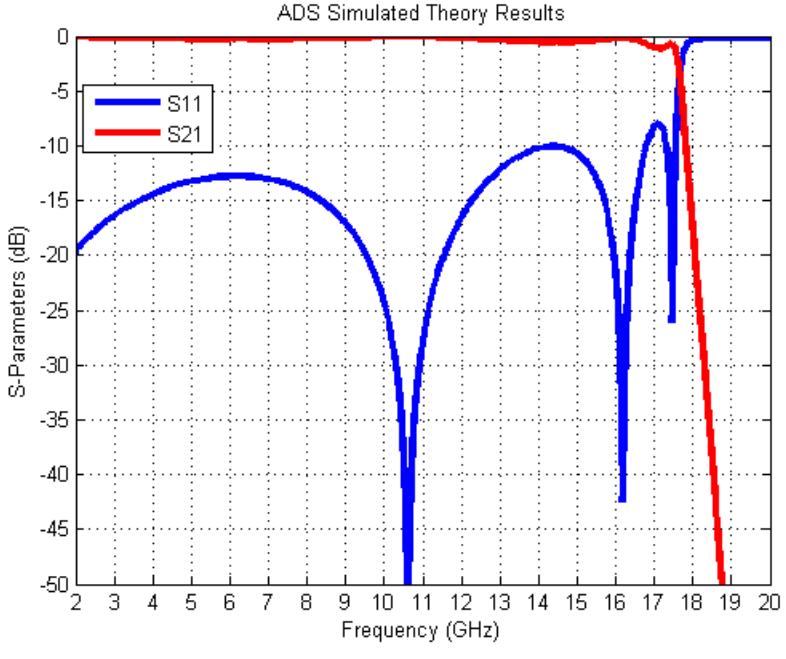

Figure 4-3: ADS Simulated Results with Calculated Theory Values

Figure 4-4 is a screen shot of the filter design in HFSS. The HFSS full EM simulated results are shown in figure 4-5. The ADS design setup gives a very close approximation of the actual SSS layout simulated in HFSS. Therefore, the ADS simulation can be used as a first order approximation for tuning of the distributed parameters.

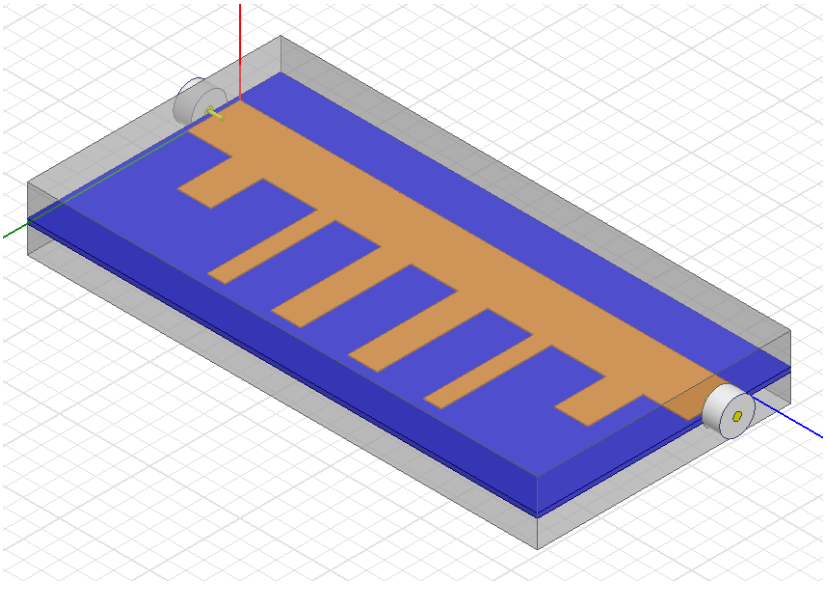

Figure 4-4: HFSS Design with Calculated Theory Values

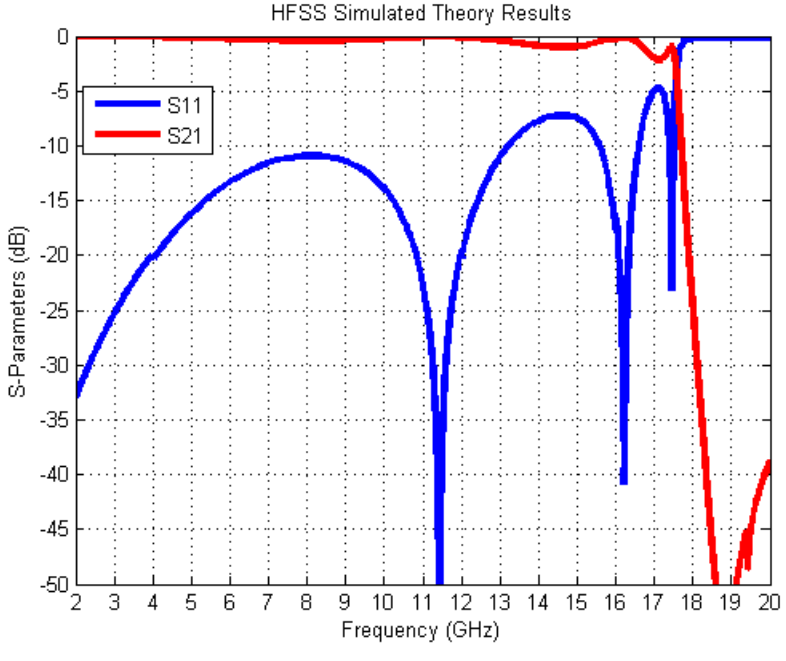

Figure 4-5: HFSS Simulated Results with Calculated Theory Values

Now that the theory values have run in both ADS and HFSS, the filter parameters will be tuned to achieve optimal performance. As mentioned earlier, in order to tune the filter, only the

shunt open circuit stub lengths should need to be tuned. After quick tuning, the inner stub lengths were adjusted to 116.13 mils and the outer stub lengths were tuned to 90.06 mils.

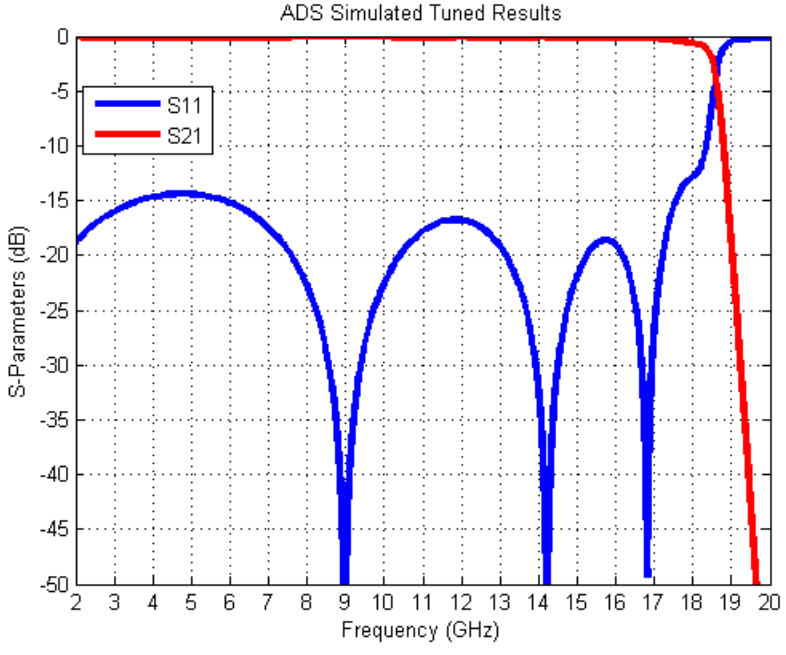

Figure 4-6: ADS Simulated Results with Tuned Values

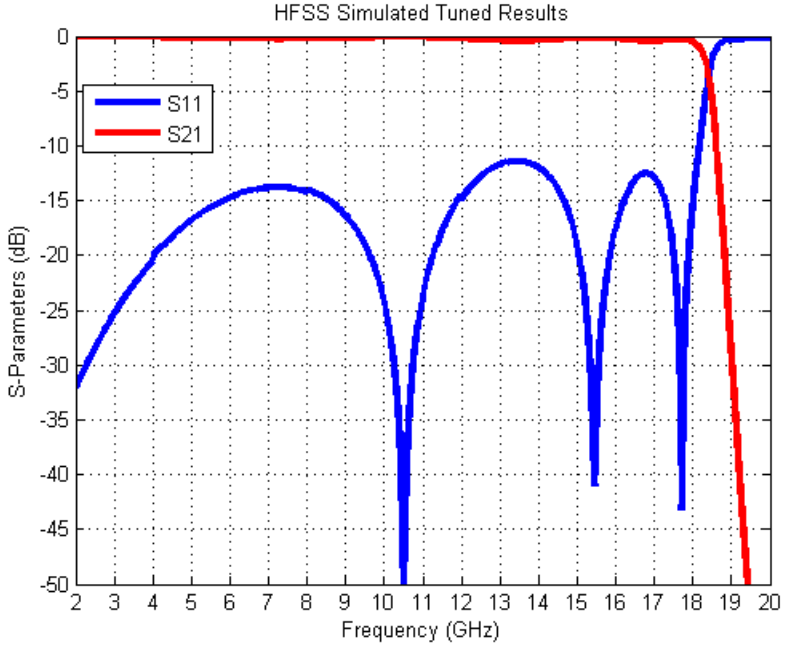

Figure 4-7: HFSS Simulated Results with Tuned Values

After very simple tuning of the stub lengths, the distributed lowpass filter has a cutoff frequency of 18 GHz as desired. It is also clear that the ADS simulation matches the HFSS simulation very well after tuning, again verifying the ADS model for first order approximation. Because ADS is not a full EM finite element simulation, simulations can be run very quickly allowing for the tuning process to be done rather quickly than using the HFSS optimization tool.

In this section, it should be noted that special attention is needed when laying out the HFSS design. The inside of the SSS filter is equivalent to a rectangular waveguide. If the cutoff frequency of the waveguide is low enough in frequency, it will appear as a large notch in the passband and no matter how the stubs are tuned they cannot be removed. Therefore, the cavity should be kept relatively tight around the filter to make sure the waveguide's cutoff frequency is way above the passband. However, placing the cavity too close to the filter can cause additional fringing capacitance and can affect the design. This is especially important in super UWB applications such as this.

Figure 4-8 is a photo of the finished product as well as the filter. Both are compared to a quarter for size reference. Figure 4-9 is a comparison between the measured and HFSS simulated results. The insertion loss is less than 1 dB across the pass band, and the return loss is greater than 10 dB across the passband. The attenuation in the stopband is greater than 60 dB at 20 GHz and greater than 40 dB up to 26 GHz. Figure 4-10 is a comparison between the in-house and purchased LPF. The measured S_{11} is slightly different from the simulated S_{11} due to differences between them. These differences include; incomplete connector model due to proprietary design, soldering of the connector pin to the filter feed line, and mechanical inaccuracies due to non-perfect tolerance. A 10× cost reduction is accomplished by developing the filters in-house. These filters can be made in 2 days eliminating the 8 week lead time for purchased filters.

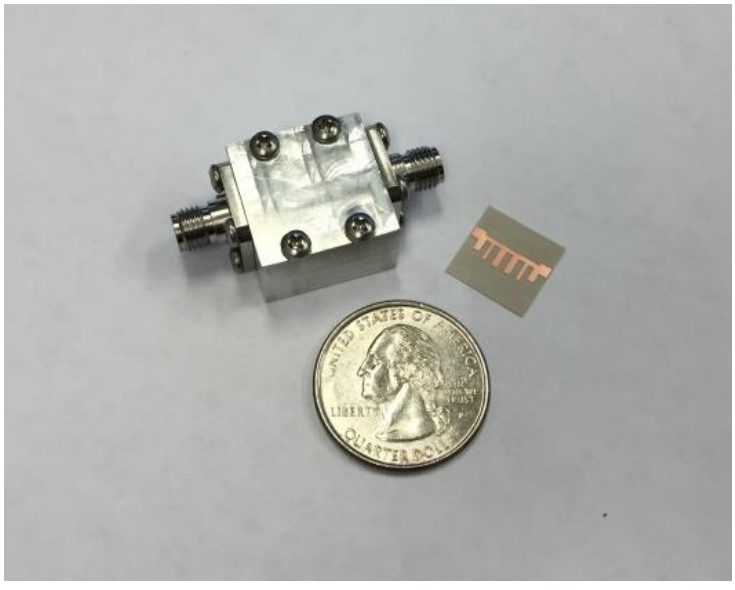

Figure 4-8: LPF Finished Product

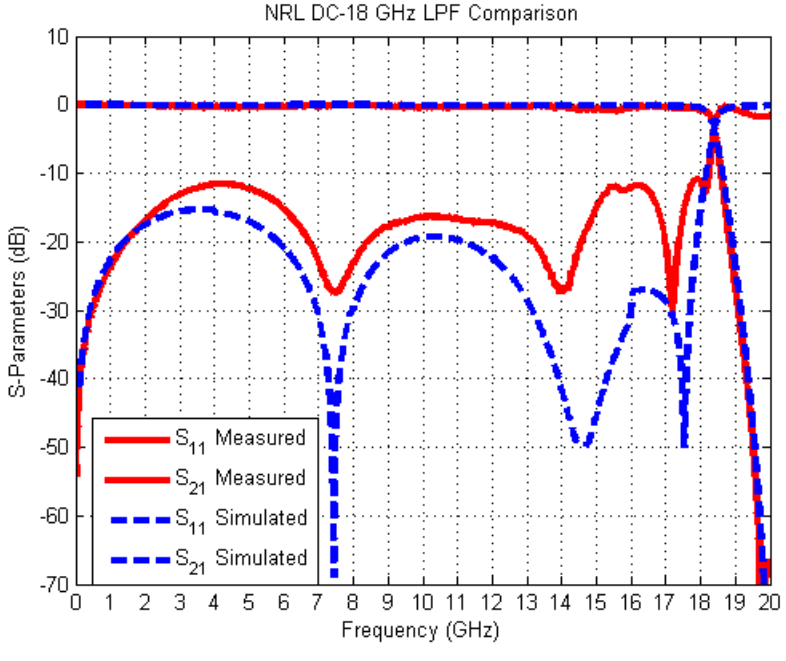

Figure 4-9: DC-18 GHz Measured vs Simulated Comparison

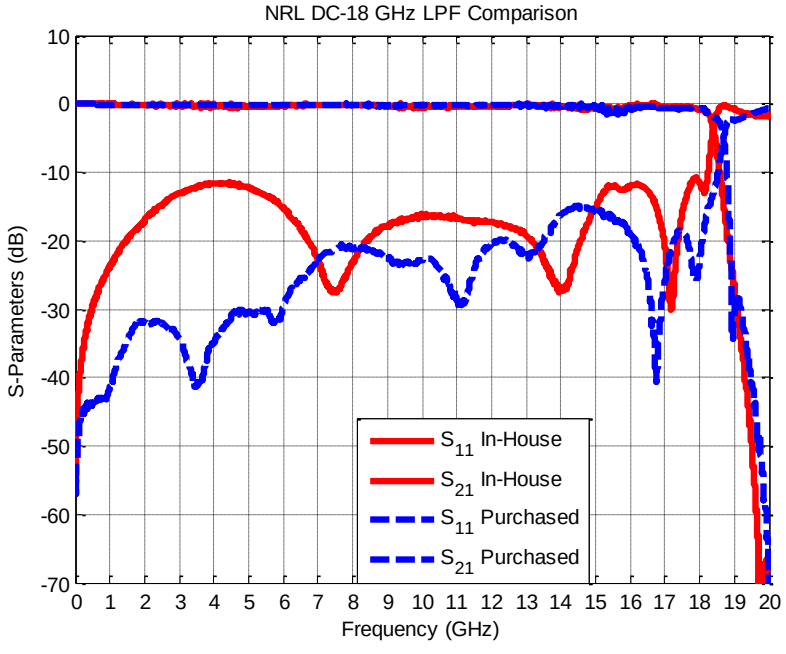

Figure 4-10: In-house Filters vs Purchased Filters Comparison

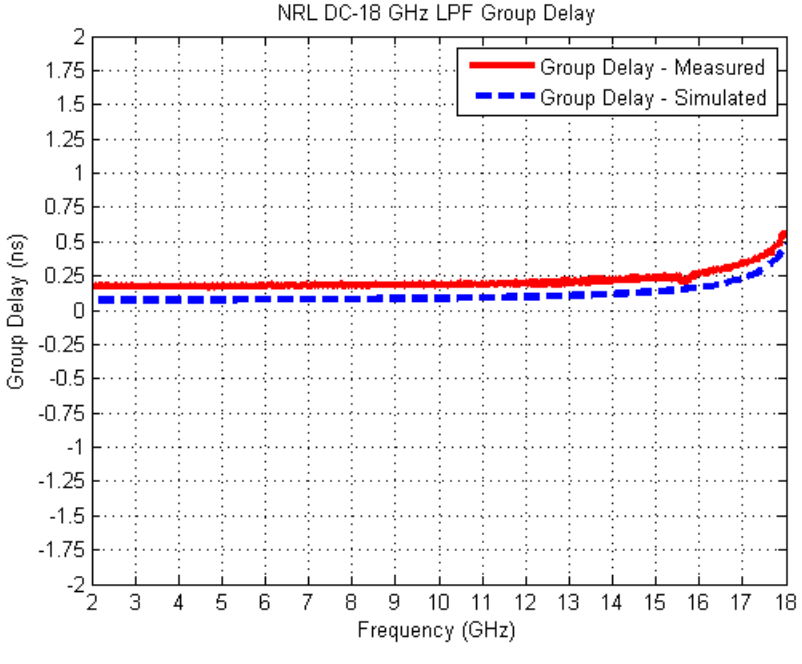

Figure 4-11: LPF Group Delay Comparison

Figure 4-11 is a comparison between the measured and simulated group delay. The difference between the two is due to the additional length of connector not simulated in HFSS.

4.1.3 High Pass Filter

In this section, the generalized Chebyshev lumped element lowpass prototype will be transformed into a distributed high pass prototype. A very similar design approach as above can be done to derive the distributed parameter equations. From a circuits standpoint, a frequency transformation

$$\omega \rightarrow -\frac{\omega}{\omega_c} \tag{4.27}$$

occurs. The physical meaning of this is that inductors are transformed into capacitors and capacitors are transformed into conductors. The generalized lowpass filter can also be transformed to a distributed high pass filter by directly applying the Richards transformation [20]

$$s = \frac{\omega_o}{jtan(a\omega)} \tag{4.28}$$

where s is the complex frequency and a is again a constant. This Richards transformation allows for modeling of lumped inductors as short circuit stubs and capacitors as open circuit stubs [19].

Applying the Richards transformation in 4.28 to equation 4.2, the length of the stubs can be derived as

$$l_2 = \frac{v}{\pi f_c} tan^{-1}(\omega_o) \tag{4.29}$$

and the width can be solved using equation 4.22 and supporting Getsinger curves.

The series capacitors are traditionally implemented using coupled line structures. However, when large passband bandwidths are desired, the impedances necessary become too small to be realized. This is commonly a milling limitation due to the impeccably small coupled line separation. This issue can be overcome by implementing a broadside coupled line structure for the

series capacitors. By choosing a super thin substrate, tiny impedance vales can be met for UWB applications.

Using the same width for the series stubs that was found 4.12 when setting Z_o to 50 Ω, the effective dielectric of the HPF can be solved using

$$\varepsilon_e = \frac{1}{2}[\varepsilon_r + 1 + (\varepsilon_r - 1)F] \tag{4.30}$$

where

$$F = (1 + 12h/w)^{-1/2} \tag{4.31}$$

Once this effective dielectric is known, the length of the broadside coupled section can be calculated. In [19], the length equation of the broadside coupled line is

$$l_3 = \frac{(1.8vZ_{oo}C_s(R))}{\sqrt{\varepsilon_e}} \tag{4.32}$$

where $C_s(R)$ is the capacitance calculated after frequency transformation and impedance scaling.

$$C_s(R) = \frac{1}{2\pi f_c L_o(R) R_s} \tag{4.33}$$

The odd mode characteristic impedance is numerically analyzed for a certain substrate as [22]

$$Z_{oo} = \frac{Z_{oo}^o}{\sqrt{\varepsilon_{oo}}} \tag{4.34}$$

where

$$\frac{1}{\sqrt{\varepsilon_{oo}}} = 1 + 0.5\left[H - P * ln\left(\frac{w}{b} + \sqrt{\left(\frac{w}{b}\right)^2 + 1}\right)\right]\left[ln\left(\frac{1}{\sqrt{\varepsilon_r}}\right) + \frac{1}{\sqrt{\varepsilon_r}} - 1\right] \tag{4.35}$$

and

$$H = 0.7210 - 0.3568\left(\frac{h}{b}\right) + 0.02132\left(\frac{a}{b}\right) \tag{4.36}$$

$$P = -0.3035 + 0.3743\left(\frac{h}{b}\right) + 0.07274\left(\frac{a}{b}\right) \tag{4.37}$$

I set a = b = 70 mil and used a 5 mil thick Rogers 6002 RT/Duroid substrate (with a dielectric constant $\varepsilon_r = 2.94$ and a loss tangent$\delta = .0012$. Finally, it is shown that

$$Z_{oo}^{o} = \frac{\eta_o}{2}\left[S + T * ln\left(\frac{.2}{w/b} + \sqrt{1 + \frac{.23}{(w/b)^2}}\right)\right] \tag{4.38}$$

where

$$S = -0.1073 + 1.67080\left(\frac{h}{b}\right) + 0.007484\left(\frac{a}{b}\right) \tag{4.39}$$

$$T = 0.4768 + 2.1295\left(\frac{h}{b}\right) - 0.01278\left(\frac{a}{b}\right) \tag{4.40}$$

After the lengths and widths have been calculated, the system was built up in ADS using the same stripline model approach and modifying it for SSS simulations. Because the high pass filter performs like a bandpass filter over a large bandwidth, the distributed variables had to be tuned appropriately for the required 2-18 GHz pass band. After initial tuning, a quick optimization was done and the ADS schematic and results are shown below in figure 4-12 and 4-13. The design was then built up in HFSS and optimized using finite element full electromagnetic simulation. The HFSS results are shown in figure 4-14 and 4-15.

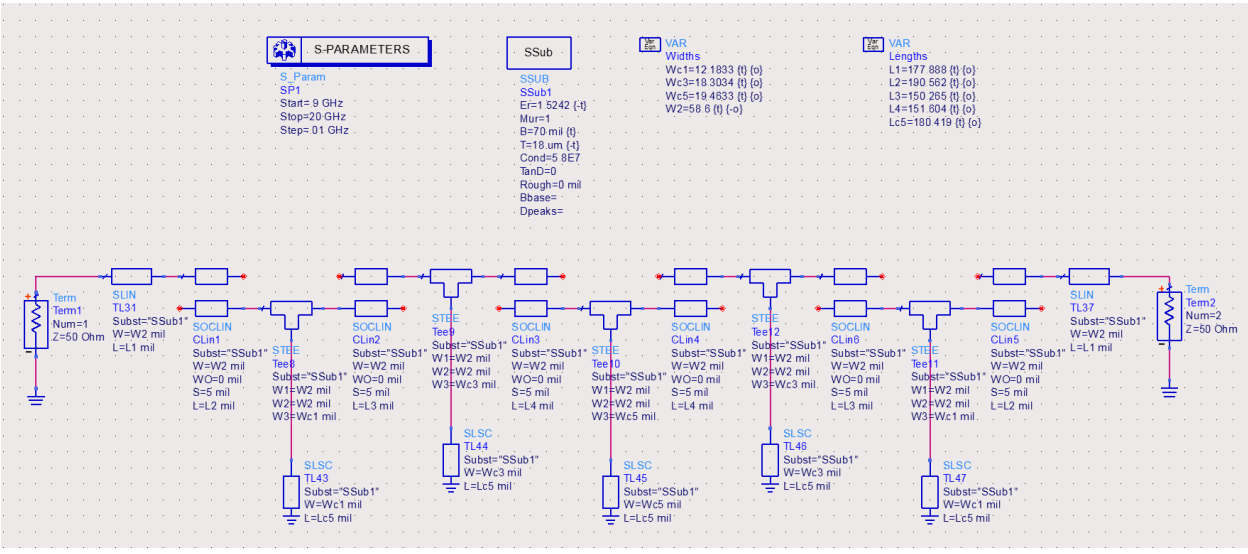

Figure 4-12: ADS Schematic with Tuned Values

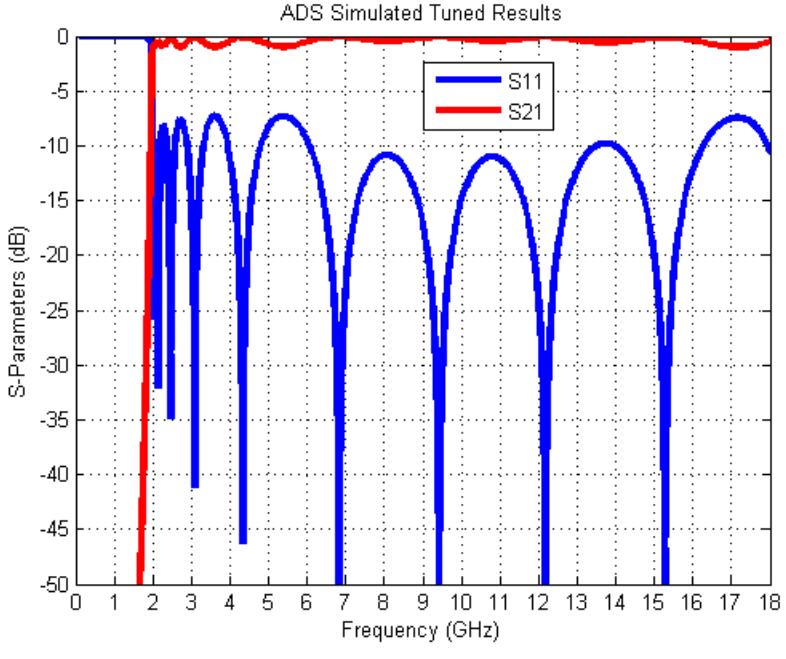

Figure 4-13: ADS Simulated Results with Tuned Values

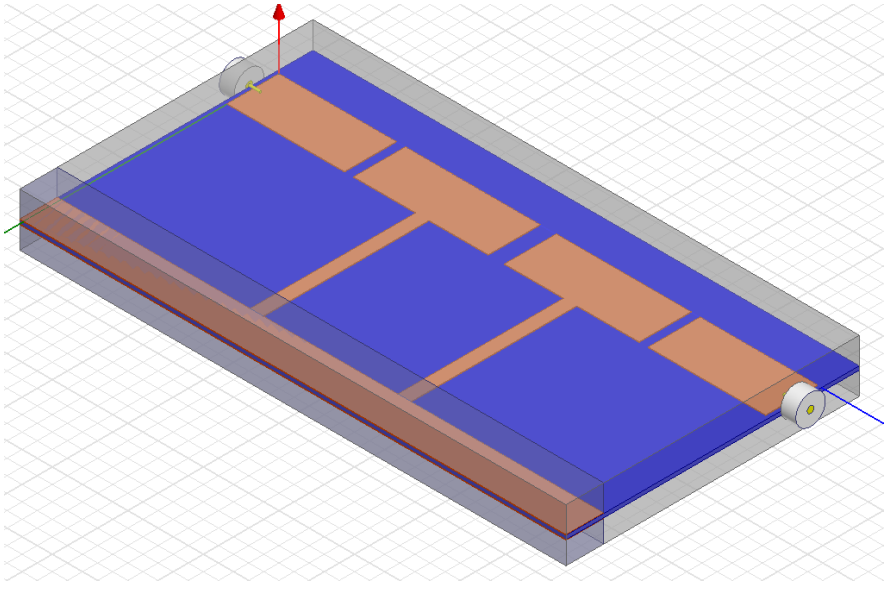

Figure 4-14: HFSS Simulated Results with Tuned Values

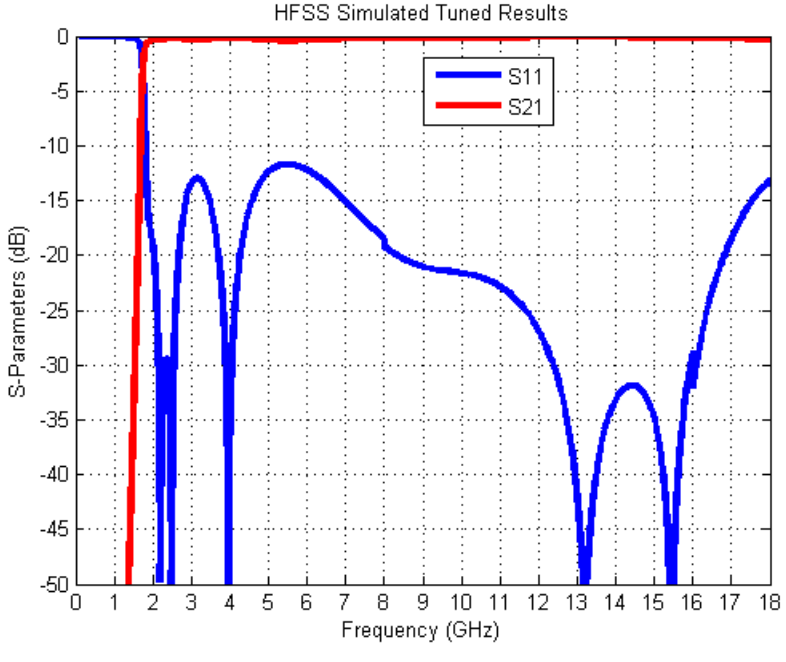

Figure 4-15: HFSS Simulated Results with Tuned Values

As with the LPF in 4.1.2, special attention is needed when laying out the design in HFSS. The inside of the SSS filter is equivalent to a rectangular waveguide which forms notches in the passband if the cutoff frequency is not above the desired passband. The HPF is also inherently longer than the LPF due to the broadside coupled sections. Because of this, it is typical to increase

the width of the coupled section and decrease the length while maintaining the capacitance value. This will shorten the length of the filter and allow for wider bandwidth filters.

Figure 4-16 is a photo of the finished product as well as the filter. Both are compared to a quarter for size reference. Figure 4-17 is a comparison between the measured and HFSS simulated results. The insertion loss is less than 1 dB across the pass band, and the return loss is greater than 10 dB across the passband. The attenuation in the stopband is greater than 60 dB below 1 GHz. Figure 4-18 is a comparison between the in-house and purchased LPF. Again, the difference in S_{11} between the measured and simulated results is due to the same issues discussed for the LPF. A 10× cost reduction is accomplished by developing the filters in-house. These filters can be made in 2 days eliminating the 8 week lead time for purchased filters.

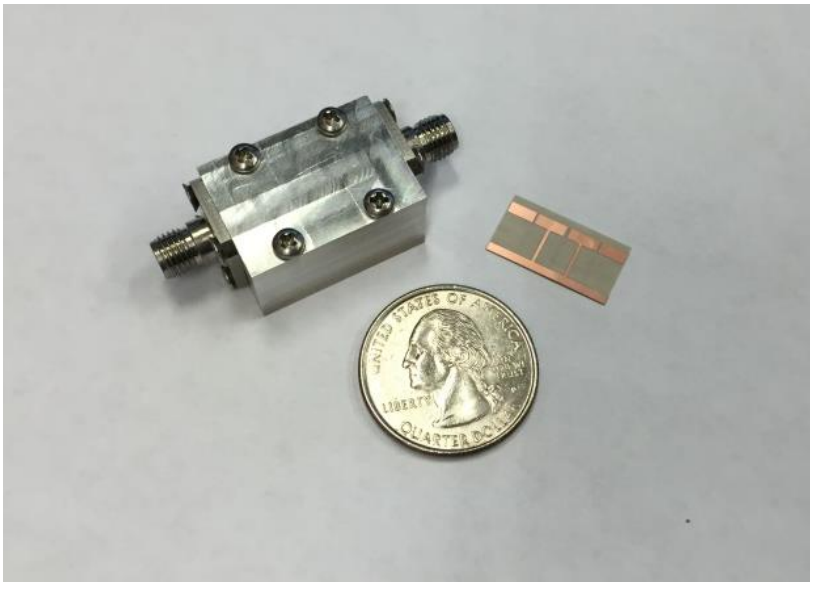

Figure 4-16: HPF Finished Product

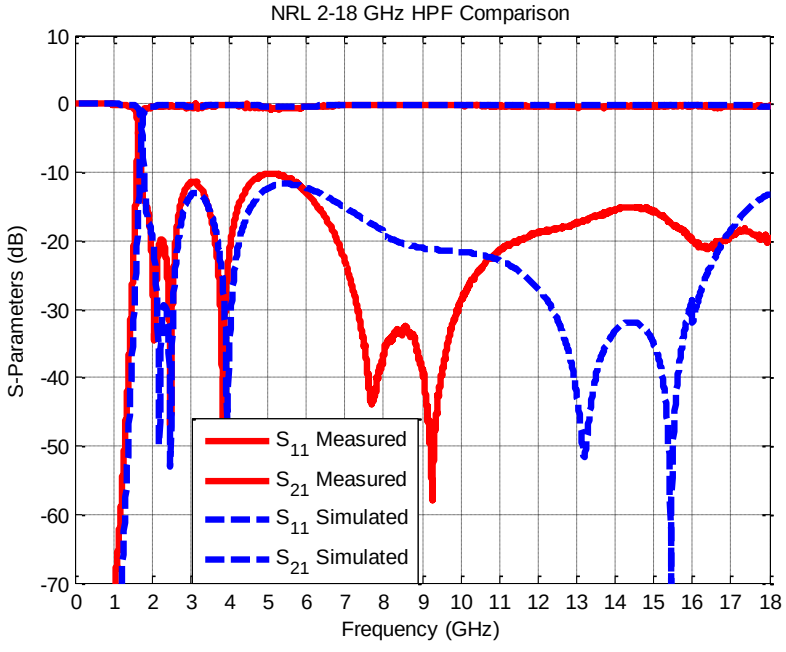

Figure 4-17: 2-18 GHz Measured vs Simulated Comparison

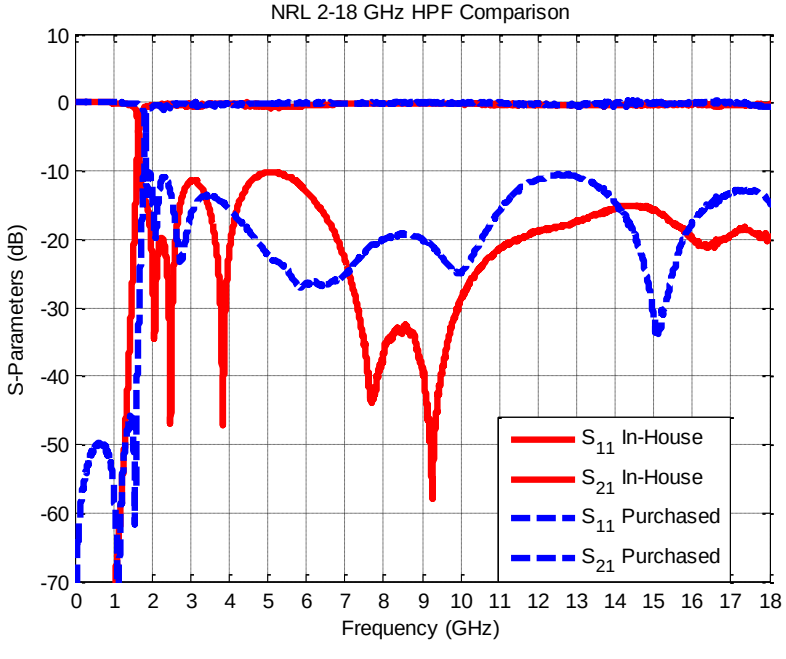

Figure 4-18: In-house Filters vs Purchased Filters Comparison

Figure 4-19 is a comparison between the measured and simulated group delay. The difference between the two is due to the additional length of connector not simulated in HFSS.

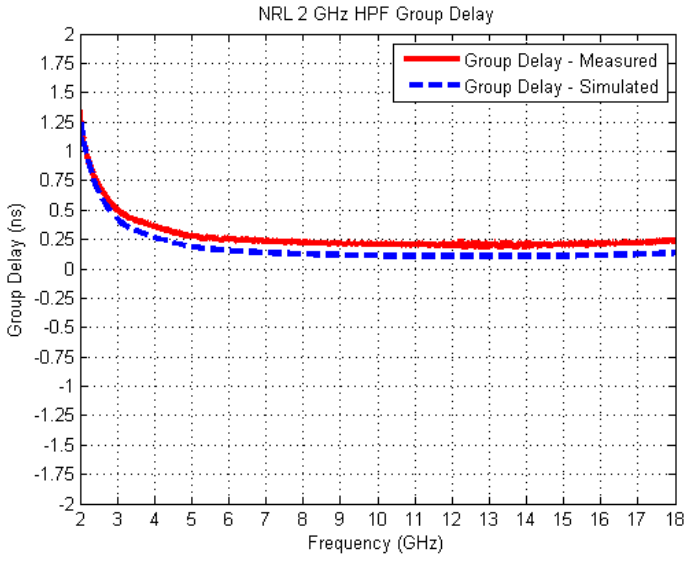

Figure 4-19: HPF Group Delay Comparison

4.1.4 Band Pass Filter

After both filters were tested individually, the filters were cascaded to perform as a bandpass filter. Figure 4-19 is a comparison between the in-house filters cascaded and the purchased filters cascaded. The in-house filters have an insertion loss less than 2 dB across the pass band and a return loss greater than 10 dB across the pass band.

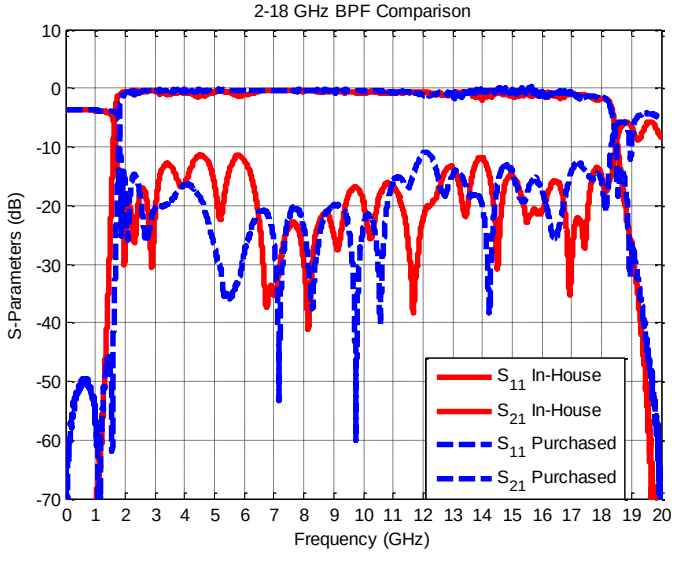

Figure 4-20: In-house Filters vs Purchased Filters Comparison

4.2 POWER COMBINER

The current receive Vivaldi antenna array is designed to have 8×8 active elements totaling 64 single elements. Because of the limited data storage, rack space, and cost of digitizing all the data from these 64 elements, they are first power combined in the along-track using 16 power combiners to produce 8 V-polarized outputs and 8 H-polarized outputs in the cross-track, which would still maintain the cross-track beam-steering capability. Therefore, a total of 16 power combiners are necessary to accomplish this task.

For the March 2015 NRL deployment, 8:1 power combiners from Pulsar microwave and several high frequency cables from Fairview Microwave were purchased. This approach was incredibly expensive and had several mechanical issues. The shelf structure that was designed at CReSIS was exceptionally heavy after the power combiners were added. Also, the bulk cabling between the antenna and power combiner shelf was sufficiently long and required a lot of mechanical stress relieving to avoid damaging the connectors on the array. Given these issues, a new approach of integrating lightweight power combiners into the array for future deployments has been designed.

In this section, a novel design approach will be shown for a TEM-mode Hybrid Power Combiner. Design parameters will be referenced and provided below.

4.2.1 Power Combiner Design Parameters

In microwave transmission line theory, it is common to use the multi-section technique to increase bandwidth by using multiple sections of increasing or decreasing characteristic impedance for matching. For this design, this multi-section approach was applied to the Wilkinson's N-way power combiner. The theory and design parameters for this concept were originally derived by Cohn following the design of the Wilkinson divider [14]. Since then, several other papers including

[15-17] have proposed other techniques to accomplish UWB designs but either require complex geometries which increase fabrication cost or require lengthy tapered lines requiring a large footprint for just a 2:1 divider/combiner. Using design in [14], cascaded annular rings of λ/4 can be cascaded to shorten length and provide ease of fabrication. Also, because of the reduced length, multiple 2:1 sections can be cascaded to expand design to a 4:1, 8:1, and 16:1 divider/combiner with a simple 50 ohm line connecting the two sections while maintaining minimum length.

The general circuit for the multi-section three-port hybrid can been seen below in figure 4-21. In his paper, Cohn provides design parameters up to an N=7 multi-section hybrid. The values Z_n and Rn are given for the normalized case of Z_o=1 and should be multiplied by Z_o of the design. Another parameter that should be noted is f_2/f_1. Maximum frequency divided b minimum frequency will determine how many sections are needed for the specified bandwidth. For this design, f_2=18 GHz and f_1=2 GHz resulting in f_2/f_1=9. Therefore, from Table 1 in [14], an N=7 hybrid should be used for the desired bandwidth.

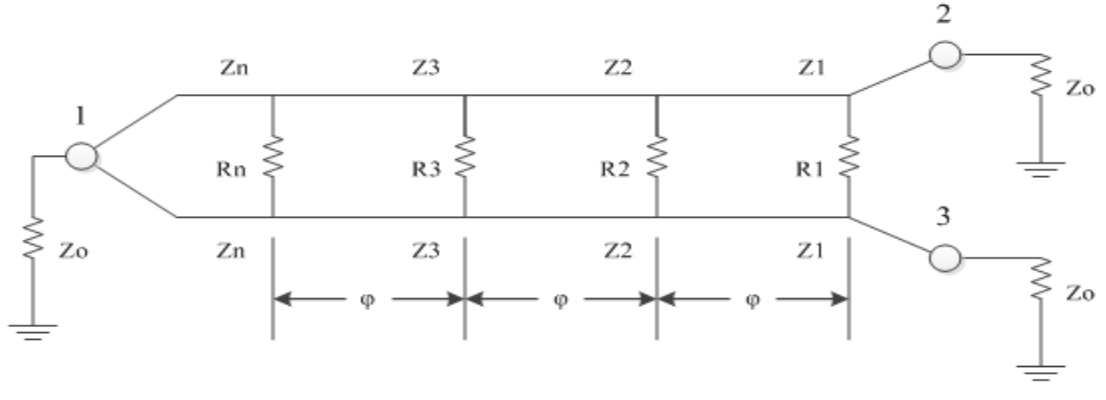

Figure 4-21: Generalized Circuit for a Multi-section Three-port Hybrid

In table 4-1 below, the design parameters for the 2-18 GHz 2:1 power combiner are presented. The Z_n and R_n provided have been multiplied by Z_o=50 and the corresponding lengths

and widths have been calculated for each section. It should be noted that each section is λ/4 at the "average" center frequency of the bandwidth (10 GHz) and was implemented on Rogers 5880 material consisting of a dielectric constant (ε_r) of 2.20 and a loss tangent of .0009.

TABLE 4-3
TEM-MODE THREE-PORT HYBRID DESIGN PARAMETERS

	Z_n (Ω)	R_n (Ω)	W_n (mil)	L_n (mil)
N = 1	56.37	442.48	50.51	215.82
N = 2	60.25	616.15	45.33	216.57
N = 3	65.09	446.23	39.81	217.46
N = 4	70.71	319.9	34.41	218.43
N = 5	76.82	217.58	29.52	219.42
N = 6	82.99	129.62	25.39	220.36
N = 7	88.70	248.26	22.14	221.17

Due to the relatively small structure of this design, 0402 resistors were used between the junction points. Therefore, careful design considerations need to be made to make sure the resistors length is long enough to cross the gap of the junction point for each section. It should also be obvious that following the final tuning of the design, actual resistor values should be chosen close to the optimized resistance values and a final simulation ran to verify performance. Finally, adequate separation of the output terminals should be verified so that a connector can be soldered onto the device for assembly and testing. The remainder of this chapter will provide ADS and HFSS schematics and simulated results.

Using the values in Table 4-1, the generalized circuit in figure 4-21 was built in ADS and simulated using these theory values. The ADS schematic is shown in Figure 4-22 followed by the simulated results in figure 4-23. After proof of concept in ADS, the structure was designed in

HFSS and a full finite-element full-wave electromagnetic simulation was run. The HFSS structure is shown in figure 4-24 and simulated results are shown in figure 4-25.

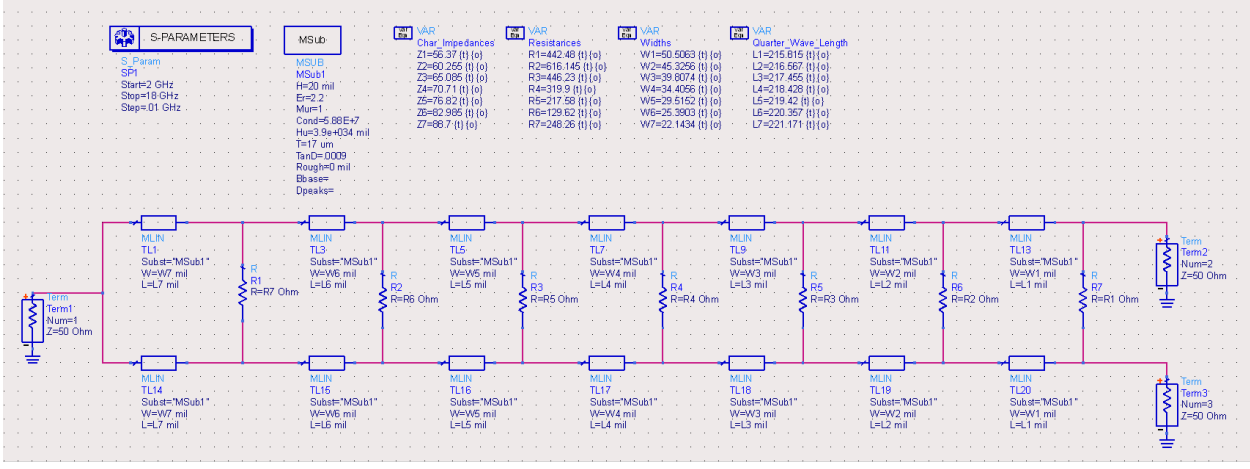

Figure 4-22: ADS Schematic of 2:1 Power Combiner

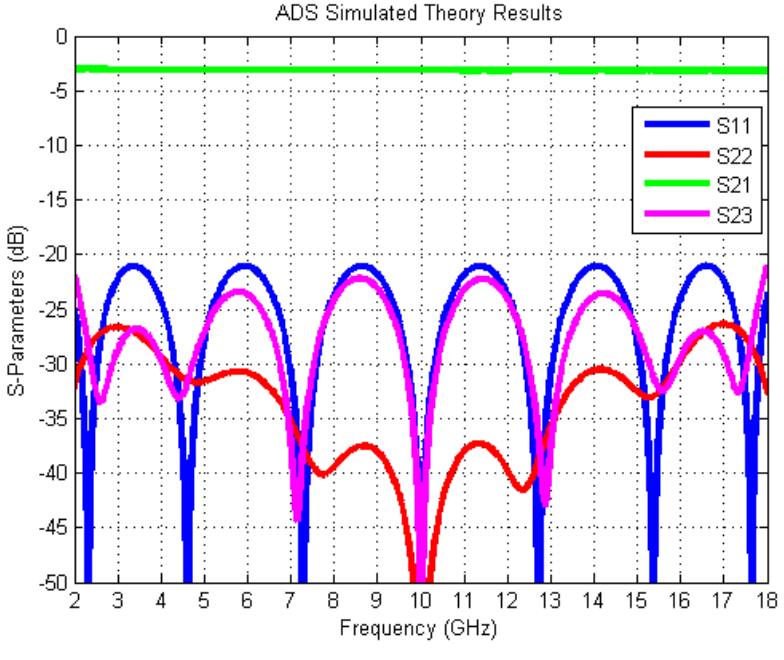

Figure 4-23: ADS Simulated Results of 2:1 Power Combiner

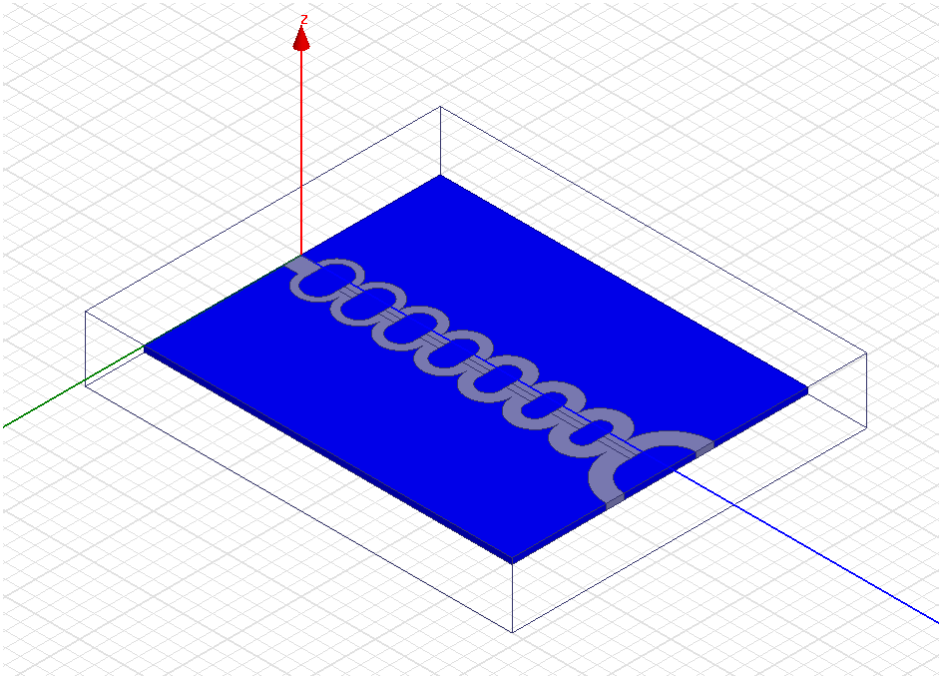

Figure 4-24: HFSS Structure of 2:1 Power Combiner

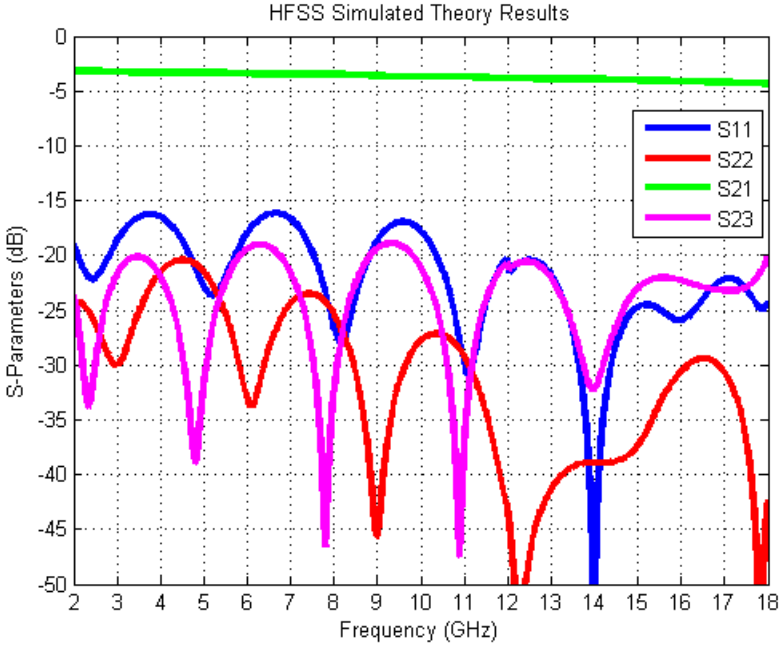

Figure 4-25: HFSS Simulated Results of 2:1 Power Combiner

After initial results were achieved for the 2:1 power combiner, the 2:1 was cascaded to create the 8:1 power combiner. The structure was again built up in HFSS and a full electromagnetic

(EM) simulation was run. These initial simulations were not as great as for the 2:1 so some minor changes were made to the design. For the 8:1 combiner, an additional section was added to increase the bandwidth even further allowing for the insertion loss from 16 GHz to 18 GHz to be significantly improved. The trace widths, lengths, and resistance values were optimized to achieve optimal performance. Finally, the connecting lines were curved to shorten the length of the overall combiner to achieve minimal size. The 8:1 ADS schematic is the same as above but cascaded three times. However, the simulated results are shown in figure 4-26 as well as the HFSS structure in figure 4-27 along with its simulated results in figure 4-28.

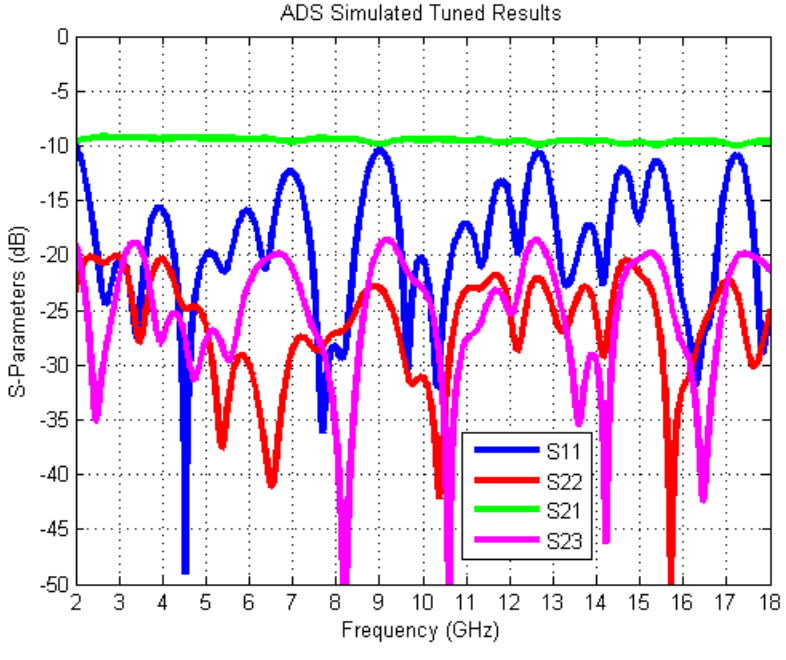

Figure 4-26: ADS Simulated Results of 8:1 Power Combiner

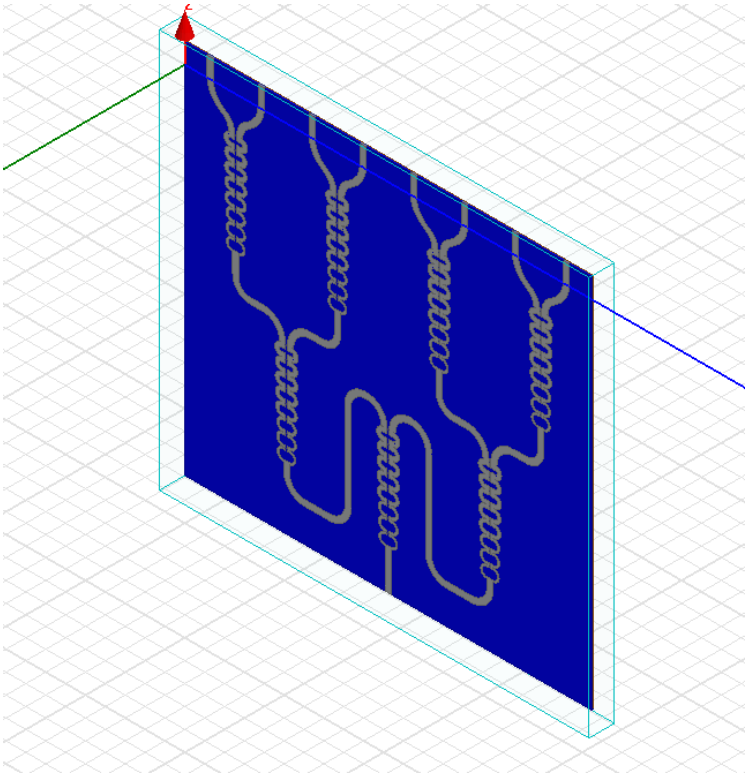

Figure 4-27: HFSS Structure of 8:1 Power Combiner

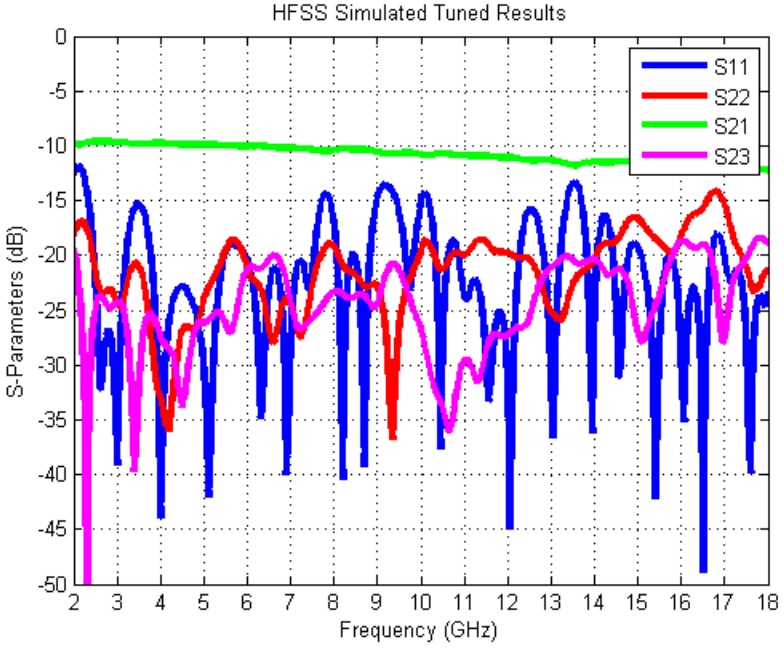

Figure 4-28: HFSS Simulated Results of 8:1 Power Combiner

5 MEASUREMENTS AND RESULTS

In this chapter, the laboratory measurements setup will be discussed and measured results of the individual receiver will be provided. Minor modifications that were done to the receiver to satisfy the March 2015 deployment will also be discussed. Data results and echograms from Barrow Alaska will be provided and discussed in further detail.

5.1 RECEIVER MEASUREMENTS

To verify receiver performance after integration into their individual cases, the individual receivers were tested in the RF lab at CReSIS. The measurements were made using a vector network analyzer set up in mixer mode. The RF and LO ports were swept from 1-20 GHz with the IF frequency set to 40 MHz. The IF bandwidth was set to 5 kHz, and receivers were measured using 32,001 points. The cables used during the experiment were measured separately to determine cable loss. This loss was subtracted from the receiver measurement in MATLAB. This was repeated 12 times in order to make sure each receiver was performing correctly. A measured result of one of the receivers is provided in figure 5-1.

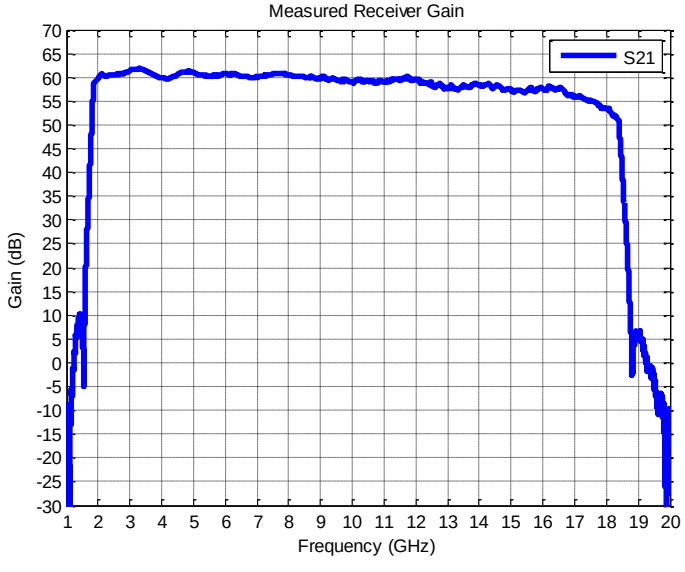

Figure 5-1: Measured Receiver Gain

5.2 RECEIVER MODIFICATIONS FOR NRL SPRING MISSION

In order to meet the March 2015 deployment, a few minor modifications had to be made to the receiver. Because a single chirp operation was used, due to unforeseen complications, the receiver IF section of the filter had to be slightly re-configured. Since the Twin Otter flies at approximately1400 ft., this put the beat frequency within the 4^{th} Nyquist zone (187.5-250 MHz). In order to pass this signal through the IF section, the first filter was changed to a RBP-190+ surface mount filter with a passband from 190-250 MHz. Also, the final 62.5 MHz elliptic lowpass filter was bypassed with a piece of coax. With these modifications, the return signal could be detected during nominal flight height with sufficient attenuation of out-of-band signals.

The RF chain used Hittite evaluation boards instead of the integrated RF amplifier boards due to duplication errors in the fabrication and assembly process of the boards. The changes needed to integrate these boards in the future will be discussed in chapter 6. Once all of these modifications were made, the individual receivers were re-tested with the VNA in mixer mode to verify performance. Because the integrated amplifier board made in house had almost exact performance of the evaluation boards, the overall performance of the receiver was exactly the same. However, while in mixer mode, the receiver was measured with a beat frequency set to 190 MHz, 220 MHz, and 250 MHz to make sure the receiver performed the same across the entire Nyquist zone. The variance across the Nyquist passband was less than 1 dB.

5.3 BARROW ALASKA DATA AND ECHOGRAMS

In figure 5-2, frequency domain data from Barrow, AK when flying over thin ice on a lead is shown. The beat frequency is just above 200 MHz which corresponds to approx. 1400 ft. altitude. Right above 200 MHz, there is a sharp increase in the signal return followed by a long trailing edge. This is caused due to multiple scattering targets, or in this case, multiple chunks of ice. Figure

5-3, is a picture taken from the Twin Otter aircraft giving a general idea of the landscape in the area. This roughness is also captured in the echograms discussed below.

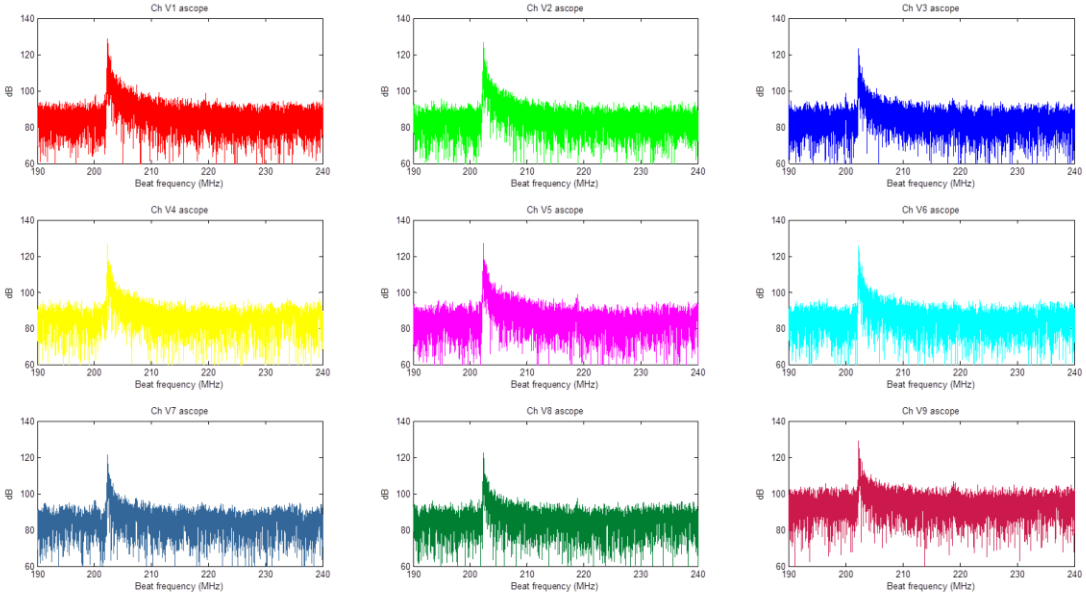

Figure 5-2: Frequency Domain Plots of Measured Data in Barrow, AK

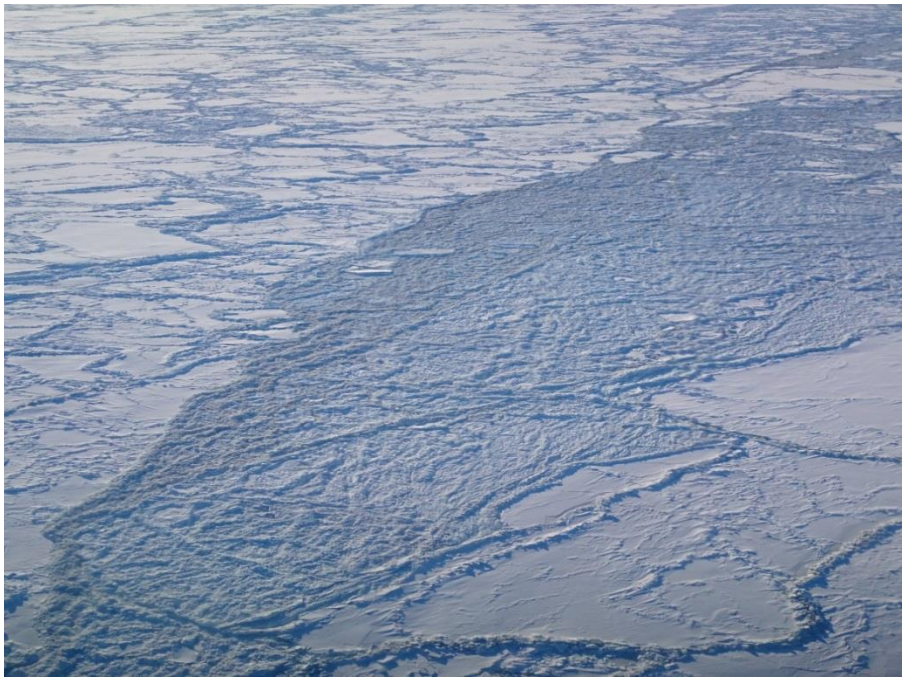

Figure 5-3: Photo from Twin Otter Aircraft (courtesy of: Dr. Stephen Yan)

During the filed mission in Barrow Alaska, we were able to do some basic field-processing to verify the system is working. Echograms are the generated data products that allow us to determine the snow thickness. The first figure below is the echogram after field-processing. After arriving back at CReSIS, the data was reprocessed with a more sophisticated program implementing coherent phase noise removal and de-convolution with the system response. This code was developed by Dr. Jie Bang (Stephen) Yan; Principle Investigator (PI) on the NRL project. This echogram is shown below as well.

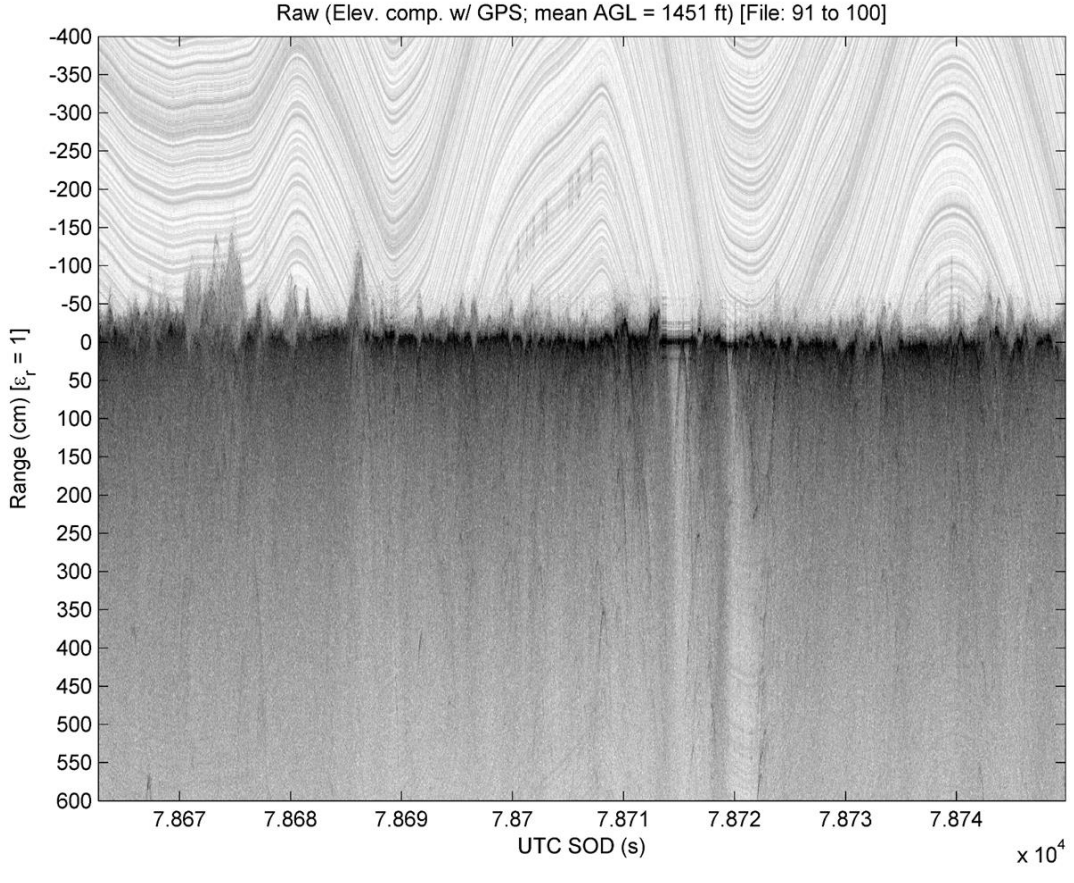

Figure 5-4: Field-Process Echogram from Barrow Alaska (March 2015)

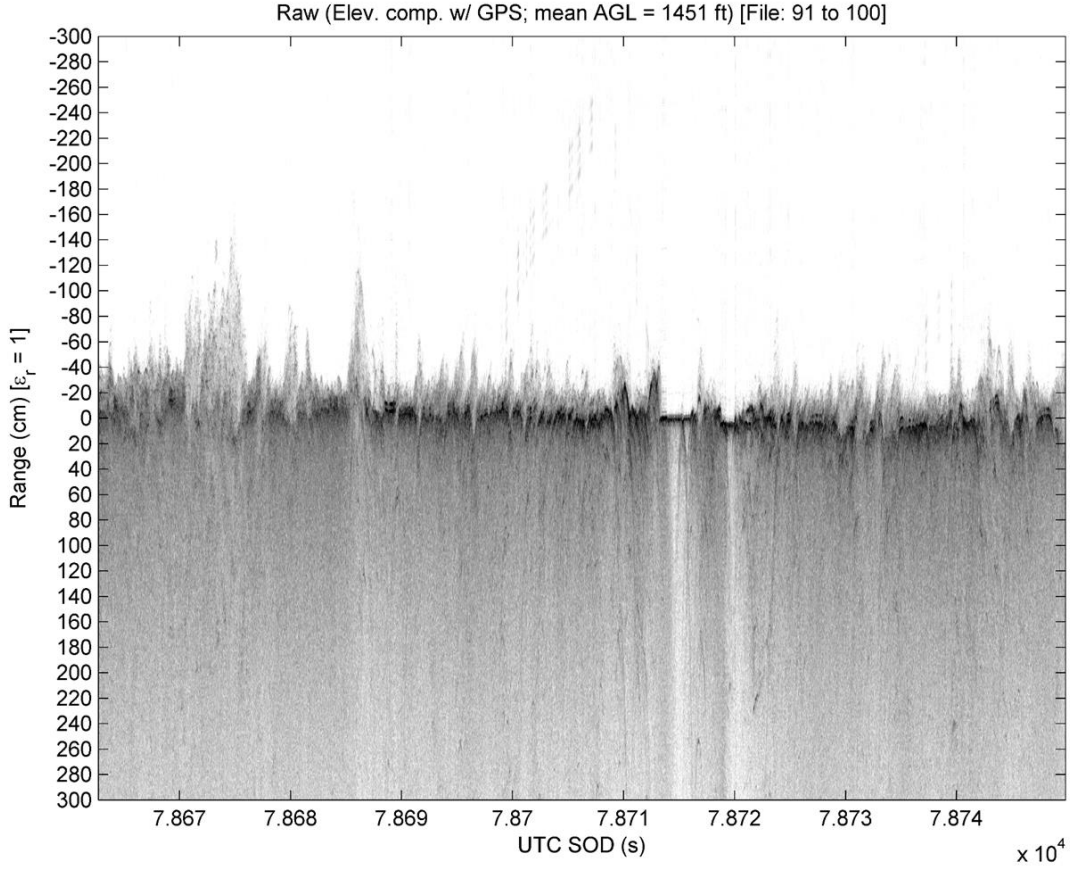

Figure 5-5: Data with Coherent Phase Noise Removal and De-Convolution from Barrow, AK (March 2015)

The echogram after de-convolution and coherent noise removal provides a very clear definition of where the snow-air and snow-ice interfaces are. However, both echograms clearly indicate how rough the landscape was which is supported from the frequency domain response and pictures taken from aircraft. During the test flight, a ground team from the NRL crew took measurements of the snow thickness from sites where data was recorded. Initial measured results matched very well with snow thickness captured by the radar. Development of additional radar signal processing will continue at CReSIS in order to implement snow water equivalent estimation, and from this snow density using the snow depth measurements.

6 CONCLUSIONS AND FUTURE WORK

At the Center for Remote Sensing of Ice Sheets, UWB FMCW radars have been developed and deployed to accurately determine snow thickness. With increased demand for additional snow characterization to more accurately model sea level rise, a new multi-channel, quad-polarized, 2-18 GHz Snow radar has been developed. The major contributions of this thesis were the design, integration, and miniaturization of a 2-18 GHz receiver as well as the design and integration of a 2-18 GHz transmitter. The theory to measurement process of UWB SSS filters and theory to simulation process of a TEM-Mode Hybrid power combiner were another major contribution. These passive microwave components can be used for future builds and expansion to reduce cost and eliminate major lead times. In March 2015, the Snow radar was deployed to Barrow, AK to satisfy the NRL mission. After processing the raw data, results were compared against lab loop-back measurements as well as calculated link budget results. Both the loop-back and measured results from Barrow matched very well but showed a decent reduction in SNR from calculated link budget results. This SNR reduction is due to coherent noise in the system raising the noise floor. This issue is generated in the frequency multiplier, which has been fixed. Snow thickness was successfully determined and accuracy was verified with NRL ground crews. Additional processing will need to be done for the side-looking channels to determine SWE and ultimately snow density.

For future miniaturization of the receiver, the receiver RF amplifier chain presented in figure 2-7 will need to be integrated into the receiver. This can be done by having the RF amplifier boards professionally fabricated and assembled. The boards must be gold-plated on each side and solder mask should be removed along the RF trace. Instead of using the Henkel conductive film to bond the board to the heatsink, as used for the in-house prototype, Sn96 should be used instead. This conductive material is used by Hittite for their evaluation boards. Professional assembly will be required due to the assembly limitations in the CReSIS labs. Sn96 requires additional venting

as well as specialized reflow cycles. This conductive material can bond to bare aluminum, minimizing cost of material and overall weight.

Additional future work for the receiver RF chain includes new options in surface mount mixers. Marki Microwave and Miteq offer several surface mount mixer options but typically show weaker performance than their connectorized counterparts. If initial testing of mixers is successful, these components can be integrated onto the RF amplifier chain.

The distributed lowpass filter prototype equations were derived from the generalized Chebychev lowpass filter prototype by applying basic circuit analysis and using the Richards transformation. An equivalent SSS ADS model was developed and verified with finite-element simulations from HFSS. This model allows for significant time reduction during the tuning/optimization stage of the filter design. A lowpass filter with an 18 GHz cutoff frequency was designed, assembled, and measured in-house to verify filter performance. A quick discussion on how the lowpass filter prototype can be transformed to a distributive highpass prototype by modifying the Richards transformation to be applied. The introduction of broad-side coupled striplines could overcome fabrication limitations when dealing with UWB applications. A highpass filter with a 2GHz cutoff frequency was also designed, assembled, and measured at CReSIS to verify filter performance.

Finally, a 2-18 GHz 8:1 power combiner was designed and simulated and results were shown in section 4.2. Modifications to the design must be made to integrate the power combiner into the Vivaldi array and simulations must be run to verify performance. After simulating the design, fabrication and testing of the power combiner should be done and tested with the array.

7 REFERENCES

[1] M. I. Skolnik, *Introduction to RADAR Systems,* Third Edtion, McGraw-Hill Book Co., 2002

[2] Alvetegui, D., *A Linearization Method for a UWB VCO-Based Chirp Generator Using Dual Compensation,* Department of Electrical Engineering and Computer Science: Master's Thesis, University of Kansas, 2011

[3] Morales F., Gogineni S., Leuschen C., *Advanced Multifrequency Radar Instrumentation for Polar Research,* IEEE Transactions on Geoscience and Remote Sensing Vol. 52 No. 5, pp 2824-2842, May, 2014.

[4] R. Flickenger, *Wireless Networking in the Developing World,* Third Edition, CreateSpace Independent Publishing Platform, 2013

[5] Spreen, G., L. Kaleschke, and G. Heygster. *Sea Ice Remote Sensing Using AMSR-E 89GHz Channels*. JOURNAL OF GEOPHYSICAL RESEARCH. Web. 8 Dec. 2014. <http://www.iup.uni-bremen.de/iuppage/psa/documents/spreen07.pdf>.

[6] M. Richards, J. Scheer, W. Holm, *Principles of Modern Radar,* SciTech Publishing, 2010

[7] F. Ulaby, D. Long, *Microwave Radar and Radiometric Remote Sensing,* Michigan Press, 2014

[8] C. Balanis, *Antenna Theory,* Third Edition, Wiley-Interscience, 2005

[9] X. Xu, L. Tsang, S. Yueh, *Electromagnetic Models of Co/Cross Polarization of Bicontinuous/DMRT in Radar Remote Sensing of Terrestrial Snow at X- and Ku-band for CoReH20 and SCLP Application,* IEEE Journal of Selected Topics in Applied Earth Observations and Remote Sensing Vol. 5 No. 3, pp 1024-1032, 2012

[10] S. Yueh, *Airborne Ku-band Polarimetric Radar Remote Sensing of Terrestrial Snow Cover*, IEEE Transactions on Geoscience and Remote Sensing Vol. 47 No. 10, pp 3347-3364, 2009

[11] Natural Resources Conservation Service. (n.d.). Retrieved March 2, 2015, from http://www.nrcs.usda.gov/wps/portal/nrcs/detail/or/snow/?cid=nrcs142p2_046155

[12] S. Beaven, *Sea Ice Radar Backscatter, Measurements, and the Fusion of Active and Passive Microwave Data.* PhD Dissertation, University of Kansas, 1995

[13] T. Jonas, C. Marty, J. Magnusson, *Estimating the snow water equivalent from snow depth measurements in the Swiss Alps*, Journal of Hydrology Vol. 378, pp 161-167, 2009

[14] S. Cohn, *A Class of Broadband Three-Port TEM-Mode Hybrids*, IEEE Transactions on Microwave Theory and Techniques VOL. 16 No. 2, pp 110-116, 1968

[15] C.T. Chiang, B.K. Chung, *ULTRA WIDEBAND POWER DIVIDER USING TAPERED LINE*, Progress in Electromagnetic Research Vol. 106, pp 61-73, 2010

[16] P.O. Afanasiev, V.A. Sledkov, M.B. Maniulov, *A Novel Design of Ultra-Wideband Stripl-Line Power Divider for 2-18 GHz*, International Conference on Antenna Theory and Techniques, pp 323-325, 2013

[17] K. Shamaileh, *Fourier-Based Transmission Line Ultra-Wideband Wilkinson Power Divider for EARS Applications*, Midwest Symposium on Circuits and Systems, 2013

[18] S. Alseyab, *A Novel Class of Generalized Chebyshev Low-Pass Prototype for Suspended Substrate Stripline Filters*, IEEE Transactions on Microwave Theory and Techniques Vol. 30, No. 9, pp 1341-1347, 1982

[19] Z. Zakaria, *Generalized Chebyshev Highpass Filter based on Suspended Stripline Structure for Wideband Applications,* Jurnal Teknologi, 2014

[20] N. Lioutas, *Design of a Generalized Chebyshev Suspended Substrate Stripline Filters,* Defence Research Centre Salisbury, 1986

[21] D. Pozar, *Microwave Engineering,* Fourth Edition, John Wiley and Sons Inc., 2012

[22] Y. Shu, X. Qi, Y. Wang, *Analysis Equations for Shielded Suspended Substrate Microstrip Line and Broadside-Coupled Stripline,* Radio Engineering Dept. of Nanjing Institute of Technology

[23] W. Getsinger, *Coupled Rectangular Bars Between Parallel Plates,* IEEE Transactions on Microwave Theory and Techniques, pp 65-72, 1962

[24] R. Ludwig, *RF Circuit Design: Theory and Applications,* Second Edition, Pearson Education, 2009

[25] C. Allen, *Radar Measurments II* [PowerPoint Slides]. Retrieved from http://people.eecs.ku.edu/~callen/725/EECS725.htm

[26] J. Stiles, *Noise in Microwave Systems* [PDF Format]. Retrieved from http://www.ittc.ku.edu/~jstiles/622/handouts/section_4C_Noise_in_Microwave_Systems.pdf

[27] R. Kwok, G.F. Cunningham, *ICESat over Artic sea ice: Estimation of snow depth and ice thickness,* Journal of Geophysical Research Vol. 113, C08010, 2008

[28] Mini-Circuits, *DC-18 GHz Precision Fixed Attenuator* [PDF Format]. Retrieved from http://www.minicircuits.com/pdfs/BW-S1W2+.pdf, Mini-Circuits, New York

[29] Hittite Microwave, *GaAs pHEMT MMIC Low Noise AGC Amplifier, 2-20 GHz* [PDF Format]. Retrieved from http://www.hittite.com/content/documents/data_sheet/hmc463lh250.pdf, Hittite Microwave Corp., Massachusetts

[30] AMTI, http://www.diplexers.com/products/highpass/1000mhz-2499mhz/h02g18g6.html, AMTI, Virginia

[31] AMTI, http://www.diplexers.com/products/lowpass/18000mhz-23999mhz/l18g20g1.html, AMTI, Virginia

[32] Miteq, *2-18 GHz Double Balanced Mixer* [PDF Format]. Retrieved from https://www.miteq.com/docs/MITEQ-DB0218.PDF, Miteq, New York

[33] Mini-Circuits, *DC-7 GHz Fixed Attenuator* [PDF Format]. Retrieved from http://www.minicircuits.com/pdfs/PAT-1+.pdf, Mini-Circuits, New York

[34] Mini-Circuits, *DC-70 MHz Metal Shield Low Pass Filter* [PDF Format]. Retrieved from http://www.minicircuits.com/pdfs/RLP-70+.pdf, Mini-Circuits, New York

[35] Hittite Microwave, *InGaP HBT Gain Block MMIC Amplifier, DC-1 GHz* [PDF Format]. Retrieved from https://www.hittite.com/content/documents/data_sheet/hmc580st89.pdf, Hittite Microwave Corp., Massachusetts

[36] Acopian, http://www.acopian.com/store/productdetail.aspx?q=i276, Acopian, Pennsylvania

[37] Mini-Circuits, *700 MHz-18 GHz Super Ultra Wideband Amplifier [*PDF Format]. Retrieved from http://www.minicircuits.com/pdfs/ZVA-183+.pdf, Mini-Circuits, New York

[38] Pasternack, *50 ohm 4 Way SMA Power Divider from 2-18 GHz at 10 Watts* [PDF Format]. Retrieved from http://www.pasternack.com/images/ProductPDF/PE2029.pdf, Pasternack, California

[39] Daitron, http://www.daitronpower.com/hfs30.html, Daitron, Tokyo, Japan

[40] Hittite Microwave, *GaAs pHEMT MMIC Low Noise AGC Amplifier, 2-20 GHz* [PDF Format]. Retrieved from https://www.hittite.com/content/documents/data_sheet/hmc463lp5.pdf, Hittite Microwave Corp., Massachusetts

[41] Narda, *.5-18 GHz High Performance PIN Switches* [PDF Format]. Retrieved from http://www.nardamicrowave.com/east/index.php?m=Products&e=getPdf&id=5098, Narda, New York

[42] RF Lambda, *AC 110V/220V 8W Ultra Wide Band Power Amplifier 1-22 GHz* [PDF Format]. Retrieved from http://www.rflambda.com/pdf/acamplifier/RAMP01G22GA.pdf, RF Lambda, Texas

[43] Mini-Circuits, *800 MHz-21 GHz Super Ultra Wideband Amplifier* [PDF Format]. Retrieved from http://www.minicircuits.com/pdfs/ZVA-213+.pdf, Mini-Circuits, New York

[44] Hittite Microwave, *GaAs pHEMT MMIC 2 Watt Power Amplifier, 0.1-20 GHz* [PDF Format]. https://www.hittite.com/content/documents/data_sheet/hmc998lp5.pdf, Hittite Microwave Corp., Massachusetts

[45] Daitron, http://www.daitronpower.com/hfs30.html, Daitron, Tokyo, Japan

[46] Daitron, http://www.daitronpower.com/hfd30.html, Tokyo, Japan

[47] Steatite, *0.9-18 GHz Ultra-Wideband Dual Polar Horn* [PDF Format]. Retrieved from http://www.steatiteqpar-antennas.co.uk/Datasheets/STEATITE-QPAR/01_Horns/01_Wideband/QMS-00250_TEST_REPORT.pdf, Steatite, United Kingdom

[48] A-Info, *2-18 GHz Dual Polarization Horn Antenna* [PDF Format]. Retrieved from http://www.ainfoinc.com/en/pro_pdf/new_products/antenna/Dual%20Polarization%20Horn%20Antenna/tr_LB-SJ-20180.pdf, A-Info, Chengdu, China

[49] Satimo, *Closed Wideband Quad Ridge Horns QR2000* [PDF Format]. Retrieved from http://www.satimo.com/sites/www.satimo.com/files/Closed_Wideband_2013.pdf, Microwave Vison, France

[50] B. Panzer and others, *An ultra-wideband, microwave radar for measuring snow thickness on sea ice and mapping near-surface internal layers in polar firn*, Journal of Glaciology Vol. 59, No. 214, pp. 244-254, 2013

8 APPENDIX A: LINK BUDGET MATLAB SCRIPT

```
%**************************************************************************
%File:          F:\CReSIS Folders\NRL_Project\Link Budget\Link Budget
%               MATLAB Script
%Usage:         Link_Budget.m
%Description:  This script is used to generate the Link Budget given an
%               excel sheet containing link budget data. Plots will be
%               generated to show where the signal powers fall within the
%               sensitivity (MDS) and input saturation powers (Psat). The
%               plots can be generated for a specular Nadir return, diffuse
%               Nadir return, and Side-Looking return. All data has been
%               put into variables to allow for easy customization to the
%               current radar system design.
%Author:        Jay McDaniel, j163m149@ku.edu
%               (c) 2015, University of Kansas. All rights reserved.
%Date:          17  March 2015 (Version 1.00)
%Platform:      MATLAB R2008b, Windows 7
%Toolboxes:     Signal Processing
%**************************************************************************

clc;
clear all;
format long

Tx = 2; %choose 0 for Nadir(Specular), 1 for Nadir(Diffuse), or 2 for Side-
Looking

BW =    16*10^9;        %chirp bandwidth
t =     240*10^(-6);    %240us chirp sweep time
nb =    1/t;            %Noise Bandwidth (Hz)
c =     3*10^8;         %speed of light in free space

%if statement will execute depending on Tx chosen
if Tx == 0  %Nadir (Specular)

    R = 1500;       %One Way Range in feet
    R = R*.3048;    %One Way Range in meters
    R = R*2;        %Round Trip in meters

    filename = 'LinkBudget.xlsx';

    PTx =   xlsread(filename, 'C2:C18'); %Transmit Power (dBm)
    f =     xlsread(filename, 'A2:A18'); %Frequency from 2-18 GHz
    l =     xlsread(filename, 'B2:B18'); %Wavelength squared (dBm^2)
    Gamma = xlsread(filename, 'G2:G18'); %Reflection Coefficient (dB)
    GTx =   xlsread(filename, 'D2:D18'); %Transmit Antenna Gain (dBi)
    GRx =   xlsread(filename, 'I2:I18'); %Receiver Antenna Gain (dBi)
    LTx =   xlsread(filename, 'F2:F18'); %Transmitter Cable Loss/1 foot (dB)
    LRx =   xlsread(filename, 'K2:K18'); %Receive Cable Loss/1 foot (dB)

    LTx =    20*LTx; %Transmitter Cable Loss for 20 foot cable (Twin Otter)
    LRx =    19*LRx; %Receiver Cable Loss for 19 foot cable (Twin Otter)

    %for loop to calculate the Received Power in dBm versus frequency
    for d=1:length(PTx)
```

```
        PRx(d) = PTx(d)+l(d)+GTx(d)+GRx(d)+Gamma(d)-10.*log10((4.*pi)^2)-
                 10.*log10((R)^2)-LTx(d)-LRx(d);
    end

    NF =    xlsread(filename, 'L2:L18'); %Noise Figure (dB)
    MDS =   -174+NF+10*log10(nb); %Sensitivity of the receiver (dBm)
    Psat =  xlsread(filename, 'M2:M18'); %Input Saturation Power (dBm)

    %Use spline command to curve fit data across the frequency range
    ff =    0:.01:18;
    PRx1 =  spline(f,PRx,ff);

    figure;
    plot(ff, PRx1,'-g', 'LineWidth', 3)
    hold on
    plot(f,Psat,'-r', 'LineWidth', 3)
    plot(f,MDS,'-b', 'LineWidth', 3)
    xlabel('Frequency (GHz)');
    ylabel('Signals (dBm)');
    title('Nadir Link Budget (1500 ft.)');
    set(gca, 'XTick', [2:1:18])
    xlim([2 18])
    set(gca, 'YTick', [-150:10:0])
    ylim([-150 0])
    grid on
    legend('Received Power (dBm)', 'Input Saturation Power (dBm)',
'Sensitivity (dBm)')



elseif Tx == 1  %Nadir (Diffuse)

    R = 1500;       %One Way Range in feet
    R = R*.3048;    %One Way Range in meters

    filename = 'LinkBudget.xlsx';

    PTx =   xlsread(filename, 'C2:C18'); %Transmit Power (dBm)
    f =     xlsread(filename, 'A2:A18'); %Frequency from 2-18 GHz
    l =     xlsread(filename, 'B2:B18'); %Wavelength squared (dBm^2)
    Gamma = xlsread(filename, 'Q2:Q18'); %Reflection Coefficient (dB)
    GTx =   xlsread(filename, 'D2:D18'); %Transmit Antenna Gain (dBi)
    GRx =   xlsread(filename, 'I2:I18'); %Receiver Antenna Gain (dBi)
    LTx =   xlsread(filename, 'F2:F18'); %Transmitter Cable Loss/1 foot (dB)
    LRx =   xlsread(filename, 'K2:K18'); %Receive Cable Loss/1 foot (dB)

    LTx =    20*LTx; %Transmitter Cable Loss for 20 foot cable (Twin Otter)
    LRx =    19*LRx; %Receiver Cable Loss for 19 foot cable (Twin Otter)

    %code to calculate the side-looking area (pulse limited)
    delta_r = (c.*1.6)/(2*BW);              %range resolution
    theta = acos(R./(R+delta_r));
    r = R*tan(theta);                       %ground annulus radius
    Nadir_Area = pi.*r^2;                   %Nadir area (m^2)
    Nadir_Area_dB = 10.*log10(Nadir_Area);   %Nadir area (dBm^2)
```

```
    %for loop to calculate the Received Power in dBm versus frequency
    for d=1:length(PTx)
        PRx(d) = PTx(d)+l(d)+GTx(d)+GRx(d)+Gamma(d)+Nadir_Area_dB-
                 10.*log10((4.*pi)^3)-10.*log10((R)^4)-LTx(d)-LRx(d);
    end

    NF =    xlsread(filename, 'L2:L18'); %Noise Figure (dB)
    MDS =   -174+NF+10*log10(nb); %Sensitivity of the receiver (dBm)
    Psat =  xlsread(filename, 'M2:M18'); %Input Saturation Power (dBm)

    %Use spline command to curve fit data across the frequency range
    ff =    0:.01:18;
    PRx1 =  spline(f,PRx,ff);

    figure;
    plot(ff, PRx1,'-g', 'LineWidth', 3)
    hold on
    plot(f,Psat,'-r', 'LineWidth', 3)
    plot(f,MDS,'-b', 'LineWidth', 3)
    xlabel('Frequency (GHz)');
    ylabel('Signals (dBm)');
    title('Nadir Link Budget (1500 ft.)');
    set(gca, 'XTick', [2:1:18])
    xlim([2 18])
    set(gca, 'YTick', [-150:10:0])
    ylim([-150 0])
    grid on
    legend('Received Power (dBm)', 'Input Saturation Power (dBm)',
'Sensitivity (dBm)')



elseif Tx == 2  %Side-Looking

    angle = 30; %beam-steering angle off Nadir

    R = 1500;   %One way range in feet
    R = R*.3048;    %One Way Range in meters
    R = R/cosd(angle); %One way range in meters

    filename = 'LinkBudget.xlsx';

    PTx =       xlsread(filename, 'C2:C18'); %Transmit Power (dBm)
    f =         xlsread(filename, 'A2:A18'); %Frequency from 2-18 GHz
    l =         xlsread(filename, 'B2:B18'); %Wavelength squared (dBm^2)
    Gamma =     xlsread(filename, 'H2:H18'); %Reflection Coefficient (dB)
    GTx =       xlsread(filename, 'E2:E18'); %Transmit Antenna Gain (dBi)
    GRx =       xlsread(filename, 'J2:J18'); %Receiver Antenna Gain (dBi)
    LTx =       xlsread(filename, 'F2:F18'); %Transmitter Cable Loss/1ft.(dB)
    LRx =       xlsread(filename, 'K2:K18'); %Receive Cable Loss/1 foot (dB)
    PD_Loss =   xlsread(filename, 'P2:P18'); %Vivaldi Array Power Divider and
                                              Cable Loss

    LTx =    20*LTx; %Transmitter Cable Loss for 20 foot cable (Twin Otter)
    LRx =    19*LRx; %Receiver Cable Loss for 19 foot cable (Twin Otter)
```

```
    %code to calculate the side-looking area (pulse limited in cross-track
    %and beam limited in the along track
    lambda =            c./(f*10^9);                %wavelength (meter)
    effective_length =  .08;                        %effective length (meter)
    beam_x =            lambda./effective_length;   %x-dir. array beam width
    elevation_angle =   angle*pi/180;
    sigma_r =           (c.*1.6)/(2*BW);            %range resolution
    sigma_rg_SLAR =     sigma_r/elevation_angle;
    R_SLAR =            R;
    A_SLAR =            sigma_rg_SLAR.*R_SLAR.*beam_x;
    A_SLAR_dB =         10*log10(A_SLAR);

    %for loop to calculate the Received Power in dBm versus frequency
    for d=1:length(PTx)
        PRx(d) = PTx(d)+GTx(d)+GRx(d)+l(d)+Gamma(d)+A_SLAR_dB(d)-
                 10*log10((4*pi)^3)-10*log10(R^4)-LTx(d)-LRx(d)-PD_Loss(d);
    end

    NF =    xlsread(filename, 'N2:N18'); %Noise Figure (dB)
    MDS = -174+NF+10*log10(nb); %Sensitivity of the receiver (dBm)
    Psat =  xlsread(filename, 'O2:O18'); %Input Saturation Power (dBm)

    %Use spline command to curve fit data across the frequency range
    ff = 0:.01:18;
    PRx1 =  spline(f,PRx,ff);

    figure;
    plot(ff, PRx1,'-g', 'LineWidth', 3)
    hold on
    plot(f,Psat,'-r', 'LineWidth', 3)
    plot(f,MDS,'-b', 'LineWidth', 3)
    xlabel('Frequency (GHz)');
    ylabel('Signals (dBm)');
    title('Side-Looking Link Budget (1500 ft.)');
    set(gca, 'XTick', [2:1:18])
    xlim([2 18])
    set(gca, 'YTick', [-150:10:0])
    ylim([-150 0])
    grid on
    legend('Received Power (dBm)', 'Input Saturation Power (dBm)',
'Sensitivity (dBm)')
end
```

9 EAGLE SCHEMATIC AND BOARD LAYOUTS

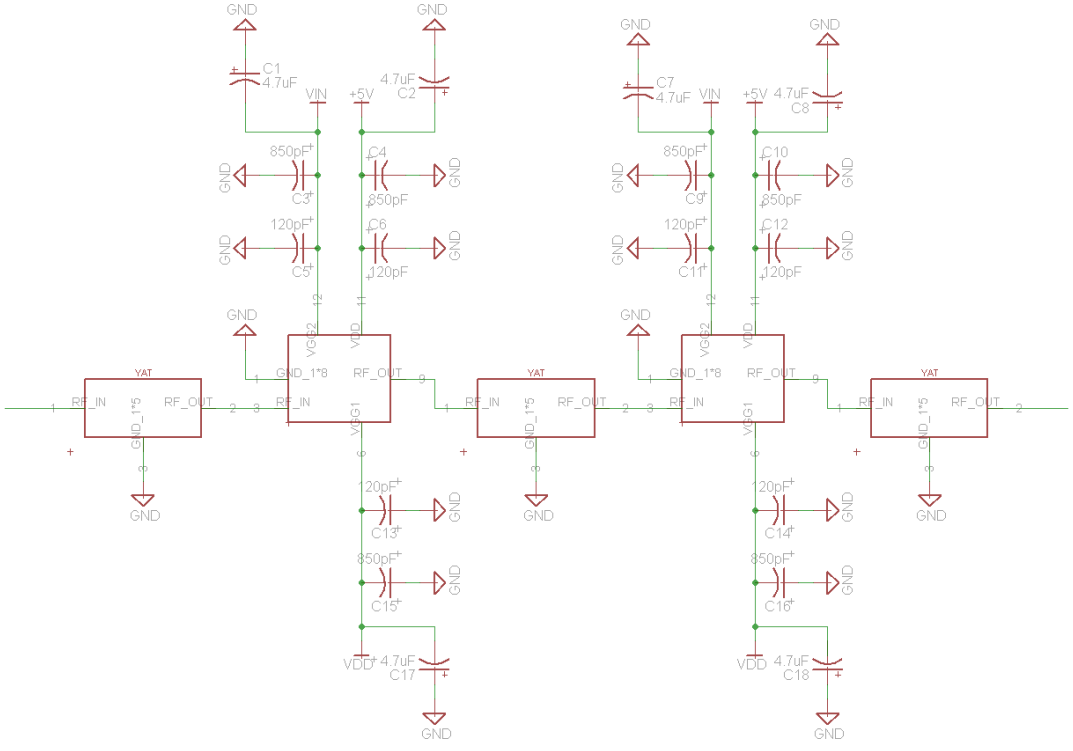

Figure 9-1: RF Amplifier Chain v5 Schematic

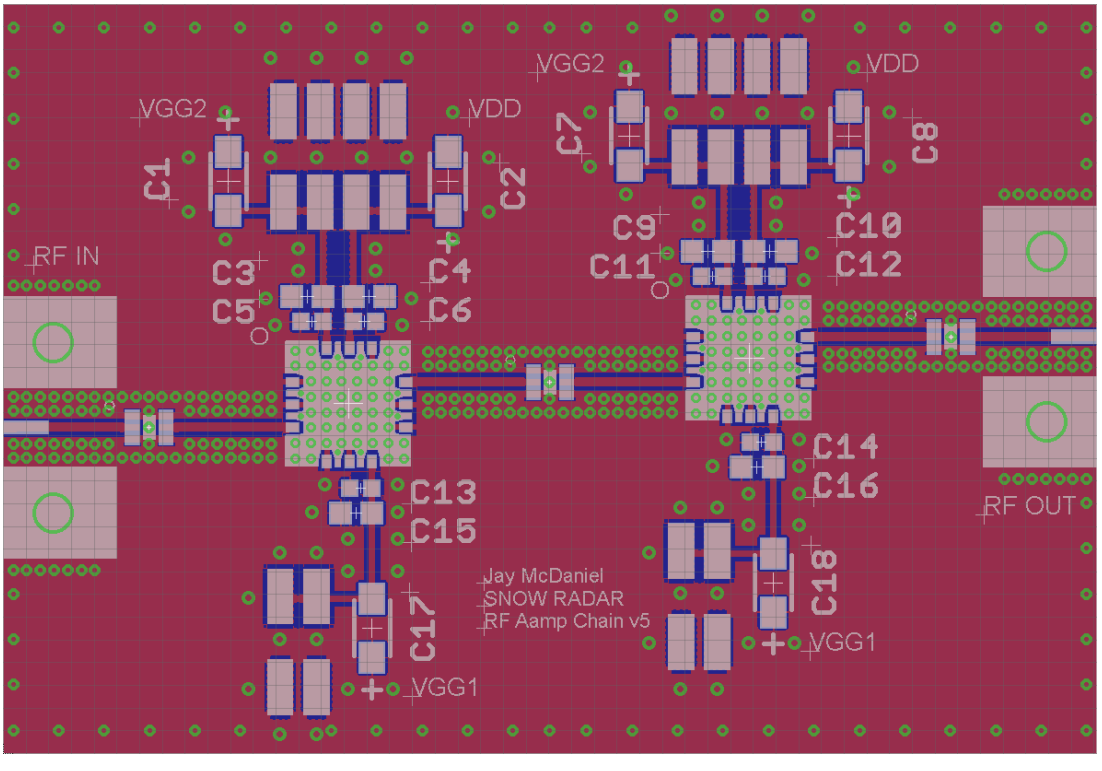

Figure 9-2: RF Amplifier Chain v5 Board Layout

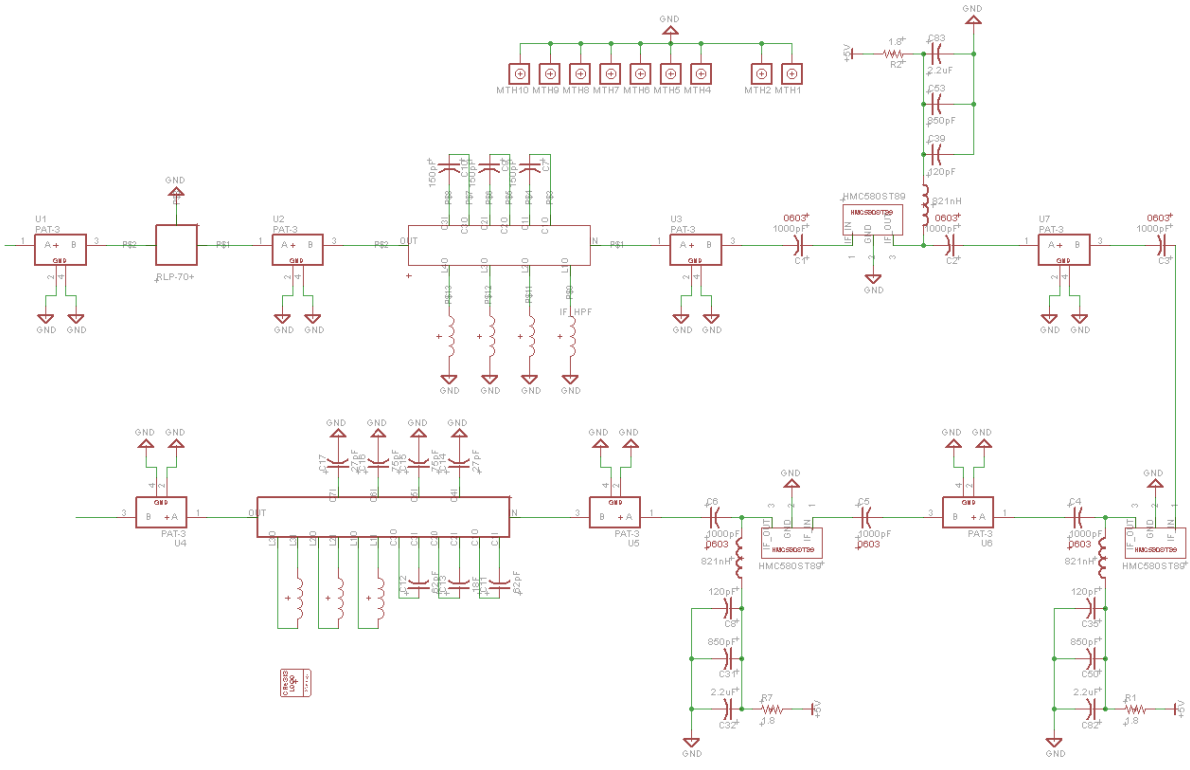

Figure 9-3: IF Chain v5 Schematic

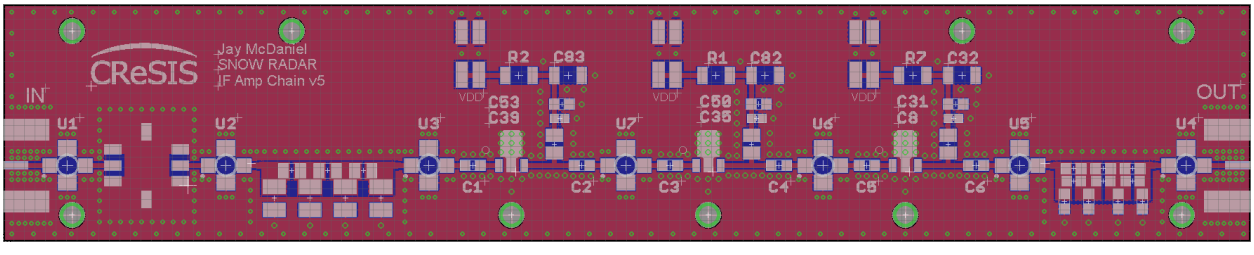

Figure 9-4: RF Amplifier Chain v5 Boar Layout